DOKUZ EYLÜL UNIVERSITY
GRADUATE SCHOOL OF NATURAL AND APPLIED SCIENCES

INVESTIGATION OF FLOW STRUCTURES AT HOUSEHOLD DEVICES BY DATA ASSIMILATION OF OPTICAL FLOW DIAGNOSTICS

by
Utku Alp YÜCEKAYA

September, 2024
İZMİR

INVESTIGATION OF FLOW STRUCTURES AT HOUSEHOLD DEVICES BY DATA ASSIMILATION OF OPTICAL FLOW DIAGNOSTICS

A Thesis Submitted to the
Graduate School of Natural and Applied Sciences of Dokuz Eylül University
In Partial Fulfillment of the Requirements for the Degree of Doctor of Philosophy in Mechanical Engineering, Energy Program

by

Utku Alp YÜCEKAYA

September, 2024
İZMİR

Ph.D. THESIS EXAMINATION RESULT FORM

We have read the thesis entitled **"INVESTIGATION OF FLOW STRUCTURES AT HOUSEHOLD DEVICES BY DATA ASSIMILATION OF OPTICAL FLOW DIAGNOSTICS"** completed by **UTKU ALP YÜCEKAYA** under supervision of **PROF.DR. DİLEK KUMLUTAŞ** and we certify that in our opinion it is fully adequate, in scope and in quality, as a thesis for the degree of Doctor of Philosophy.

Prof. Dr. Dilek KUMLUTAŞ

Supervisor

Prof. Dr. Yalçın ÇEBİ

Thesis Committee Member

Prof. Dr. Can Özgür ÇOLPAN

Thesis Committee Member

Prof. Dr. Mustafa Turhan ÇOBAN

Examining Committee Member

Prof. Dr. Cüneyt EZGİ

Examining Committee Member

Prof. Dr. Okan FISTIKOĞLU

Director

Graduate School of Natural and Applied Sciences

ACKNOWLEDGMENT

I would like to thank Prof. Dr. Dilek KUMLUTAŞ, my very valuable doctoral thesis supervisor and project executive, who provided all kinds of support in this thesis study and always showed the right path in my academic life, studies and work.

This thesis was supported by The Scientific and Technological Research Council of Turkey (TUBITAK) and Demirdöküm Heating Company with the 5180092 encoded 1505 project. I would like to emphasise my appreciation for being a part of this effort on the project. It was also supported by The Scientific and Technological Research Council of Turkey (TUBITAK) and Vestel Air-Conditioner Company with the 5140039 encoded 1505 project. I would like to thank to Electrolux Company of their support and contributions of thesis.

I would like to specially thank to my colleague Dr. Özgün ÖZER. We handled all the hardships of research together. I would also like to thank Dr. Hasan AVCI, M.Sc. A. Yakup CUMBUL. Working with them is a pleasure.

I want to express my endless gratitude to my life mate, Alaz İZER YÜCEKAYA, who always been with me and supported me with endless love and patience. Special thanks to my father Mehmet YÜCEKAYA, my mother Gülümay YÜCEKAYA, my sister Burcu ÖZTÜRK and my whole family who never forgave their support from me and they made me come to this day.

Utku Alp YÜCEKAYA

INVESTIGATION OF FLOW STRUCTURES AT HOUSEHOLD DEVICES BY DATA ASSIMILATION OF OPTICAL FLOW DIAGNOSTICS

ABSTRACT

The thesis examines the volumetric temperature and velocity distributions of split air conditioners (SAC), combi boilers, and air purifiers using Stereo Particle Imaging Velocimetry (SPIV) and Meshed Infrared Thermography (MIT) methods. The experimental volumetric flow structures serve as boundary conditions for numerical studies, using from a new data assimilation method developed in this thesis. This novel approach ensures highly accurate numerical studies, as it utilizes experimental volumetric data as boundary conditions, a departure from conventional literature methods.

In this thesis, the volumetric velocity distribution in the outlet section of the SAC indoor unit was measured using SPIV, while the temperature distribution was determined using the MIT method. The data obtained from these experimental measurements were assimilated to establish a realistic boundary condition for the time-dependent Computational Fluid Dynamics (CFD) model. The developed data assimilation approach in this thesis resulted in more accurate numerical analysis, with only a 3.13% average error, in contrast to the conventional approaches that yielded a 13.9% average error.

In order to conduct a thorough analysis of a 24 kW combi boiler fan-burner system in the thesis studies, it is imperative to accurately model the burner inlet section. This modeling directly impacts the system's overall performance and emission results. SPIV experiments were conducted to obtain the volumetric flow structure of the burner inlet region with and without a cover. Furthermore, the impact of spatial resolution in SPIV experiments on both the experimental results and numerical analysis using data assimilation method were illustrated. Through the application of the data assimilation method as a novel contribution to the literature, the margin of error between experimental data and numerical results were reduced from 24% to 4% approximately.

The SPIV method was used to analyze the volumetric flow structures of the blowing and suction zones of the household air purifier. The results revealed that the airflow through the filter surface is non-uniform. Consequently, assumptions of constant flow rate or homogeneous velocity in numerical studies would be inaccurate. The volumetric data obtained were utilized as a boundary condition for CFD analyses through data assimilation method. The analyses were validated with an error margin of 1%.

As a novel contribution of the literature, the data assimilation method employing volumetric optical flow diagnostics, developed as part of this thesis, holds considerable promise for enhancing the realism and accuracy of CFD analyses. This approach has emerged as a valuable tool for investigating flow structures, significantly expanding its applicability in the field of fluid dynamics studies and leaving a lasting impact on both academic research and practical engineering applications.

Keywords: Data assimilation, particle image velocimetry, meshed infrared thermography, computational fluid dynamics, split air conditioner, combi boiler, air purifier

EV TİPİ CİHAZLARDA AKIŞ YAPILARININ OPTİK AKIŞ TANILAMA VERİ ASİMİLASYONU İLE İNCELENMESİ

ÖZ

Bu tez kapsamında, split klima, kombi ve hava temizleme cihazının hacimsel sıcaklık ve hız dağılımları Stereo Parçacık Görüntülemeli Hız Ölçümü (SPGHÖ) ve Ağ Yapılı Kızılötesi Sıcaklık Ölçümü (AYKSÖ) yöntemleri ile elde edilmiştir. Deneysel olarak elde edilen hacimsel akış yapıları tez kapsamında geliştirilen veri asimilasyonu yöntemi kullanılarak sayısal çalışmalara sınır koşulu olarak tanımlanmıştır. Yöntem, literatürden farklı olarak deneylerden elde edilen hacimsel verilerin sınır koşulu olmasını sağladığı için sayısal çalışmaların yüksek doğruluğa sahip olmasına olanak sağlamıştır.

Tez kapsamında, split klima iç ünitesinin üfleme bölgesindeki üç boyutlu hız dağılımı SPGHÖ ile sıcaklık dağılımı ise AYKSÖ yöntemi ile belirlenmiştir. Bu deneysel ölçümlerden elde edilen veriler, zamana bağlı Hesaplamalı Akışkanlar Dinamiği (HAD) modeli için gerçekçi bir sınır koşulu oluşturmak üzere asimile edilmiştir. Geliştirilen veri asimilasyonu yaklaşımı (%3,13 ortalama hata) sayesinde, geleneksel yaklaşımlara (%13,9 ortalama hata) oranla daha doğru sayısal analiz sonuçları elde edildiği görülmektedir.

Tez çalışmalarında incelenen 24 kW kombi fan-brülör sisteminin kapsamlı analizi için brülör giriş bölgesinin doğru modellenmesi kritik öneme sahiptir. Bu modelleme genel performans ve emisyon sonuçlarını direk olarak etkilemektedir. Bu sebeple kapak kullanılan ve kullanılmayan brülör giriş bölgesinin SPGHÖ deneyleri gerçekleştirilerek hacimsel akış yapısı elde edilmiştir. Ayrıca SPGHÖ deneylerinde uzaysal çözünürlüğün deney sonuçları ve veri asimilasyonu ile sayısal analiz üzerindeki etkisi ortaya konmuştur. Literatüre katkı olarak, veri asimilasyonu yönteminin uygulanması ile deneysel verilerle sayısal sonuçlar arasındaki hata payı yaklaşık olarak %24'lerden %4'e kadar düşürülmüştür.

Ev tipi hava temizleme cihazının üfleme ve emiş bölgelerinin hacimsel akış yapıları SPGHÖ yöntemi ile elde edilmiştir. Elde edilen sonuçlar filtre yüzeyinden geçen

havanın homojen olmadığı ve dolayısıyla sayısal çalışmalarda sabit debi veya hız gibi tanımlamaların hatalı olacağını ortaya koymuştur. Elde edilen hacimsel veriler HAD analizlerine sınır koşulu olarak veri asimilasyonu yöntemi ile tanımlanmış ve %1 gibi hata payı ile analizler doğrulanmıştır.

Literatüre yeni bir katkı olarak tez kapsamında geliştirilen hacimsel optik akış tanılama kullanan veri asimilasyon yöntemi, akış yapılarının incelenmesi için bir yaklaşım olarak ön plana çıkarak, daha gerçekçi ve doğru HAD analizleri için önemli bir potansiyele sahiptir. Bu kapsamda, yöntem akışkanlar dinamiği incelemelerinde, akademik ve pratik mühendislik çevrelerinde etki yaratarak geniş bir uygulanabilir alan yaratmıştır.

Anahtar kelimeler: Veri asimilasyonu, parçacık görüntülemeli hız ölçümü, ağ yapılı kızılötesi sıcaklık ölçümü, hesaplamalı akışkanlar dinamiği, split klima, kombi, hava temizleme cihazı

CONTENTS

Page

Ph.D. THESIS EXAMINATION RESULT FORM ii
ACKNOWLEDGMENT iii
ABSTRACT iv
ÖZ vi
LIST OF FIGURES x
LIST OF TABLES xv

CHAPTER ONE INTRODUCTION 1

1.1 Literature Review 2
1.1.1 Literature Search on Optical Flow Diagnostics 2
1.1.2 Literature Search on Split Air Conditioner 9
1.1.3 Literature Search on Combi Boiler 13
1.1.4 Literature Search on Air Purifier 16
1.2 Aim and Motivation 17

CHAPTER TWO METHODOLOGY 19

2.1 Particle Image Velocimetry 19
2.1.1 Stereo Particle Image Velocimetry Components 21
2.2 Meshed Infrared Thermography 26
2.2.1 Validation of Three Dimensional Meshed Infrared Thermography Method 32

CHAPTER THREE EXPERIMENTAL AND NUMERICAL INVESTIGATION OF AIR CONDITIONER 36

3.1 Stereo Particle Image Velocimetry and Meshed Infrared Thermography Experiments to Investigate Split Air Conditioner Indoor Unit Outlet Section. 37
3.1.1 Temperature Measurement: Meshed Infrared Thermography 37
3.1.2 Velocity Measurement: Stereo Particle Image Velocimetry 39
3.2 Numerical Study of the Split Air Conditioner Indoor Air Effect 41

3.3 Validation of Numerical Studies by Data Assimilation with Stereo Particle Image Velocimetry 45
3.4 Results..... 48

CHAPTER FOUR EXPERIMENTAL AND NUMERICAL INVESTIGATION OF FAN-BURNER SYSTEM OF THE COMBI BOILER..... 57

4.1 Flow Structure of Fan-Burner System in Combi Boiler..... 58
4.1.1 The Spatial Resolution of Investigation Planes' Effect on Three-Dimensional Reconstruction of Jet Flow Structure of Fan-Burner System in Combi Boiler..... 69
4.1.2 The Burner Cover Effect on Flow Structure of Fan-Burner System in Combi Boiler..... 73
4.2 Numerical Investigation of Combi Boiler Fan-Burner System by Data Assimilation with Stereo Particle Image Velocimetry 75

CHAPTER FIVE EXPERIMENTAL AND NUMERICAL INVESTIGATION OF AIR PURIFIER SYSTEMS..... 94

5.1 Stereo Particle Image Velocimetry Experiments to Investigate Air Purifier 95
5.2 Numerical Investigation of Air Purifier by Data Assimilation with Stereo Particle Image Velocimetry..... 105

CHAPTER FIVE CONCLUSIONS 112

REFERENCES..... 116

LIST OF FIGURES

Page

Figure 1.1 Leonardo da Vinci‘s “a free water jet issuing from a square hole into a pool” 3
Figure 1.2 a) Leonardo da Vinci's aortic valve vortices, b) Velocity vectors from MRI in the left ventricular outflow tract..... 3
Figure 1.3 Ludwig Prandtl in front of his water tunnel for flow visualisation in 1904 4
Figure 2.1 The schematic of SPIV setup..... 20
Figure 2.2 Different particle distribution densities 21
Figure 2.3 Elementary kinds of interactions between atoms and electromagnetic radiation..... 23
Figure 2.4 The ND:YAG Laser used in the experiments..... 24
Figure 2.5 The cameras used in the experiments 25
Figure 2.6 Three-dimensional meshed infrared thermography setup 27
Figure 2.7 a)Target projection on the sensor and b) Simulated temperature map 29
Figure 2.8 Optical schematic of the proposed 3D MIT setup 30
Figure 2.9 The schematic of the experimental setups. a) 3D MIT experimental setup b) 2D measurement screens experimental setup 32
Figure 2.10 Linear regression fitting between the measurements of both validation experiments 33
Figure 2.11 A) Average volumetric temperature isosurfaces of the CFF obtained via 3D MIT. B) Average volumetric velocity isosurfaces of the CFF obtained via PIV. 34
Figure 3.1 MIT experiment setup a) Isometric view b) Left view..... 38
Figure 3.2 SAC indoor unit outlet section MIT experiment results..... 38
Figure 3.3 SPIV investigation planes and SPIV velocity distribution result of the z= 742.5 mm plane..... 40
Figure 3.4 Average volumetric velocity iso-surfaces 3m/s, 4 m/s and 5 m/s at the outlet section of the SAC indoor unit obtained by SPIV 40
Figure 3.5 The air volume of the three-dimensional room model 42

Figure 3.6 The position of the obtained data point and plane 44
Figure 3.7 Validation line (red) position 45
Figure 3.8 Velocity profile comparison between SPIV data and CFD data with different boundary conditions 47
Figure 3.9 Boundary conditions of outflow section: a) Temperature BC: Homogeneous, Velocity BC: Homogeneous, b) Temperature BC: Homogeneous, Velocity BC: PIV, c) Temperature BC: MIT, Velocity BC: Homogeneous, d) Temperature BC: MIT, Velocity BC: PIV 49
Figure 3.10 Penetration of outflow section of air conditioner indoor unit, a) Temperature BC: MIT, Velocity BC: PIV, b) Temperature BC: MIT, Velocity BC: Homogeneous 50
Figure 3.11 Temperature and velocity distributions of the XY midplane of the room at 180 seconds: a) Velocity BC: SPIV, b) Temperature BC: MIT, c) Velocity BC: Homogeneous, d) Temperature BC: Homogeneous 52
Figure 3.12 Temperature histograms at 180 s, 360 s, 600 s 54
Figure 3.13 Temperature distributions of the XY midplane of the room at different times: a, b, c) Temperature BC: MIT, Velocity BC: SPIV, d, e, f) Temperature BC: Homogeneous, Velocity BC: SPIV 55
Figure 4.1 CAD of combi boiler fan-burner system 57
Figure 4.2 CAD of cover at the burner inlet 58
Figure 4.3 CAD drawing of the fan outlet area of the 24 kW capacity combi boiler device a) Fan system without burner b) Fan system with burner 59
Figure 4.4 SPIV experiment setup 59
Figure 4.5 Combi boiler fan-burner system investigation region a) fan-burner system of the combi boiler, b) dimensions of the burner inlet, c) SPIV investigation area 60
Figure 4.6 Investigation planes of SPIV experiment 61
Figure 4.7 z=40 mm SPIV experiment results a) direct camera b) angular camera .. 62
Figure 4.8 z=40 mm SPIV experiment velocity distribution results a) direct camera b) angular camera 63
Figure 4.9 z=40 mm SPIV 3 component velocity map 64

Figure 4.10 SPIV results at line a) u-velocity b) v-velocity b) w-velocity d) resultant velocity 66
Figure 4.11 Fan-Burner system three-dimensional velocity 5 m/s, 8 m/s and 10 m/s iso-surfaces 68
Figure 4.12 Schematic of Fan-Burner system experiment setup for SPIV 70
Figure 4.13 SPIV experiment images a) direct camera b) angular camera 70
Figure 4.14 Velocity distribution obtained by SPIV of the burner inlet a) direct camera b) angular camera 71
Figure 4.15 Fan-Burner system three-dimensional velocity 7 m/s, 12 m/s and 20 m/s iso-surfaces 72
Figure 4.16 Burner inlet cover 73
Figure 4.17 Velocity distribution obtained by SPIV of the burner inlet a) direct camera b) angular camera 74
Figure 4.18 Velocity distribution obtained by SPIV of the burner inlet a) direct camera b) angular camera 74
Figure 4.19 Stereo velocity distribution obtained by SPIV of the burner inlet 75
Figure 4.20 Fluid domain to investigate burner flow structure a) burner and environment b) cross-section of fluid domain c) burner fluid domain ... 77
Figure 4.21 Mesh structure of fluid domain a) mesh structure b) details of mesh ... 78
Figure 4.22 Data assimilated inlet boundary condition 79
Figure 4.23 Data assimilated inlet boundary condition comparison with SPIV volumetric velocity results a) generated volumetric velocity distributions using SPIV b) data assimilated boundary condition 80
Figure 4.24 Velocity distributions of burner inside a) homogeneous flowrate B.C. b) data assimilated B.C. 81
Figure 4.25 a) Volumetric velocity distributions obtained by SPIV b) Inlet boundary condition by data assimilated volumetric velocity data 82
Figure 4.26 Inlet boundary condition by data assimilated volumetric velocity data a) interpolated data from SPIV b) directly used SPIV data 83
Figure 4.27 Velocity vectors of inlet boundary condition a) interpolated data from SPIV b) directly used SPIV data 83

Figure 4.28 Velocity distributions of burner mid-plane a) homogeneous flowrate B.C. b) data assimilated B.C. from interpolated data from SPIV c) data assimilated B.C. from directly used SPIV data 84
Figure 4.29 SPIV experiment images a) direct camera b) angular camera 85
Figure 4.30 SPIV two-dimensional three component velocity distributions of burner surface 86
Figure 4.31 Validation line (red) 87
Figure 4.32 Velocity distribution of validation line at Figure 4.30 87
Figure 4.33 Second validation line (blue) 88
Figure 4.34 Velocity distribution of validation line at Figure 4.32 89
Figure 4.35 Inlet boundary condition by data assimilated volumetric velocity data from SPIV experiment with burner cover geometry 90
Figure 4.36 Velocity distribution of validation line at 1 91
Figure 4.37 Velocity distribution of validation line at 2 92
Figure 5.1 Investigated air purifier system 95
Figure 5.2 CAD geometry of investigated air purifier 96
Figure 5.3 SPIV setup to investigate the air purifier 97
Figure 5.4 z=160 mm SPIV experiment results a) direct camera b) angular camera 97
Figure 5.5 z=160 mm SPIV experiment velocity vector map a) direct camera b) angular camera 98
Figure 5.6 SPIV setup to investigate the air purifier outlet section 99
Figure 5.7 z=0 mm SPIV experiment velocity vector map 99
Figure 5.8 Air purifier outlet section crown 100
Figure 5.9 SPIV results of air purifier outlet section without crown a) z=0 from parallel angle b) z=160 (mid-plane) from direct angle 101
Figure 5.10 SPIV results of air purifier outlet section a) with crown b) without crown 102
Figure 5.11 Velocity distribution of red line in Figure 5.10 103
Figure 5.12 SPIV results of air purifier suction region a) with filter b) without filter 104

Figure 5.13 Numerical model of air purifier CFD analysis a) room and air purifier fluid domain b) air purifier fluid domain 106
Figure 5.14 Mesh structure of air purifier fluid domain 107
Figure 5.15 Velocity distributions of mid-plane 108
Figure 5.16 Velocity distributions of outlet section of air purifier a) CFD result b) SPIV result 109
Figure 5.17 Comparison of SPIV and CFD results 110

LIST OF TABLES

Page

Table 1.1 Comparison of CFD studies on indoor air environment supported by experiment 12

Table 3.1 Average velocity comparison between SPIV and CFD at line 48

Table 5.1 Average velocity comparison of SPIV and CFD results 110

CHAPTER ONE
INTRODUCTION

Household devices are machines with tasks such as heating, cooling, cooking, food storage, fresh air in our daily lives. The machines developed for each task have been met with great interest because they provide comfort to human life in their early periods. Their first designs focused on their tasks without worrying about efficiency and environmentalism. However, with the developing technology and aesthetic concerns, design improvements of such devices have come to the fore.

The research process can be grouped as aesthetic, mechanical and aerothermal. While the aesthetic features of the devices are determined at the industrial design stage, the stage where the mechanical properties of plastic and sheet metal parts are determined is known as mechanical design. In the aerothermal design phase, the flow structure, heat transfer areas, etc., that will affect the energy efficiency and performance of the devices are examined.

In the aerothermal design phase, it is critical to examine the systems' heat transfer and flow characteristics. For this reason, numerical studies are carried out. However, the assumptions made in numerical studies can distract researchers from the high-fidelity results. For this reason, experimental studies come to the fore in terms of verifying numerical studies and advancing design processes with less margin of error.

As the structures of the devices examined become more complex, the results provided by experimental studies are essential. Providing quantitative data as well as qualitative data gains importance at this point. In addition, the ability to obtain data in 2 or 3 dimensions with the complexity of the systems creates a facilitating effect on the research processes.

Optical experimental methods that provide two or three-dimensional data are advantageous for aerothermal investigations of household devices with such complex structures.

In aerothermal investigation, constraints involving time and value are paramount. For this reason, numerical studies are often preferred. Nevertheless, it's crucial to verify these studies and the underlying assumptions, as they can significantly impact the margin of error. Taking all these factors into account, the data assimilation method, which integrates experimental and numerical studies, has been developed within the framework of this thesis.

1.1 Literature Review

1.1.1 Literature Search on Optical Flow Diagnostics

Professor F.M.N. Brown of the University of Notre Dame wrote(Smits & Lim, 2012):

> A man is not a dog to smell out each individual track, he is a man to see, and seeing, to analyse. He is a sight tracker with each of the other senses in adjunctive roles. Further, man is a scanner, not a mere looker. A single point has little meaning unless taken with other points and many points at different times are a little better. He needs the whole field, the wide view.

Flow visualisation is a crucial aspect of understanding fluid dynamics, enabling researchers to gain insights into complex flow patterns and behaviours. This chapter reviews the key literature related to flow visualisation techniques, methodologies, and applications, emphasising the evolution of visualisation methods over time.

In the 15th century, it was an interesting field to understand flow by visualising it, which can be found even in Leonarda da Vinci's aorta and water channel drawings as can be seen Figure 1.1 and 1.2 (Hak, 2000).

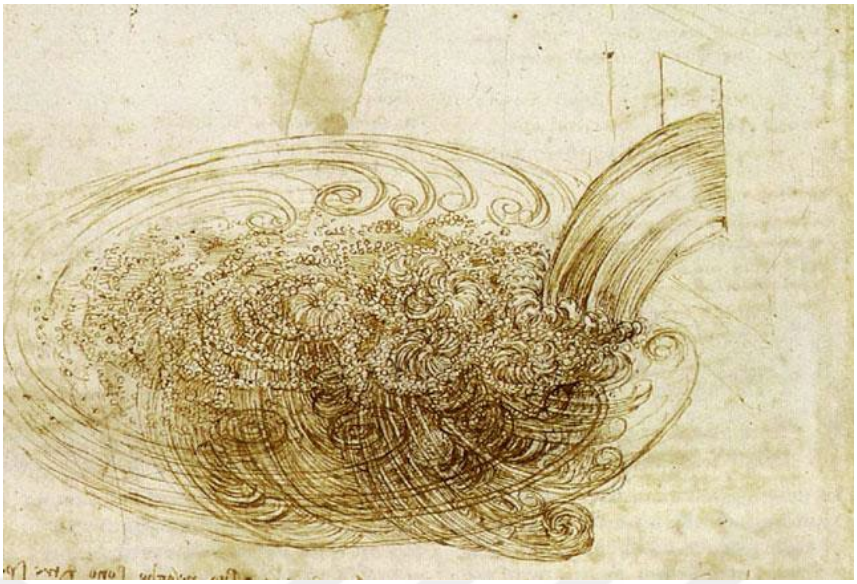


Figure 1.1 Leonardo da Vinci‘s “a free water jet issuing from a square hole into a pool” (Hak, 2000)

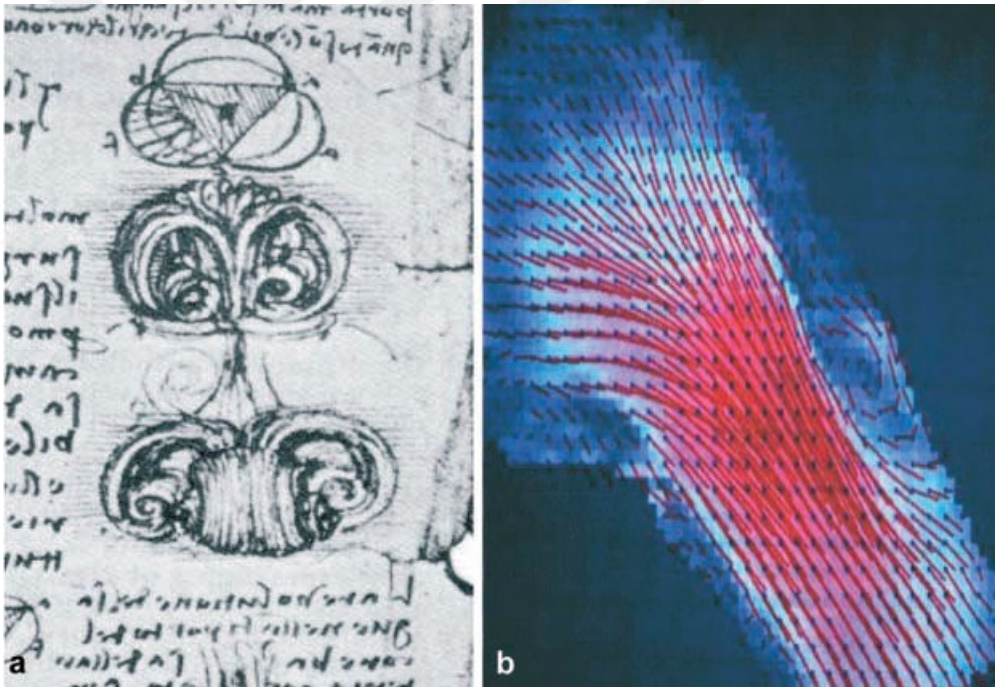


Figure 1.2 a) Leonardo da Vinci's aortic valve vortices, b) Velocity vectors from MRI in the left ventricular outflow tract (Gharib et al., 2002)

There are qualitative and quantitative examples of flow imaging methods used to make sense of flow systems with complex structures. In qualitative examinations, the flow structure can be examined by photographing the paint and smoke added to the flow. In addition, qualitative results can be obtained by utilising the density difference

of the flow using methods such as Schileren (Özer et al., 2017). When the methods that can give quantitative results are examined, there are experimental systems that can make point, planar and volumetric measurements. All these methods that create flow patterns can be used to make sense of the physics of flow. In order to effectively comprehend flow patterns, a comprehensive comprehension of steady and unsteady flow pathlines, streaklines, and streamlines to explain the flow field clearly is imperative (Smits & Lim, 2012).

Qualitative analyses are based on examining the 2D or 3D structure of the flow and interpreting it by obtaining the flow structure. One of the first examples of the studies is Ludwig Prandtl's addition of mica particles to the water flow (Figure 1.3) (Raffel et al., 2007).

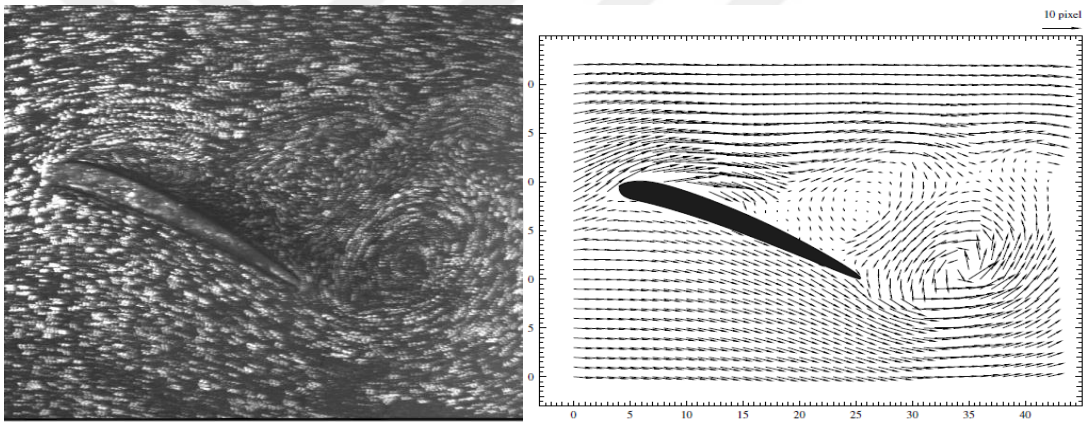


Figure 1.3 Ludwig Prandtl in front of his water tunnel for flow visualisation in 1904 (Raffel et al., 2007)

In past years, a method involving the introduction of hydrogen bubbles obtained through electrolysis into a fluid was developed to qualitatively observe flow dynamics, such as turbulence, flow separation, and boundary layers (Kline et al., 1967). This approach was instrumental in providing insights into the qualitative aspects of fluid flow.

Additionally, a long-standing and cost-effective method for visualizing flow involves the use of smoke and paint. This method, first employed by Reynolds in 1883, entails introducing smoke or paint with a density similar to that of the fluid into the flow, allowing for the visualization of flow properties through analogous movements. This approach continues to be utilized in qualitative research due to its cost-

effectiveness and ease of application, offering the significant advantage of enabling spatial or volumetric observation of flow (Reynolds, 1883).

To comprehend and enhance the physics of flow, quantitative imaging has been utilized over various periods. The Particle Image Velocimetry (PIV) method, featured in this thesis and available in 2D and 3D versions in literature, stands as one of the primary techniques for determining flow velocity and velocity-dependent properties. Its inception dates back to 1984 (Adrian, 2005). This method necessitates a high-speed camera, light source, suitable particles for the flow, a computer, and a synchronization device for the camera and light source. Tracer particles, compatible with the fluid density under examination, are introduced into the region of interest and illuminated with a high-power light source. High-speed cameras capture sequential images of the illuminated particles to acquire velocity data. Initially facilitating moving flows, the method evolved to offer experimental data for intricate flows, including turbulence and volumetric investigation (Özer, 2017).

The PIV method has been widely utilized across various fields to glean insights into the flow physics of different systems. It has particularly gained prominence in the analysis of household appliances, where the flow structure significantly impacts the performance of the system.

Ben Amara et al. (2008) investigated the airflow due to natural convection in a static refrigerator model using the PIV system. They compared the experimental data obtained with the numerical study. In addition, the results obtained from PIV allowed the prediction of the hydrodynamic boundary layer on the wall (Ben Amara et al., 2008).

Keller et al. (2014) investigated the fluid interaction between the impeller and volute at the nominal flow rate of a centrifugal pump using the PIV method. As a result of the study, turbulence kinetic energy, vorticity and velocity maps were generated by PIV method. It was determined in which region of the vanes the turbulence generation occurs for the examined flow rate (Keller et al., 2014).

Ozer & Kumlutaş (2017) investigated the design parameters of split air conditioner (SAC) indoor unit using Stereo PIV (SPIV) method. They were able to obtain a 3-component velocity map using SPIV and presented the air conditioner design parameters in detail. As a result of the study, they proposed the optimum flow structure for the range examined. (Özer & Kumlutaş, 2017).

Chen et al. (2018) using the advantages of the PIV method of high spatial resolution and non-intrusive method, they investigated a hood driven flow. The effect of the distance between the cooker and the hood on the exhaust air is investigated (W. Chen et al., 2018).

The PIV method allows the flow structures of the devices to be examined, as well as turbomachinery driving fluid such as fans and pumps. Cantrak & Jankovic (2022) utilised the PIV system to investigate the turbulent flow created by an axial fan in a piping system. In the study for different Reynolds numbers, the results of turbulence physics of Rankine type turbulent flow are presented (Čantrak & Janković, 2022).

Another parameter as important as velocity when analysing the flow structure is temperature. Since temperature directly affects the density of the fluid, it also affects the flow structure. The most common way to obtain temperature data as optical inspection is infrared cameras. Infrared imaging techniques are currently utilized to determine the temperature of solid materials that are opaque in infrared wavelengths and emit with a distinct emissivity coefficient. Infrared cameras can visualize gases with high temperature and particle density. However, due to the transparency of gases at infrared wavelengths (7–13 μm), as well as issues such as low signal-to-noise ratio and unknown emissivity distributions, direct temperature determination of gases is not feasible with infrared cameras. To address this challenge, measurement screens have been employed in the literature.

A measurement screen is a solid target placed in a gas medium, enabling the determination of gas temperature through convection. The temperature distribution of the measurement screen is captured using infrared thermography. It's important to note that this method indirectly measures gas temperature, and its success relies on the heat

transfer mechanism between the measurement screen and the gas. As a result, various types of measurement screen targets have been proposed in the literature.

The measurement screen method was first utilized and reported by Anderson et al. (1991) and later by Burch et al. (1992) to analyze the temperature distribution in a car's aeration streams. They used a fiberglass sheet (plane target) with a thickness of 0.25 mm and 70% porosity as the measurement screen. Comparing the results obtained with the measurement screen to those obtained with a calibrated thermocouple revealed that the temperature distribution could be determined with an accuracy of ±1.3 K. Additionally, the measurement screen demonstrated a time response of 0.3 second (Anderson et al., 1991; Burch et al., 1992).

In a separate research study utilizing a measurement screen, Elvsén and Sandberg (2009) examined a floating jet in a ventilated room. They visualized the instantaneous velocity and temperature distributions near the diffuser using various flow visualization methods, such as Particle Streak Velocimetry (PSV), PIV, and infrared thermography techniques (Elvsen & Sandberg, 2009). The researchers aimed to mitigate backside radiation by employing a double-layer measurement screen, as recommended by Cehlin et al. (2002) (Cehlin et al., 2002). However, the use of aluminium foil as the second layer in this approach might elevate heat transfer within the measuring screen, potentially leading to increased measurement errors.

The wire-based methods offer volumetric temperature distribution measurement. These methods can be divided into two groups. The first group includes the use of thermistors (thermoresistive temperature sensors) with the application of conductivity sampling for temperature field measurement (Ritterath et al., 2011). Several examples of this method exist (Arlit et al., 2018; Kelm et al., 2016; Schäfer et al., 2013). When compared with the infrared imaging methods, these wire-based methods offer the advantage of higher time resolution and lower flow distortion due to the size of the target. Additionally, there is the optical fiber method, which shares the same advantages as the thermistor (Lomperski et al., 2015).

An alternative approach for measuring air temperature (as well as the temperature of similar gases) involves using a probe. Although this method is effective for

determining temperature at a specific location, it is limited to performing single-point measurements. Therefore, to assess heat distribution across an area, it is necessary to use multi-point measurement devices, which can result in the development of complex systems. When temperature measurements are conducted using thermocouples or probe scanning, temporal variations occur, requiring the use of a traverse system.

In the method developed and implemented as part of the thesis, we acquired the simultaneous volumetric temperature distribution of infrared-transparent flows (such as air, gases, etc.) with minimal distortion on the flow structure through the innovative 3D Meshed Infrared Thermography (3D MIT) method. In this approach, we captured the design of the target for volumetric temperature measurements using an infrared camera and then digitally processed the obtained images to derive a volumetric temperature distribution. We compared the results obtained using the 3D MIT method with those obtained via the SPIV method. The primary advantage of the 3D MIT method, in comparison to other measurement methods, is its capability to simultaneously capture temperature distributions in three-dimensional form (Özer et al., 2019).

In addition to the aforementioned temperature visualization technique, previous studies have utilized the laser induced fluorescence (LIF) method to measure fluid temperature (Bruchhausen et al., 2005; Einecke et al., 2000; Sakakibara & Adrian, 1999). In the LIF method, fluorescent particles are introduced into the flow and illuminated with a powerful laser. The resulting fluorescence is captured using a high-speed camera to determine temperature based on the particles' fluorescence wavelength. However, this method is relatively costly due to the necessary components such as a high-speed camera and lasers. Additionally, precautions are required as the fluorescent particles used are toxic. Another method found in the literature involves the use of thermochromic liquid crystals for whole-field temperature measurement (Dabiri, 2009). Both LIF and thermochromic liquid crystal methods offer the advantage of simultaneously measuring temperature and velocity.

The Rayleigh thermometry method, as described in the literature (Miles & Lempert, 1990), offers a means of determining air temperature. This technique involves seeding the flow with tracer particles and visualizing the flow using laser illumination. Unlike

the LIF method, the Rayleigh method utilizes tracer particles with a smaller wavelength than the transmitted laser, making it susceptible to measurement errors if the flow is contaminated. Due to this sensitivity, the Rayleigh method is only suitable for clean laboratory environments. Furthermore, it is limited to high-temperature applications and requires costly components, similar to the LIF method. Additionally, temperature measurements are constrained to a thin plane when using this method.

1.1.2 Literature Search on Split Air Conditioner

Heat Pumps and SAC are substantial devices for increasing air conditioning demands, especially in tropical and dry climate zones, due to their capability of both heating and cooling. According to The Japan Refrigeration and Air Conditioning Industry Association statistics, in 2021, more than 110 million devices were sold worldwide (Estimates of World Air Conditioner Demand the Japan Refrigeration and Air Conditioning Industry Association, 2022).

These devices have advantages in reducing carbon emissions since they have a Coefficient of Performance (COP) of around four, which means a typical SAC with 3.2 kWh heating capacity uses 0.8 kWh of electricity from the grid. The remaining energy is gathered from the outdoor air, a renewable source (Yücekaya et al., 2023).

The only downside of the SAC in terms of global warming is that the refrigerants used in these devices might include greenhouse gas; however, the new generation of refrigerants that efficiently carry heat and have a lower environmental impact becomes an industrial standard (Calm, 2008). So, in contrast to their previous role, these devices are becoming an important tool to slow climate change.

In order to increase energy efficiency and comfort, it is crucial to investigate the flow and temperature distribution of SAC devices. Although both indoor and outdoor units are critical in terms of energy efficiency, the indoor unit of SAC is more vital since it is located in the living environment and beyond efficiency, it significantly affects thermal comfort. Therefore, it is necessary to evaluate the flow structure and the air temperature distribution in the outlet section of SAC indoor unit for thermal comfort. In addition, the shape of the room, the location of the SACs, the furniture

locations and the environmental conditions (the position and size of the windows, the ambient conditions, etc.) are decisive parameters in the flow of air blown into the room by the air conditioner. However, it is impossible to predict all these parameters and designs using them during production. Therefore, it is necessary to use the most appropriate design method for general usage conditions to develop flexible designs with different flow characteristics.

Numerous studies have been carried out in the field of investigating indoor air, which can be broadly classified into three main categories: theoretical, experimental, and numerical. Fanger (Fanger, 1973) studied the parameters affecting the thermal balance of the human body. As a result of the study, an equation known as the comfort equation was proposed. Fanger (Fanger, 1973) and Wargocki (Wargocki, 1998)worked on indoor climates. These studies presented that indoor air velocity, indoor air temperature, indoor air pollution, and flow patterns influenced the indoor climate. Another parameter that is critical for indoor air quality is air pollution. Air pollution can be produced in the indoor environment as well as brought from the outdoor environment. Nero (Nero, 1988) and Brohus (Brohus, 1997) have studied indoor air pollution. The parameters of these studies are the air pollution produced in the indoor environment, not the air pollution brought indoors from the open air. Awbi's study (Awbi, 1989) revealed how vital thermal comfort and indoor air quality are. In this study, it was found that people spend 90% of their time indoors. This shows that it is crucial to examine indoor air velocity, temperature distribution, and its influence on humans.

For the validation of theoretical and numerical studies in indoor air investigations, experimental studies are necessary. While parameters such as temperature and velocity are analyzed, it is necessary to make measurements with large areas due to spatial and temporal variability. Conventional methods such as thermocouples, thermistors, hot wire anemometers, Laser Doppler Velocimetry and passive gas tracers are frequently used to measure air velocity and air temperature. These methods are capable of point measurement. Therefore, a large number of sensors and labour are needed to examine the entire room. Because of the disadvantages of conventional measurement techniques, PIV method, which allows whole-field velocity measurement, is usually

preferred for velocity measurement in indoor environments (X. Cao et al., 2014). Sun & Zhang (Sun & Zhang, 2007) summarised the methods of studying the motion of air in a room. The methods used to obtain the velocity data were divided to be capable of point measurement and capable of whole-field measurement. The pointwise techniques include Pitot tube and rotating-vane anemometry, which are based on pressure differential principles; hotwire anemometry, hot-film anemometry and hot-sphere anemometry, on heat transfer principles; ultrasonic anemometry (UA), on acoustics principles; and Laser Doppler Velocimetry (LDV), on Doppler shift principles. The whole-field techniques mainly include particle tracking velocimetry (PTV), PSV and PIV, which are based on optical principles. Cao et al. (G. Cao et al., 2010) investigated the turbulent jet flow into the ambient air from the active chilled beam in a climate chamber using PIV. The attached Plane jet with high turbulence intensity and low Reynolds number was investigated quantitatively and instantaneously with PIV. Meslem et al. (Meslem et al., 2010) achieved instantaneous velocity distributions of two different jets using PIV. It has been reported that cross-shaped jets perform much better than circular reference jets for passive control of air-diffusing systems.

The flow characteristic of the air penetrating into the room affects the air distribution in the room. Therefore, in addition to examining the air distribution in the room, it is critical to examine the outlet section of the devices that cause the flow in the room. Karadeniz et al. (Karadeniz et al., 2013) investigated the outlet section flow structure of the indoor unit of the SAC indoor unit in three dimensional. SPIV was used to obtain the three-dimensional flow structure. Besides the examination of the design parameters of the SAC indoor unit, the flow characteristics of the conditioned air penetrating into the room were revealed.

Methods of studying indoor air environments include numerical simulations beside experimental and theoretical methods. Computational Fluid Dynamics (CFD) is foregrounded to examine indoor air environments (Chow, 1996; Jones & Whittle, 1992; Nielsen, 1974, 2015; Zhai, 2006) due to its practicality and the experimental methods' cost, effort and limitations. CFD also has the ability to quickly investigate a large number of parameters, which is a significant advantage due to the

unpredictability of indoor environments, including factors such as the positioning and dimensions of doors and windows, as well as room volume, human presence and Heating, Ventilation and Air Vonditioning (HVAC) devices location.

On the other hand, boundary conditions are one of the most critical points in CFD, especially in indoor air environment analysis. Using real-time data, Wu et al. (Wu et al., 2018) showed that ventilation and indoor temperatures could be adequately predicted with CFD.

However, in most of the studies in the literature, researchers obtain their boundary conditions information through the flow rate data and average temperature of the devices. Then, the velocity and temperature boundary conditions were homogeneously defined at the outlet section of the HVAC devices. In other words, all values defined as boundary conditions along the surface of the outlet region of the devices were considered equal. The comparison between the present study and previous examples from the literature can be seen in Table 1.1.

Table 1.1 Comparison of CFD studies on indoor air environment supported by experiment

	Velocity Profile	**Inlet Boundary Conditions**	**Temperature Profile**	**Temperature Boundary Conditions [K]**
(Posner et al., 2003)	Homogeneously	Velocity-0.235 m/s	Homogeneously	296.15
(Ma et al., 2022)	Homogeneously	Velocity-3 m/s	Homogeneously	313.95
(Andersson et al., 2022)	Homogeneously	Flowrate-70 L/s	Homogeneously	289.65
(Staveckis & Borodinecs, 2021)	Homogeneously	Flowrate-150 m^3/h and 225 m^3/h	Homogeneously	291.15 and 296.15
(Yao et al., 2013)	Homogeneously	Flowrate-0.15 kg/s and 0.2 kg/s	Homogeneously	304.55 and 299.5
(Bulińska & Buliński, 2015)	Homogeneously	Flowrate-0.00812 kg/s	Homogeneously	283.15
(Xu et al., 2023)	Homogeneously	Flowrate-0.2892 kg/s, 0.5784 kg/s	Homogeneously	271.5

(F. Zhang & Ryu, 2021)	Homogeneously	Flowrate-216 m^3/h	Homogeneously	302.15
(Wang et al., 2023)	Homogeneously	Velocity-3 m/s	Homogeneously	308.48
Thesis	The profile was obtained by 715341 measurement points from experimental data.	The volumetric data extracted from the SPIV experiments	The profile was obtained by 100 measurement points from experimental data.	The data extracted from the MIT experiments

In summary, the main aim of indoor air environment analysis is to generate accurate indoor air velocity and temperature distribution. There are many studies in the literature focusing on this subject. However, most of these studies used homogeneous boundary conditions due to the standard measurement method used in the industry (Table 1.1).

The standard capacity test of a SAC aims to measure the total enthalpy change created by the device. Therefore, the outlet section of the SAC indoor unit is placed in front of a nozzle where the average velocity and the average temperature are measured after the flow is fully developed. This captured information can be utilized to derive the air flow rate and the capacity of the device.

However, this data does not include the velocity and temperature distribution information, and in reality, different SAC designs can have significantly different flow structures, which intensely affect the outcome of an indoor air environment analysis.

1.1.3 Literature Search on Combi Boiler

In the 21st century, one of the most critical challenges we face is reducing the energy industry's impact on the climate. It is essential to eliminate gas emissions to address this challenge (Dreizler et al., 2021). According to a report by the International Energy Agency (IEA), CO2 emissions from energy consumption in 2021 reached record levels among total greenhouse gas emissions. In 2021, nearly half of the energy demand for buildings was used for space and water heating, leading to total greenhouse gas emissions of 40.8 Gt of CO2 equivalent. Furthermore, the share of industrial processes and combustion emissions reached 89% in 2021. Additionally, combustion-

related methane and NOx emissions accounted for 10% and 0.7% of total emissions, respectively (Energy Agency, 2021). In Europe, energy used for domestic heating and hot water contributes to one-third of the total energy consumption. Most of this necessary heat is obtained from natural gas at a rate of about 80% (Hinrichs et al., 2018). It is worth noting that there are over 103 million space heaters in the European region, and up to 65% of them are classified as inefficient (Association of European Heating Industry. Heating market report, 2024).

One of the critical parameters affecting energy efficiency and waste gas emission in a combi boiler is the burner structure and the characteristics of the flow in this structure. In burners with premixed combustion, the air and fuel are mixed using a fan before reaching the burner. The flow structure of the premixed mixture is directly affected by both the fan and the channel transmitting to the burner. Experimental studies have shown the impact of this effect, but in numerical studies, modelling the internal structure of the burner and the combustion volume after the burner becomes challenging due to the homogeneous velocity or constant mass flow boundary conditions imposed at the burner inlet, leading to increased error percentages.

Purimetla & Cui (2009) carried out a numerical study to investigate the secondary airflow of the burner in boilers in fossil power plants. In the numerical study, they presented the optimum design for equalising the secondary air flow by defining different mass flow rates to the burner inlet (Purimetla & Cui, 2009).

Zhang et al. (2014) conducted a study optimizing gas mixing in a premixed burner using CFD. To enhance the uniformity of the gas mixture, they employed orifice plates and baffles. The study found that improving the homogeneity of the gas mixture leads to reduced pollutant emissions (T. H. Zhang et al., 2014).

In a study conducted by Zhao et al. (2015), both numerical and experimental analyses were carried out on a premixed cylindrical burner. The research focused on examining and optimizing the geometric parameters of the burner's nozzle. The boundary condition was set as a constant mass flow rate. The results indicate that the newly proposed designs significantly enhance overall performance and minimize waste gas emission. (Zhao et al., 2015).

Meraner et al. (2017) investigated the cold flow characteristics of a burner that can operate with hydrogen and methane-hydrogen mixture by CFD. CFD analyses were performed with different turbulence models. The results obtained with PIV are compared with numerical studies. They concluded that the compatible results obtained for existing burner configurations should be extended to other configurations (Meraner et al., 2018).

Hinrichs et al. (2018) performed CFD analyses for a single burner hole, obtaining numerical results of CO and NO emissions and comparing them with experiments. Due to the use of a single hole, a single inlet condition was defined, and numerical analyses were performed. The results obtained were verified by comparing them with experiments. As a result of the study, the necessity of 3D analysis was emphasised. (Hinrichs et al., 2018).

It's crucial to remember that the assumptions made regarding boundary conditions in numerical studies can constrain the results obtained. These assumptions manifest in the results as a margin of error, making it essential to validate them with experimental studies. Optical flow diagnostics methods offer the potential to yield both quantitative and qualitative insights into the behaviour of the fluid within the burner and combustion zone.

In a study conducted by Legrand et al. (2010), a premixed burner with two different topologies within a specific Reynolds range was experimentally examined using PIV. The burners were categorised as high swirl and low swirl. The experimental data collected were analysed with a focus on flame stability and are recommended for use as validation data, particularly for CFD analyses (Legrand et al., 2010).

Shinomori et al. (2011) experimentally investigated a circulating burner to investigate NOx emissions. They used the PIV method for flow and conventional measurement techniques for temperature O2 and CO. By recirculating the combustion gas in the furnace and increasing the circulation area, a decrease in NOx emission was found (Shinomori et al., 2011).

In reviewing the literature, it is apparent that there has been limited focus on experimental studies pertaining to the burner inlet and the flow structure inside the burner itself, with more emphasis placed on the region after the burner. This has resulted in the assumption of homogeneous distribution as the burner outlet condition in CFD analyses, which has consequently led to an increase in the margin of error in the analyses.

1.1.4 Literature Search on Air Purifier

Indoor air quality is a crucial factor in determining human comfort, whether in individual homes or shared spaces such as shopping centers, schools, and hospitals. The demand for improved indoor air quality has grown significantly in the wake of the pandemic, bringing air purifiers into the spotlight. Air purifiers operate by filtering the existing indoor air through filter to capture particles of specific sizes, before releasing the purified air back into the indoor environment. The performance of key components such as the flow channel, fan, and filter directly influences suction and airflow characteristics. Therefore, both numerical and experimental studies are essential for evaluating the device itself and its impact on the indoor environment.

Kim et al. (2015) conducted a numerical investigation on the airflow within the internal structure of an air purifier using CFD. As a result, they performed computational aeroacoustics (CAA) analyses to obtain aeroacoustic data. The study concluded that optimizing the design of the fan blades led to a reduction of approximately 4.5 dB(A) in total sound. This research underscores the significance of CFD analysis in predicting the fluid-induced noise of such devices (Kim et al., 2015).

Lee et al. (2020) proposed a design for an air purifier to address flow-induced noise caused by fan blades. They used CFD to identify separations in the fan blades. To mitigate the negative effects of this separation on sound and flow rate, they conducted a parametric study on the cut-off angle, radius, clearance, blade number, length, and inlet and outlet angles at specific intervals. The optimal design was then presented based on the findings. Furthermore, a prototype was created from the results and experimentally examined, resulting in a sound reduction of approximately 4.2 dBA (Lee et al., 2020).

Dbouk et al. (2021) examined the impact of domestic air purifier placement on virus transmission within a furnished room using a numerical simulation with OPENFOAM. The study focused on a scenario simulating virus particles at a specific height in the room and assumed a constant flow rate for the boundary condition. The findings indicated that placing the air purifier in the corner of the room reduced the time taken for suspended particles to reach the device, thereby enhancing its effectiveness against the virus. (Dbouk et al., 2021).

Chen et al. (2023) conducted a numerical analysis on an air purifier's efficacy in filtering PM 2.5 particles to address airborne diseases. The study assumed a constant flow rate as a boundary condition and aimed to determine the optimal placement of the air purifier and the most suitable turbulence model. By considering the geometric and semantic information of the rooms, as well as building analyses, the study identified the ideal location for the device, resulting in a 33% increase in its efficiency (K. Chen et al., 2023).

Upon reviewing the literature, it is evident that research has extensively investigated the impact of air purifiers on indoor air quality and flow structures using CFD. However, limitations arise from the absence of fan modeling in these studies and the assumptions of a constant flow rate, leading to inaccuracies in representing the release of air into the environment. Furthermore, the homogeneous suction zone assumption results in an incorrect model of the extraction of polluted air from the environment.

1.2 Aim and Motivation

Household appliances play a crucial role in our daily comfort and energy consumption, with European Union households accounting for 25.8% of total energy usage in 2022. The majority of this energy is utilised for space and water heating, cooling, fresh air needs, and cooking, with heating alone representing 63.5% of total energy expenditure (Eurostat, 2024). Considering the significant impact of household appliances on energy consumption and environmental sustainability, their design and development are of utmost importance for ensuring energy efficiency and user comfort.

The primary objective of this thesis is to investigate and characterize the flow structures within various household devices by utilizing data assimilation techniques in conjunction with optical flow diagnostics as a novel contribution to the literature. This research aims to use and validate advanced optical flow measurement techniques specifically tailored for capturing fluid dynamics in household appliances. By integrating these optical diagnostics with data assimilation methods, the study seeks to enhance the accuracy and resolution of flow visualization and numerical analysis.

The motivation for this research arises from several critical factors. With the growing concern over energy consumption and its environmental impact, there is an urgent need to design household devices that are more energy-efficient. Understanding the flow structures within these devices can lead to significant improvements in their design, reducing energy usage and lowering the carbon footprint of everyday appliances. The performance of household devices is heavily influenced by internal flow structure, and inefficient flow patterns can lead to suboptimal operation, increased wear and tear, and reduced lifespan of the appliances. By gaining a detailed understanding of these flow structures, it is possible to identify and mitigate inefficiencies, thereby enhancing overall performance and durability.

The integration of data assimilation techniques with optical flow diagnostics represents an important approach in fluid dynamics research, providing more accurate and comprehensive data and opening new avenues for the development of advanced diagnostic tools and techniques applicable to various engineering fields. This research also contributes to the broader scientific community by advancing the understanding of complex fluid dynamics in practical, real-world applications, fostering cross-disciplinary innovation and collaboration. By addressing these motivations, the thesis aims to make a meaningful impact on both the academic field of fluid dynamics and the practical realm of engineering, ultimately contributing to a more sustainable and efficient future.

CHAPTER TWO
METHODOLOGY

In the investigation of temperature and velocity data of the fluid, pointwise measurement methods are generally used for ease of use and accessibility. Although these methods are economically advantageous, more is needed to provide information about the physics of 3D flows.

The experimental methods used for the verification of the CFD method, which is frequently used in the investigations of the flow physics of thermal systems, mainly include pointwise measurements. This provides incomplete or inaccurate information, especially when the flow is not homogeneous along the entire boundary region. For this reason, the use of optical volumetric experimental methods instead of pointwise measurements is essential in investigation, development and verification studies.

The input data's reliability directly affects the output's accuracy in artificial neural network methods, which have developed today and started to play a role in design processes. For this reason, the use of volumetric experimental data as input data increases reliability. In addition, if numerical input is given, supporting it with experimental data significantly reduces the error margin of the predictions.

Considering all these parameters, SPIV, which provides volumetric temperature and velocity data, and MIT, which provides volumetric temperature data, were used in this thesis, and the details are explained in Chapters 2.1 and 2.2.

2.1 Particle Image Velocimetry

PIV is a sophisticated experimental technique within the realm of fluid mechanics, designed to unravel the intricate details of fluid flow behavior. This method facilitates the visualization and quantitative analysis of fluid motion by employing tiny tracer particles suspended in the fluid under investigation. Through the use of high-speed imaging, researchers capture successive frames, enabling the tracking of these particles' movement over time.

The primary objective of PIV is to extract velocity information at numerous points within the fluid, generating comprehensive velocity fields. This dataset offers insights into the complex dynamics of fluid motion, shedding light on phenomena such as turbulence, vortices, and boundary layer interactions. PIV's versatility extends its applications across various scientific domains, including aerodynamics, hydrodynamics, biomedical engineering, and environmental fluid dynamics.

In applying the method, the fluid to be inspected is first seeded with a tracer particle. The reason for this is that the light reflected from the particles moving in harmony with the fluid to be examined can be captured by the cameras. At this stage, particle selection is essential because the particle density should be compatible with the density of the fluid to be investigated. Otherwise, the results of the experiment may provide inaccurate data as they are the result of the movement of the particles. A high-power light source, usually a laser, is used to illuminate the particles. The light source creates a plane in the space under investigation and allows data to be acquired through this plane. Conventional PIV methods use a single camera to acquire 2-dimensional and 2-component data from this plane. In the SPIV method used in this thesis, two cameras can be used to obtain 2-dimensional 3-component velocity data. Since this provides velocity data of the third component of the flow, it provides a more detailed examination of the physics of the study area. Figure 2.1 shows a schematic representation of SPIV.

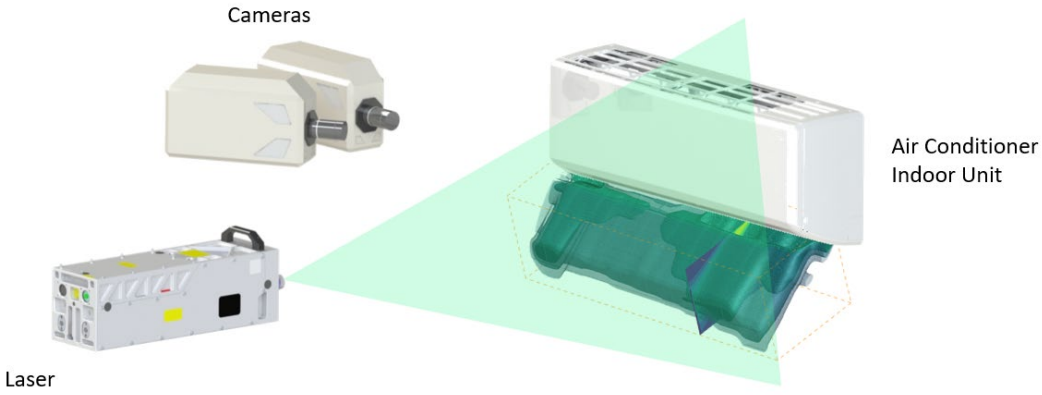


Figure 2.1 The schematic of SPIV setup (Yücekaya et al., 2023)

2.1.1 Stereo Particle Image Velocimetry Components

The PIV system usually consists of 5 main components. These are; camera and lenses, illumination unit (usually laser), synchronizer, fog generator and particles, software and computer.

PIV is an indirect measurement method that involves using cameras to display seeding particles. Seeding particles are a vital component of PIV systems, as they must accurately follow the flow behaviour of the fluid under investigation. Failure to do so will result in inaccurate data that does not represent the actual flow behaviour. The choice of seeding particles is a function of the fluid nature. Glass beads, polystyrene, aluminium flakes, or oil droplets are commonly used for macro PIV investigations. The refractive index of the particles must differ from that of the flow to enable laser scattering from the particles to the camera. Particle dimensions are critical to the success of PIV experiments. They must be large enough to reflect a significant portion of the laser light and small enough to follow the fluid motion within the response time. In PIV applications, seeding particles with a diameter ranging from 10 to 100 micrometers are typically used. Post-process analysis of PIV images involves measuring displacement using cross-correlation. Accurate displacement measurements require proper particle density distribution. Figure 2.2 displays different particle densities, with image (b) showing the optimal particle density for PIV applications. However, infrequent particle distribution, as shown in image (b), cannot provide velocity information. In contrast, image (c) has a very dense particle distribution, making it challenging to determine questioning areas accurately.

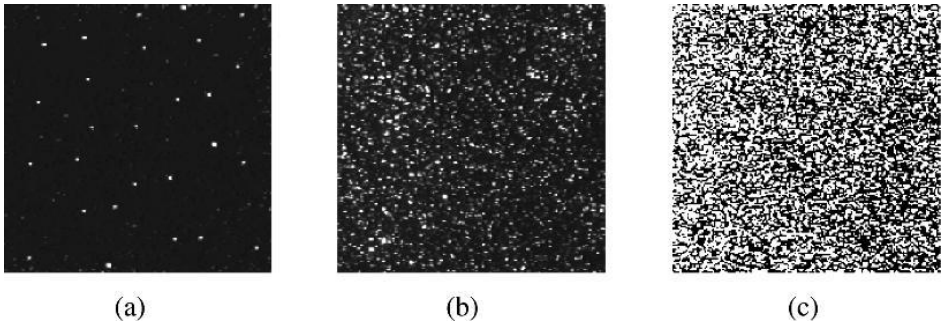


Figure 2.2 Different particle distribution densities (Raffel et al., 2007)

Since the SAC, air purifier, and burner system examined in the experiments included air as a fluid, mist compatible with air is used as a particle. In addition, a fog generator (SAFEX FOG 2010) is used to seed the investigation volume.

An illumination unit is needed to illuminate the particles added to the investigation volume. Lasers are a popular choice for PIV illumination unit because they emit monochromatic light with high energy density that can be easily focused into thin light sheets. This enables the illumination and recording of tracer particles without any chromatic aberrations, resulting in high-quality data (Raffel et al., 2007).

Lasers work on the principle of amplifying light through stimulated emission of radiation. This process starts in a specially designed chamber known as the gain medium, which contains atoms or molecules capable of being excited to higher energy states.

Within the gain medium, atoms or molecules are pumped with energy from an external source, such as electrical discharge or another laser. When a photon—a tiny packet of light—collides with one of these excited atoms or molecules, it triggers a cascade of events. The excited atom promptly releases its excess energy in the form of a new photon. This emitted photon is not just any ordinary photon; it's a clone of the stimulating photon, possessing identical properties such as frequency, phase, and polarization.

This phenomenon, known as stimulated emission, is the key to laser operation (Figure 2.3). The newly spawned photons don't stop there. They careen through the gain medium, colliding with more excited atoms and setting off a chain reaction of emission and amplification. With each collision, the army of photons grows exponentially.

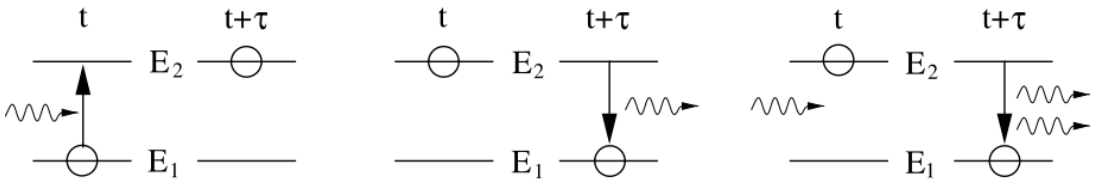


Figure 2.3 Elementary kinds of interactions between atoms and electromagnetic radiation (Raffel et al., 2007)

Neodymium-Doped Yttrium Aluminum Garnet (ND:YAG) lasers are frequently used in PIV applications. ND:YAG lasers are also used in this thesis.

Named for its active medium—a combination of Neodymium-doped Yttrium Aluminium Garnet crystals—the ND:YAG laser boasts remarkable optical properties ideal for PIV applications.

The ND:YAG laser harnesses the power of neodymium ions doped within a crystalline matrix of yttrium aluminium garnet. This composite structure enables the laser to emit high-energy light pulses with remarkable precision and stability, characteristics essential for the demanding requirements of PIV experiments.

One of the standout features of the ND:YAG laser lies in its ability to emit light at a wavelength of 1064 nanometers—a sweet spot within the electromagnetic spectrum for PIV applications. This wavelength offers optimal penetration through dense fluids and allows for the efficient illumination of tracer particles suspended within the fluid flow.

In the context of PIV, the ND:YAG laser serves as the beacon of light, illuminating the fluid under investigation with short-duration pulses of intense light. These pulses effectively freeze the motion of tracer particles within the fluid, enabling high-speed cameras to capture successive images of the particle displacements.

Moreover, the ND:YAG laser's pulsed operation facilitates precise synchronization with the camera's exposure time, ensuring clear and distinct particle images without motion blur. This synchronization is crucial for accurately measuring particle velocities and mapping fluid flow fields with exceptional spatial and temporal

resolution. The laser used in this thesis (Litron 135 mJ, 15 Fps double pulsed Nd:YAG Laser) is shown in Figure 2.4.

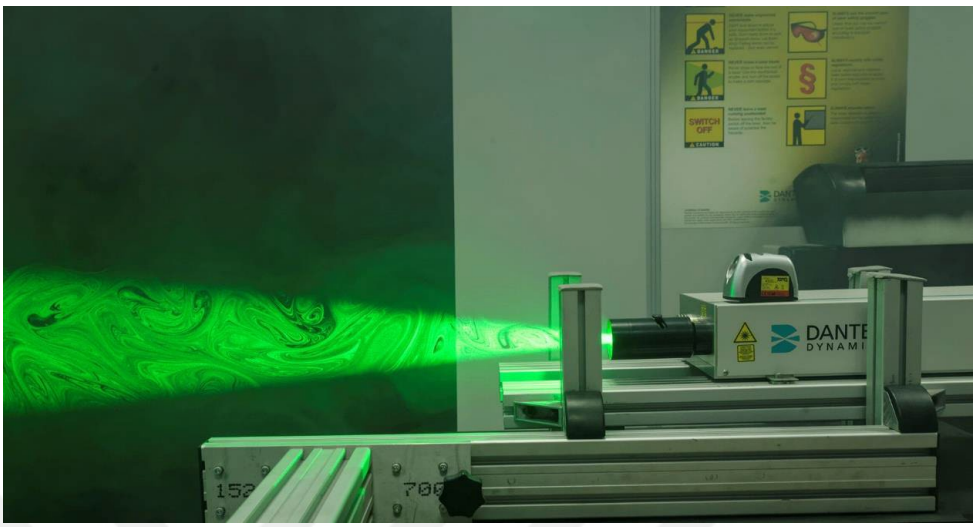


Figure 2.4 The ND:YAG Laser used in the experiments (Özer, 2017)

High-speed cameras are used in PIV applications to image the displacement of laser-illuminated particles (Figure 2.5). These cameras can use CCD or CMOS sensors. While CCD sensors traditionally offered higher image quality and lower noise levels, CMOS sensors have made significant strides in recent years, offering competitive performance with lower power consumption and faster readout speeds. Both sensor types are employed in PIV cameras, chosen based on factors such as cost, sensitivity, and application requirements.



Figure 2.5 The cameras used in the experiments (Özer, 2017)

Unlike conventional cameras, PIV applications require capturing multiple images in rapid succession. This is because PIV relies on measuring the displacement of tracer particles between frames. High-speed cameras, capable of thousands of frames per second, are ideal for this purpose. In addition, the particles may not fill a pixel due to their size, but the light reflected from the particles can be captured by the cameras because it is larger than the pixel size. The resolution of the cameras is also important in order to capture the light reflected from the particles in more detail. For this reason, cameras are required to have high spatial resolution.

Fluid flow phenomena can span a wide range of intensities, from areas of high particle concentration to regions with minimal particle density. Cameras used in PIV applications are equipped with a wide dynamic range, allowing them to accurately capture both bright and dim regions within the same image without loss of detail or saturation.

When all these features are evaluated, PIV applications should have high speed frame rate capacity. In the experiments conducted within the scope of the thesis, 2 Flowsense cameras with 4 MPx resolution and 60 mm f2 Zeiss Planar Macro Lens were used (Figure 2.5).

A synchronizer device is used for the cameras to capture images during the nanoseconds when the laser pulses. By using the synchronizer, illumination and image capture can be simultaneous and the particle motions required for the experiment can be imaged.

The final phase of the experiment is the computer processing of the acquired images. The pair of images of the fluid obtained during the experiment is divided into investigation areas. The particle arrangement in the investigation area in the first image is searched in the second image and the investigation area with the highest similarity is detected in the image. This process is called cross-correlation. In this way, the displacement and time information of the fluid is obtained and velocity vectors are calculated.

2.2 Meshed Infrared Thermography

Measurement screen methods for measuring temperature distribution in gaseous media are typically based on infrared thermography. This is because gases are transparent at infrared wavelengths (7-13 μm). These methods are considered indirect measurement techniques, and the accuracy of the measurement largely depends on the relationship between the target and flow structure. To obtain reliable results, the target should exhibit a temperature distribution that is similar to that of the surrounding air, while also minimizing any flow distortions.

In heat transfer, convection is the primary mechanism of heat transfer between the target and the gas. Therefore, the target must be designed in such a way as to enhance this mechanism and reduce the other heat transfer mechanisms. For instance, plane measurement screens have a wide surface area that causes radiative heat transfer with the surrounding atmosphere. These screens also have conductive heat transfer among themselves. Therefore, the temperature distribution obtained from a plane measurement screen depends on the convection with investigated gas, radiation with surrounding, and conduction among the screens. As a result, the temperature distribution obtained from a plane screen cannot directly represent the temperature distribution of the investigated gas.

The installation of measurement screens in the flow area can cause distortion effects on the flow structure, which in turn can lead to inaccuracies in temperature measurements. The extent of this distortion is a critical factor, as excessive deformation can result in the measurement of an irrelevant flow structure instead of the intended one. Therefore, it is essential to carefully consider the impact of measurement screens on flow structure and take appropriate measures to ensure accurate measurements.

A new measurement screen called "Three-Dimensional Meshed Infrared Thermography (3D MIT)" has been designed to handle various effects (Özer et al., 2019). This method uses spheres placed on carrier ropes that are stretched between two parallel plates connected to foot stands. Together, these components form the volumetric temperature measurement target (as shown in Figure 2.6).

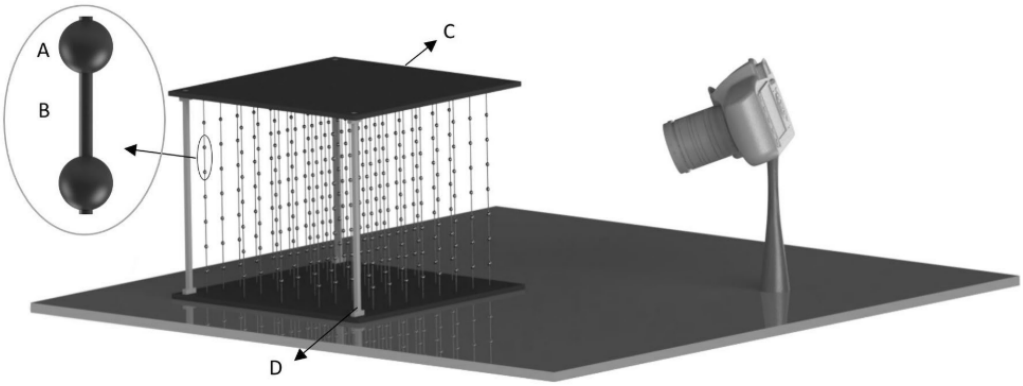


Figure 2.6 3D MIT setup (Özer et al., 2019)

The positioning of the spheres (Area A in Fig. 2.6) on the carrier ropes between two parallel plates (Area C in Fig. 2.6) is a crucial aspect of measuring temperature in fluid dynamics. The positioning of the ropes (Area B in Fig. 2.6) is dependent on the size of the spheres and the velocity of the flow. The carrier ropes have two significant parameters, namely their thermal conductivity and diameter. The ropes' thermal conductivity must be minimized to avoid conductive heat transfer between the spheres. Additionally, the diameter of the ropes should be lessened to reduce flow distortion. However, the ropes must possess adequate rigidity to hold the spheres in place. The primary issue with the spheres' movement is the motion blur effects on the infrared image, leading to inaccurate temperature measurements and extra turbulence in the flow. To reduce these challenges, it is essential to ensure that the spheres are fixed in position to avoid flickering while exposed to the stream, and the image can be taken clearly.

The use of a single camera to capture a two-dimensional image can't provide three-dimensional data. That's why typically two cameras are used to obtain 3D data. However, in the presented method, the sphere’s locations are fixed and known, along with the measurement mesh locations in three-dimensional space. Consequently, the image obtained from the thermal camera is only used for matching and temperature measurements. Thus, 3D measurements can be performed with a single camera. The plates and supporting beams serve as the mechanical carriers of the spheres and the ropes. They are the skeleton of the system. Proper positioning is necessary to avoid any disturbances in the flow and to ensure the camera's view is not blocked.

The geometries, size, and location of the spheres are the most critical parameters of the system. The spheres' symmetric geometry has an added advantage. The area projected perpendicular to the free stream velocity parameter (Af) in the drag coefficient formula (Eq. 2.1) (Incropera et al., 2007) remains the same for different attack angles. This also implies that the flow deformation for every attack angle will not be affected by the target's geometry. The proposed symmetric geometry has advantages for thermal imaging too. Spheres have the same view area from all angles. Therefore, spheres are more suitable than planes and porous targets for three-dimensional flow measurements and volumetric measurements.

$$C_d = \frac{F_d}{A_f(\rho V^2/2)} \tag{2.1}$$

In 3D MIT, the diameter of spheres plays a critical role. As the size of each sphere increases, it increases the flow deformation and affects the location of the subsequent sphere. It is expected that the flow deformation caused by a sphere will damp out before reaching other spheres in ideal cases. Therefore, if the flow deformation increases due to an increase in sphere diameter or flow velocity, the spheres must be positioned more sparsely. Similarly, decreasing the diameter of the spheres has beneficial flow effects but makes temperature measurements harder. In digital imaging, the light-sensitive area is divided into sensor areas called pixels. These sensors capture the light that focuses on them, and the collected data is evaluated and converted to an image. In infrared images, pixels represent temperature values instead of light intensity or color data. For a precise temperature measurement, a pixel must be filled by the target surface. Otherwise, it would measure an area-weighted average of the target and the background. In such cases, subpixel algorithms must be used to obtain the target temperature. In Fig. 2.7, this phenomenon is shown.

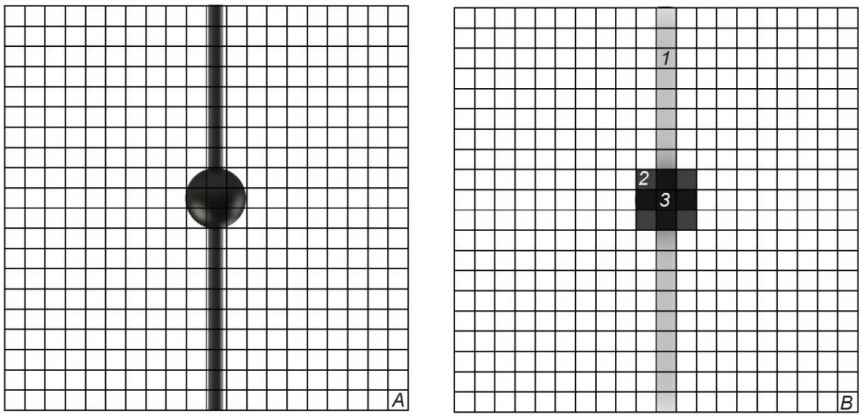


Figure 2.7 a)Target projection on the sensor and b) Simulated temperature map (Özer et al., 2019)

Subpixel algorithms are widely used for various applications, including image remapping and enhancing the accuracy of PIV experiments. They can also be applied to improve the accuracy of 3D MIT and high-porosity mesh methods. However, it's crucial to have accurate knowledge of the background temperature for efficient application. It's worth noting that the background may have different surface emissivity or eccentric temperature distribution, which can make the application of this method complex and unreliable.

In order to perform direct measurements, it is necessary to determine the minimum number of pixels that must be covered by the measurement sphere in the thermal image. This value, denoted as 'n', should be chosen such that at least one pixel in the image is filled by the sphere. It is recommended that 'n' should be 3 or greater, taking into consideration the fact that in real thermal images, not all spheres are concentric with pixels. According to Hirasawa et al., (2015), the measurement spot should be imaged by an area of at least 6 x 6 pixels. This relationship between the sphere's size, the image resolution, the sensor size, and the focal length of the lens is depicted in Figure 2.8, and can be mathematically described using the Eq. 2.2., Eq. 2.3 and Eq. 2.4.

$$\frac{L_R}{d} = \frac{L_S}{f} \tag{2.2}$$

$$S_f = \frac{L_R}{P\#} = \frac{D_{sphere}}{P\#_{sphere}} \tag{2.3}$$

$$d = \frac{D_{sphere} P\#}{P\#_{sphere} L_S} f \quad (P\#_{sphere} \geq n) \tag{2.4}$$

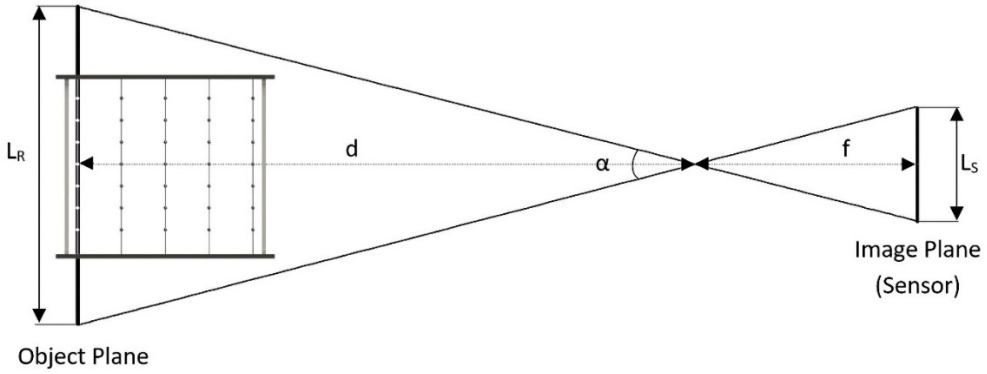


Figure 2.8 Optical schematic of the proposed 3DMIT setup (Özer et al., 2019)

The scale factor (Sf) defines the area of a pixel corresponding to the object plane, and it depends on various factors, including the focal length of the lens (f), the size of the sensor (LS), the pixel number of the camera on the related axis (P#), and the distance between the camera and the object plane (d). The angle of view (AOV) (α) of the lens is also determined by the focal length of the lens and the size of the sensor. These equations can be used to determine the size of the analyzed volume and the size of the investigation spheres based on the camera and lens specifications. However, the distance between the camera and the object plane is also related to the depth of field.

Lenses focus light from a certain distance known as the focusing distance (s), resulting in images of objects at these distances with maximum sharpness allowed by the lens. However, as objects move away from or closer to the lens from this distance, the area scattered in the image plane by light coming from a single point expands. The diameter of this scattered area, known as the permissible diameter of the circle of confusion (COC), cannot be visually observed and does not negatively affect the technical process. This concept is well-explained by (Minkina & Dudzik, 2009). The region close enough to the focusing distance such that the diameter of the scattered area of light coming from a point source is smaller than the COC is considered focused, and this area is referred to as the depth of field. The formulas related to the depth of field are provided in Equations 2.5, 2.6, 2.7, and 2.8 (Jacobson, 1978). Hyper-focal (H) is the closest distance that rays from a point can reach the lens parallel only. It is

also utilized for calculating the depth of field (DOF). The near focus distance (D_N) is the closest object distance that can be focused on the image, and the far focus distance (D_F) is the farthest distance that can be focused on the image. DOF refers to the total distance between D_F and D_N.

$$H = \frac{f^2}{N \cdot c} + f \tag{2.6}$$

$$D_N = \frac{H \cdot s}{H + s} \tag{2.7}$$

$$D_F = \frac{H \cdot s}{H - s} \tag{2.8}$$

$$DOF = \frac{2H \cdot s^2}{H^2 - s^2} \tag{2.9}$$

In thermal imaging, the lack of focusing or blurriness leads to the intermingling of temperature information from different points, resulting in an incorrect measurement of temperature. This error caused by defocusing is not fixed and is directly related to the temperature differences in the measured areas. As the temperature difference of blended pixels increases, the temperature error also increases. However, if a constant temperature target with no temperature gradient is imaged, defocusing would not cause any measurement error. To minimize blurriness, the circle of confusion (COC) should be as small as possible according to the pixel size of the sensor. In most thermal cameras, the aperture number (N) and focal length (f) parameters are not configurable, making the focusing distance (s) the primary adjustable parameter for arranging the depth of field in which the 3D MIT target must fit. Therefore, it is necessary to ensure that the distance between the lens and the object plane (d) obtained from Eq. 2.5 is compatible with the calculation of depth of field (DOF) in Eq. 2.9. The impact of this is that the spheres should be small enough to minimize flow distortions but large enough to be captured by the infrared camera.

If the infrared camera technology has higher resolution, smaller spheres can be used, and in some cases, even wires can be used for measurement. However, at present, the resolution of conventional infrared cameras is not sufficient to achieve direct measurement from wires.

2.2.1 Validation of Three Dimensional Meshed Infrared Thermography Method

The present study employed thermocouples to validate the temperatures obtained via the 3D MIT method by conducting a comparative experiment. The 3D MIT target was placed at the exit of a cross-flow fan (CFF) that drives hot air as displayed in Figure 2.9. The dimensions of the exit of the CFF were measured as 180 × 40 mm^2, and the Reynolds number of the flow was calculated to be 4880 (Lazzarotto et al. 2001) [(n) rotational speed of fan (rpm), (D) impeller external diameter (mm), (cb) blade chord (mm) and (v) kinematic viscosity (m^2/s)].

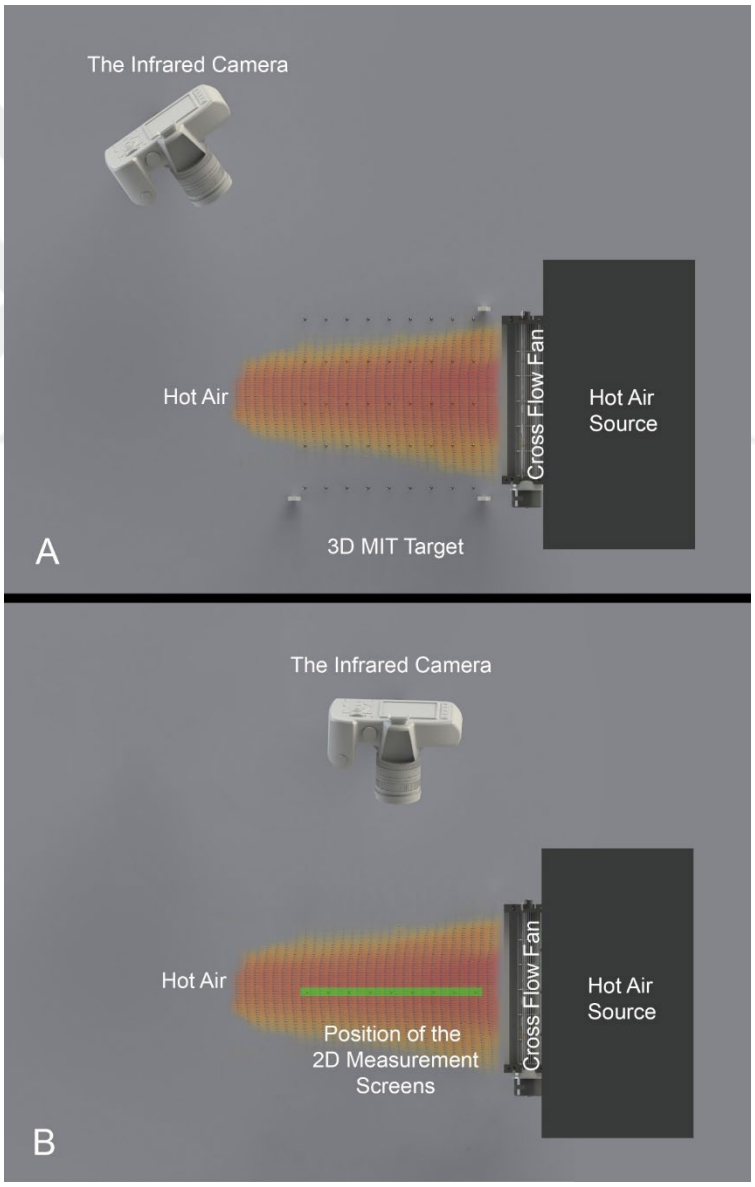


Figure 2.9 The schematic of the experimental setups. a) 3D MIT experimental setup b) 2D measurement screens experimental setup (Özer et al., 2019)

To minimize experimental errors, K-type thermocouples were utilized, and a constant temperature water bath was used to test them before the validation study. It was observed that the absolute difference from the bath temperature was between 0.1 and 0.5 K, while the standard deviation of the measured temperatures from the different thermocouples was 0.15 K.

In order to validate the experiment, thermocouples were placed beside five of the measurement spheres, which were positioned on a straight line that went through the center of the fan exit area perpendicularly. The distance between the validation points was measured as 25 mm. Temperature measurements were performed with thermocouples and via the 3D MIT method simultaneously, and the validation experiments were repeated five times. The linear regression fitting results between the 3D MIT and the thermocouple measurements are presented in Fig. 2.10.

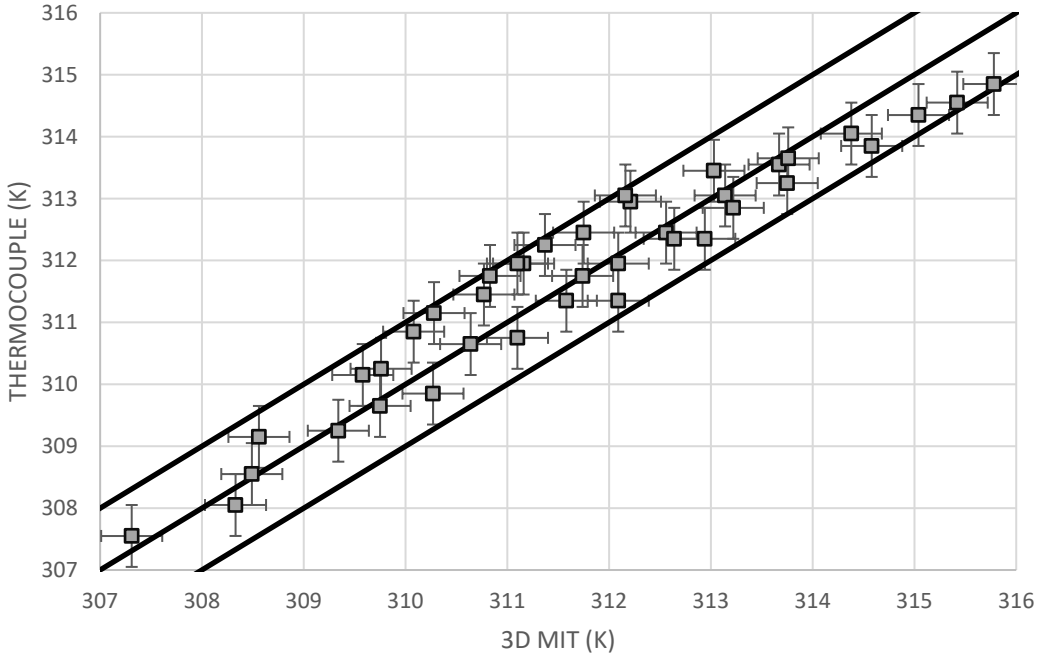


Figure 2.10 Linear regression fitting between the measurements of both validation experiments (Özer et al., 2019)

Upon examining all the data presented in Fig. 2.10, it was determined that the maximum error was less than 1 K. The absolute difference values between the thermocouple and the 3D MIT measurements varied from 0.01 to 0.93 K. The average

difference between the two experiments was 0.06 K, and the standard deviation of the absolute differences for all the measurement nodes was 0.3 K.

After analyzing the results, it can be concluded that the 3D MIT results are in good agreement with the thermocouple measurements, indicating that the 3D MIT method is advantageous for both measuring and visualizing temperature distribution.

To validate the 3D MIT method in terms of 3D flow structure, we utilized the data obtained from the measurement mesh to reconstruct the volumetric temperature distribution using the 3D MIT method. To achieve this, we matched the temperatures of the 315 spheres in the thermal image of the target to their positions in three-dimensional space. This can be done either manually or via automated algorithms, taking advantage of the fixed geometry of the measurement target. The measured temperatures were then positioned in virtual 3D media for visualization, and isotemperature surfaces were calculated to obtain a clearer view, as shown in Figure 2.11-A. We also used the SPIV method to reconstruct the average volumetric velocity isosurfaces and validate and compare the flow structure, as demonstrated in Figure 2.11-B. For this, we selected 16 equally spaced measurement planes throughout the outlet of the CFF (15 mm intervals through 0 mm to 180 mm) and carried out SPIV experiments in these planes to obtain two-dimensional three-component velocity maps for each measurement plane. We then placed the gathered data planes sequentially within a three-dimensional space in a virtual environment and interpolated them to form the average three-dimensional flow field of the CFF.

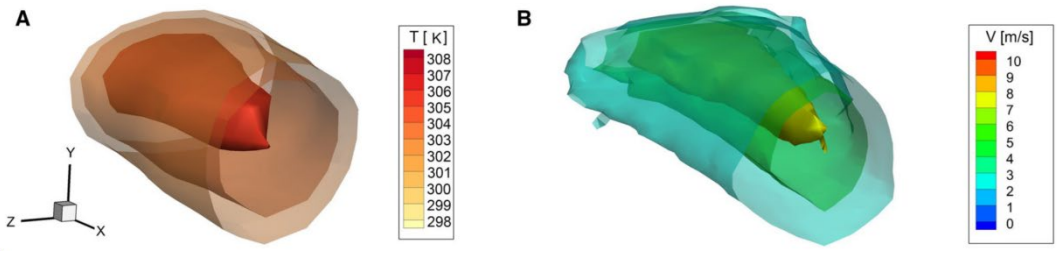


Figure 2.11 a) Average volumetric temperature isosurfaces of the CFF obtained via 3D MIT. b) Average volumetric velocity isosurfaces of the CFF obtained via PIV (Özer et al., 2019)

It is important to note that while the 3D MIT method measures temperature and the SPIV method measures velocity, a quantitative comparison between these results

cannot be made. This is because a hot jet blown into stationary air loses both its temperature and velocity as it mixes with the surrounding air. As a result, the temperature and velocity iso-surface measurements would be similar to each other in a geometrical sense, as observed in Figures 2.11-a and 2.11-b.

Based on our findings, we conclude that the 3D MIT method can be effectively employed to investigate 3D flow characteristics.

CHAPTER THREE
EXPERIMENTAL AND NUMERICAL INVESTIGATION OF AIR CONDITIONER

One of the most important parameters when designing SAC is the effect of the outlet section into the room. As detailed in Section 1.1.2, there are many studies on these investigations in the literature. The main objective of these studies is both to improve air conditioner designs and to generate accurate indoor air velocity and temperature distribution. However, most of these studies used homogeneous boundary conditions due to the standard measurement method used in the industry.

The standard capacity test of a SAC aims to measure the total enthalpy change created by the device. Therefore, the outlet section of the SAC indoor unit is placed in front of a nozzle where the average velocity and the average temperature are measured after the flow is fully developed. This captured information can be utilized to derive the air flow rate and the capacity of the device.

However, this data does not include the velocity and temperature distribution information, and in reality, different SAC designs can have significantly different flow structures, which intensely affect the outcome of an indoor air environment analysis.

The significant difference between using homogenous boundary conditions versus using boundary conditions that are obtained by the data assimilation of multiple optical volumetric experimental methods is presented sub-chapters of Chapter 3.

The volumetric, three-component average velocity data were obtained by the SPIV method at the outlet section of the SAC indoor unit and the temperature distribution in the same region was investigated with the MIT method (Özer et al., 2019) and detailed information on the SPIV and MIT experiments is given in Section 3.1.

The results of these two experiment methods aligned in a digital space to generate the three-dimensional temperature and velocity profile of the outlet section of the SAC indoor unit to define the boundary conditions of the steady-state and time-dependent CFD simulations. This data assimilation implementation allowed the local and

volumetric effects in the investigated regions to be applied as a boundary condition. The detailed information on the CFD is given in Section 3.2.

This new approach to CFD was validated with three-dimensional experimental data and compared with the conventional CFD methods, where the average velocity and temperature were defined as the homogenous boundary conditions. The detailed information on the validation is given in Section 3.3.

The results of the CFD generated by data assimilation and the comparison with the CFD generated by conventional methods are presented in Section 3.4.

3.1 Stereo Particle Image Velocimetry and Meshed Infrared Thermography Experiments to Investigate Split Air Conditioner Indoor Unit Outlet Section

Two experimental techniques were utilized to acquire the air temperature and velocity values at the outlet section of the SAC indoor unit. Specifically, the MIT method was employed to obtain the temperature distribution, while the SPIV method was utilized to determine the velocity distribution.

3.1.1 Temperature Measurement: Meshed Infrared Thermography

Infrared imaging can only measure the temperatures of objects that are opaque at the infrared wavelength and radiate with a definitive emissivity coefficient. However, gases such as air are transparent in the infrared wavelength (7-13 μm). For this reason, the infrared camera cannot directly determine the temperatures of the gases. Measurement screen methods are used in the literature to solve this problem (Anderson et al., 1991; Cehlin et al., 2002; Vinnichenko et al., 2017).

Our research team obtained the simultaneous volumetric temperature distribution of infrared-transparent flows (air, gases, etc.) with the method called three-dimensional MIT, with a negligible flow distortion (Özer et al., 2019) . This method was also used in the thesis study to obtain the temperature distributions in the SAC indoor unit's outlet section.

While applying the method, the measurement target was placed at the SAC outlet section, and temperature values were obtained from the spheres on the target (Figure 3.1).

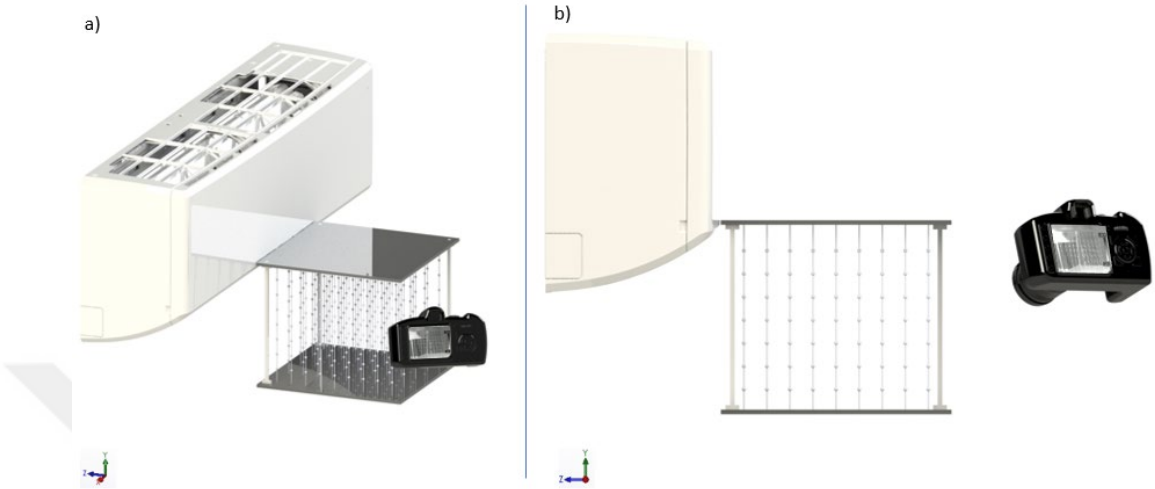


Figure 3.1 MIT experiment setup a) Isometric view b) Left view (Yücekaya et al., 2023)

The target placed in the SAC outlet section was exposed to the air coming out of the SAC until the spheres on the target reached equilibrium in terms of temperature. After that, images were taken with a thermal camera. The experiment was sequentially conducted four times by translating the MIT target in order to fully cover the temperature distribution at the outlet of SAC, which was larger than the target area. The temperatures of the spheres were recorded during these experiments, and the temperature distribution was subsequently interpolated and created using the corresponding positional data, as depicted in Figure 3.2.

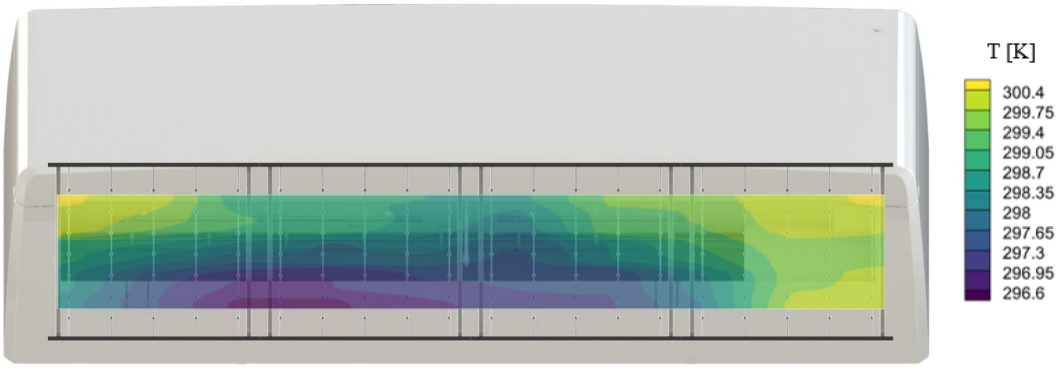


Figure 3.2 SAC indoor unit outlet section MIT experiment results (Yücekaya et al., 2023)

3.1.2 Velocity Measurement: Stereo Particle Image Velocimetry

PIV is an advanced non-intrusive, and whole-field flow visualization method that can be used for qualitative and quantitative investigation. In this method, the flow is seeded by tracer particles which move coherently with the fluid. Then the seeded flow is consecutively illuminated by lasers and imaged by PIV cameras (Raffel et al., 2007).

SPIV was used to obtained 3 component 3 dimensional velocity data. This method uses a two-camera experiment system to capture two-dimensional three-component velocity data and eliminate perspective errors.

A schematic representation of the SPIV setup is given in Figure 2.1. Experiment setup consist of the SPIV system utilized a pair of Flowsense 4 MPx cameras equipped with 60 mm f2 Zeiss Planar Macro lenses, a Litron 135 mJ double pulse Nd:YAG Laser operating at 15 frames per second, a SAFEX FOG 2010 fog generator, a synchronizer, and a workstation with accompanying software for component control and post-processing. The SAC's indoor unit was placed on a translation stage system, allowing accurate examination at regular parallel investigation planes.

The jet flow was investigated in 11 planes (Figure 3.3) to create the volumetric three-dimensional average velocity distribution, which was obtained through the application of the Kriging interpolation (De Baar et al., 2014) method. The number of planes utilized for investigation was determined to be sufficient for representing the outlet section of the SAC indoor unit in the prior studies conducted by the research team (Karadeniz et al., 2013; Kumlutaş et al., 2013). It is important to note that the number of planes can be increased based on the researchers' availability of time and the number of elements utilized in the boundary condition mesh.

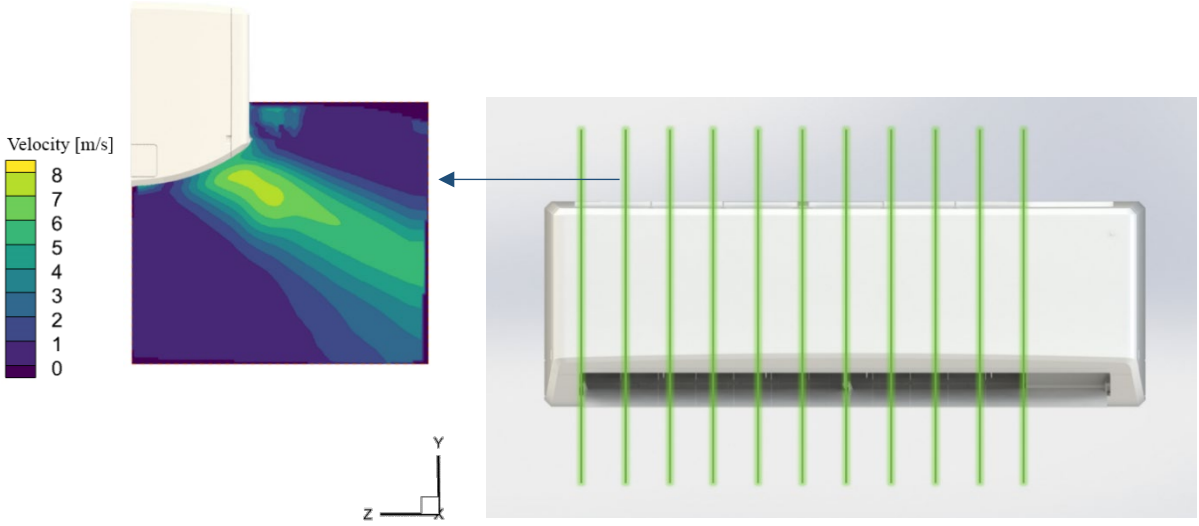


Figure 3.3 SPIV investigation planes and SPIV velocity distribution result of the z= 742.5 mm plane (Yücekaya et al., 2023)

The resulting volumetric velocity distribution of the examined SAC indoor unit is presented in Figure 3.4.

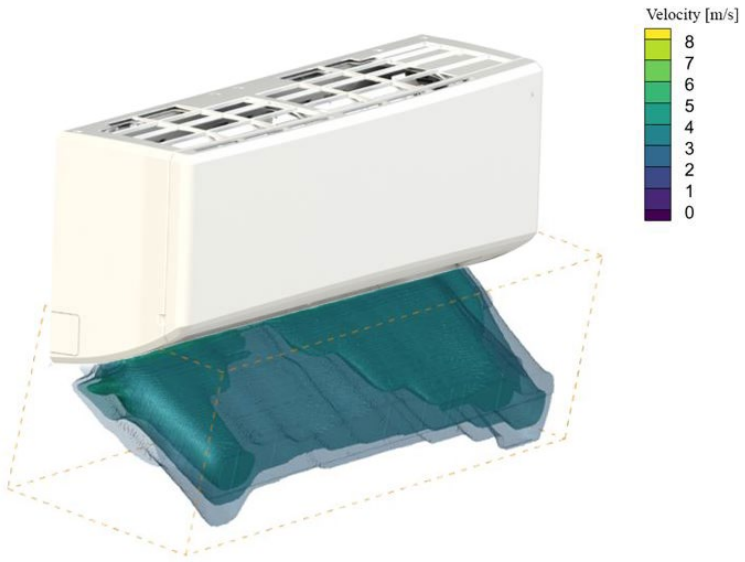


Figure 3.4 Average volumetric velocity iso-surfaces 3m/s, 4 m/s and 5 m/s at the outlet section of the SAC indoor unit obtained by SPIV (Yücekaya et al., 2023)

The outlet section of the SAC indoor unit exhibits a double-peaked velocity profile as a result of the crossflow fan's blowing behaviour. This phenomenon is attributed to the presence of secondary flows moving in opposite directions along the z-axis, which

intersect near the centre of the jet flow and divide it into two sections in the previous study of the current research group (Karadeniz et al., 2013). This results in the observed double-peaked velocity profile.

3.2 Numerical Study of the Split Air Conditioner Indoor Air Effect

In order to investigate the velocity and temperature distribution in the room, the SAC indoor unit CAD model was placed in the room geometry created in the ANSYS-CFX (ANSYS Inc., 2011) program. According to ISO 5151 standard (Non-ducted air conditioners and heat pumps — Testing and rating for performance) (Non-Ducted Air Conditioners and Heat Pumps-Testing and Rating for Performance: ISO 5151, 2017), the minimum recommended dimensions for a room with a power rating of 6000 W are 2.4 m in width, 2.1 m in height, and 2.4 m in length. The dimensions of the modelled room were 3 m x 5 m x 5.5 m to match the experiment room, as shown in Figure 3.5. The SAC was positioned 2.5 m above the floor and in the middle part of the 5 m wall. There is a difference of approximately 97 mm between the middle of the SAC indoor unit outlet section and the middle of the SAC indoor unit due to the fan motor and the electronic parts positioned on the right side of the device. So, since the SAC indoor unit was placed in the middle of the room, the midpoint of the outlet section of the SAC indoor unit was at a distance of 97 mm from the centre of the room.

The effect of the SAC's position on the flow structure in the room wasn't selected as a parameter. The position of the SAC indoor unit is one of the most studied parameters for thermal comfort in an indoor environment. However, one of the main arguments of this study points out that using boundary conditions homogenously defining the flow rate information of the device is significantly misleading.

To prove this theory, the study was utilized with transient LES model. The position of the SAC was kept constant as the standard experiment room for more robust validation. The air volume of the three-dimensional room model and the location of the air conditioner model are shown in Figure 3.5.

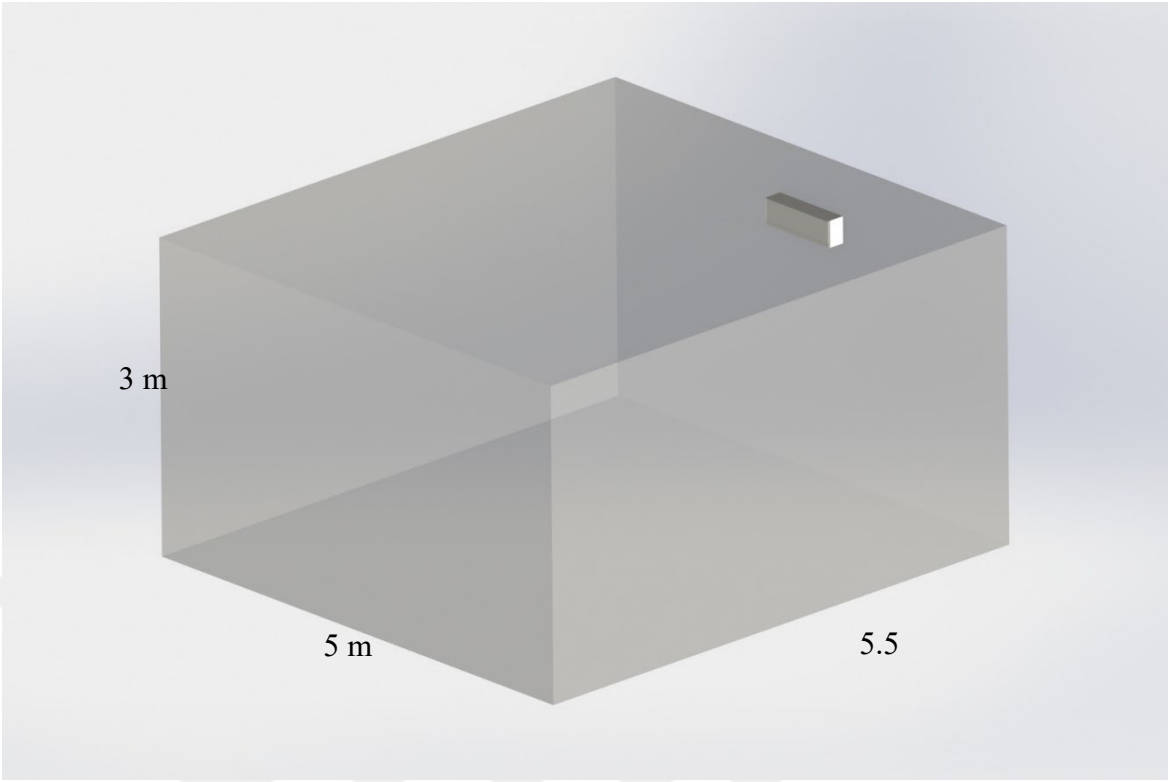


Figure 3.5 The air volume of the three-dimensional room model (Yücekaya et al., 2023)

The mesh structure has an important role in CFD analysis to simulate jet flows realistically. Mesh parameters such as the size, y^+, and orthogonal quality can directly affect the results of the analysis. In addition, the mesh structure can also affect criteria such as CPU time and analysis convergence for analysis.

Numerical simulations of the three-dimensional air temperature and velocity fields were performed using ANSYS CFX, a commercial CFD software. This program also was utilized to generate mesh structure.

While applying data assimilation to the CFD, the most critical point is having a dense enough mesh structure that will match the data points generated by the combination of experimental methods. On the other hand, the volume in numerical room models is relatively extremely larger than the outlet section of the SAC indoor unit. So if the researchers keep the same mesh size, the number of mesh becomes unsolvable, or researchers might apply inflation, which might end up with the minimum and maximum element size ratio significantly exceeding the suggested

values. Therefore, optimum mesh sizing and number should be decided by balancing the number of data points from the experiments and computer resources.

The mesh structures were created using tetrahedral elements. Models with different element numbers were analyzed while forming the mesh structure of the numerical model for the mesh independence study. By mesh independence study it is aimed to avoid calculation errors and costs. Therefore, the mesh independence study was carried out with the analysis using the data obtained from PIV experiments for the velocity boundary condition and the MIT experiment for the temperature boundary condition. The room walls are considered as 300.15 K, which is the recommended room interior surface temperature for the cooling tests according to the ISO 5151 standard (Non-Ducted Air Conditioners and Heat Pumps-Testing and Rating for Performance: ISO 5151, 2017). Six analyses that used these boundary conditions were performed with element numbers: $2.8x10^5$, $6.3x10^5$, $7.9x10^5$, $1.1x10^6$, $1.5x10^6$ and $2.2x10^6$. The mesh independence study was performed using the LES model utilized for reliability (Posner et al., 2003; Serra, 2023).

Since the volume of the room is relatively larger than the SAC outflow, using total investigation volume is not appropriate because it includes near-zero velocities at the corners that will distort the average value. The midplane of the SAC was selected to evaluate mesh independence to avoid this situation by reducing these low-velocity areas. Furthermore, the point with the highest velocity in the core of the jet is also taken into consideration to ensure the result. The position of the point (black dot in Figure 3.6) where the comparison data were obtained and the position of the midplane were shown in Figure 3.6.

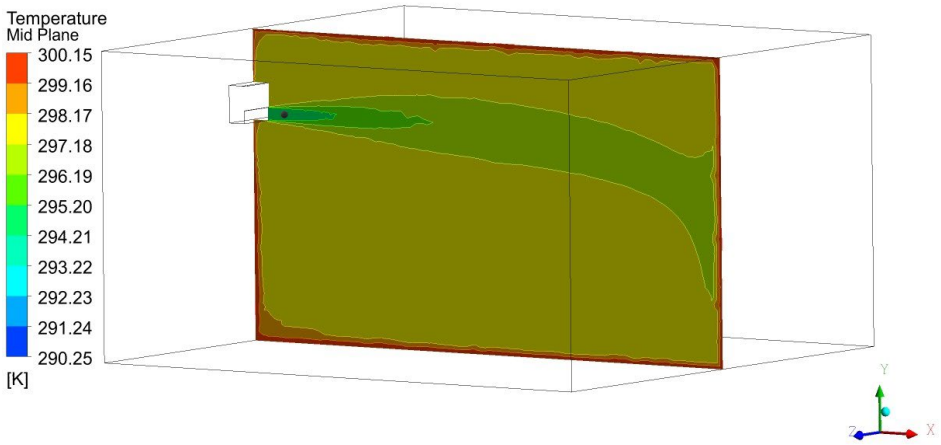


Figure 3.6. The position of the obtained data point and plane (Yücekaya et al., 2023)

Upon evaluating both velocity and temperature values at the point and the plane, no significant variations were observed in the results of the analysis above from the number of elements "1.1x10^6". However, there was a notable increase in the cost of the analysis with the number of elements "1.5x10^6", at 39.58%, and "2.2x10^6", at 104.16%. As such, it was determined that the optimal element number for the mesh structure in this study should be "1.1x10^6", and the minimum element size is 1.75 mm at the outlet section of the SAC."

Using the results of SPIV and MIT experiments as boundary conditions is effective in time-dependent investigations. In order to address this situation in more detail, time-dependent analyses were carried out using the Large Eddy Simulation (LES). The results of the analyses conducted using the LES demonstrated agreement with experimental data (Blocken, 2018; De Cachinho Cordeiro et al., 2023; Liu et al., 2020; X. Zhang et al., 2020). As such, the subgrid-scale within the ANSYS-CFX program was utilized in this study.

The numerical models were analyzed to evaluate their independence from time and time step. The initial investigation utilized a total time of 2400 seconds to assess time independence. As a result of this analysis, the area average temperature data were obtained from a plane in the middle of the room. By subtracting the temperature at each time step from the previous time step, it was determined that after 400 seconds, the temperature in the central plane exhibited a deviation of less than +-0.05 K with

respect to time. Given the negligible nature of this variation, the total time for the analysis was subsequently set to 600 seconds. An analysis was conducted using time steps of 15, 30, 45, and 60 seconds, and it was observed that there was a minimal difference between them. Despite this, the 15-second time step was selected for further examination of the flow and temperature characteristics of the room due to the lack of a significant difference in terms of analysis time.

3.3 Validation of Numerical Studies by Data Assimilation with Stereo Particle Image Velocimetry

In the analyses performed for validation, SPIV data were used as the boundary condition, as well as the boundary condition was defined by averaging the data obtained from these experiments for second analysis. The average velocity profile obtained as a result of SPIV is 1.91 m/s. Thus, for validation, 2 separate analyses were carried out by defining to the SAC indoor unit outlet section SPIV data as 3-dimensional and 1.91 m/s as homogeneous velocity condition.

The results of the analysis have been validated through comparison with SPIV data. The validation line in Figure 3.7 was selected at a distance twice the height of the SAC outlet section and in the jet flow. In addition, this selection is a region in the view of the camera in the SPIV experiments where the validation was performed.

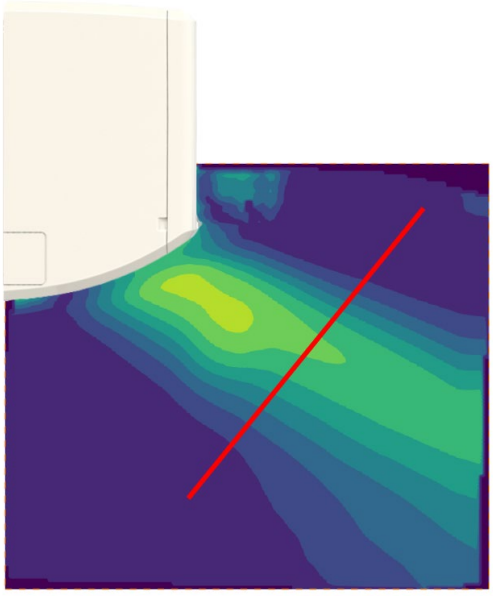


Figure 3.7 Validation line (red) position (Yücekaya et al., 2023)

The velocity profiles obtained from the line were compared with the velocity data at the same position in the CFD results with investigated boundary condition alternatives. The results are presented in Figure 3.8.

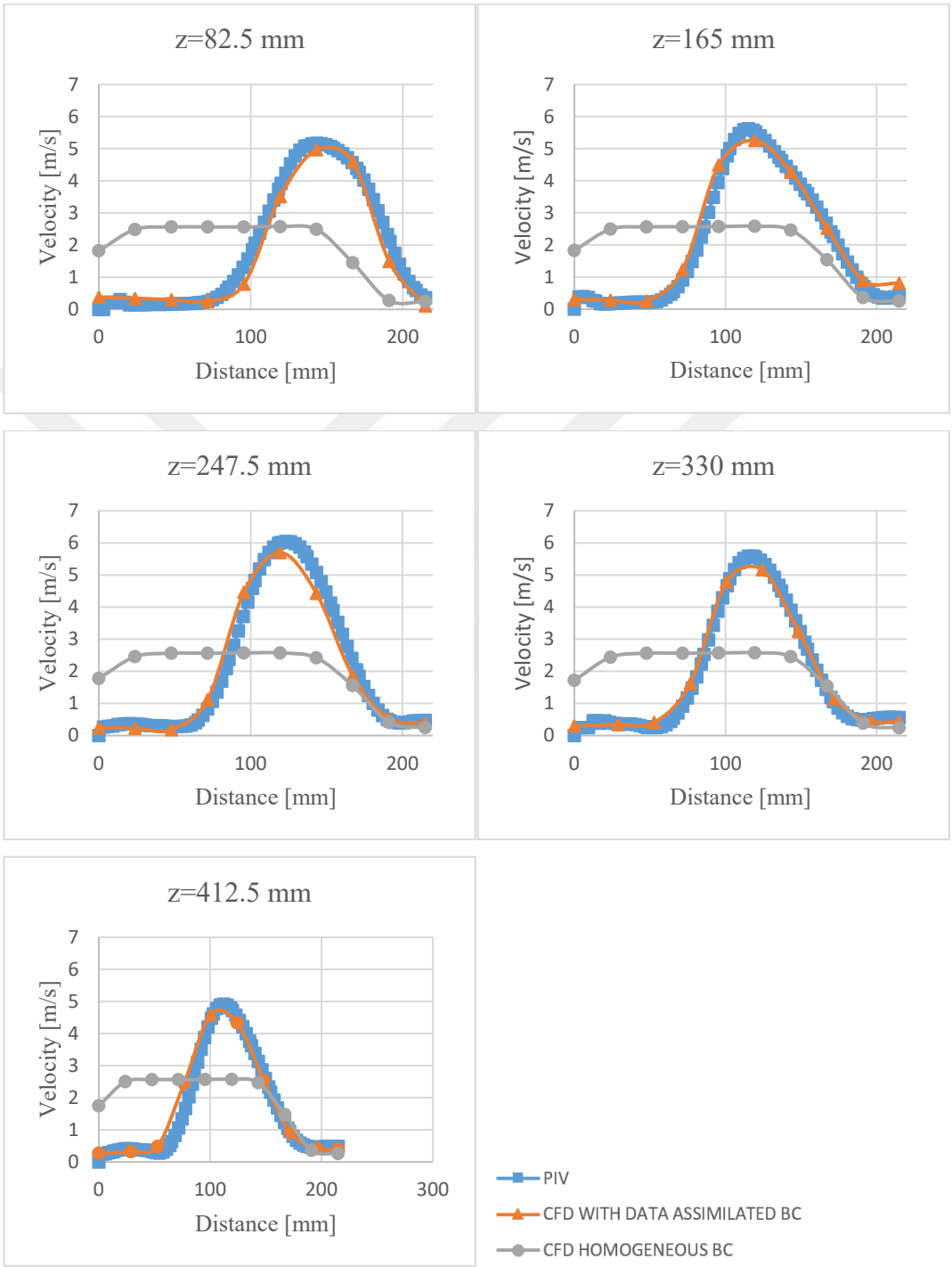


Figure 3.8 Velocity profile comparison between SPIV data and CFD data with different boundary conditions (Continued)

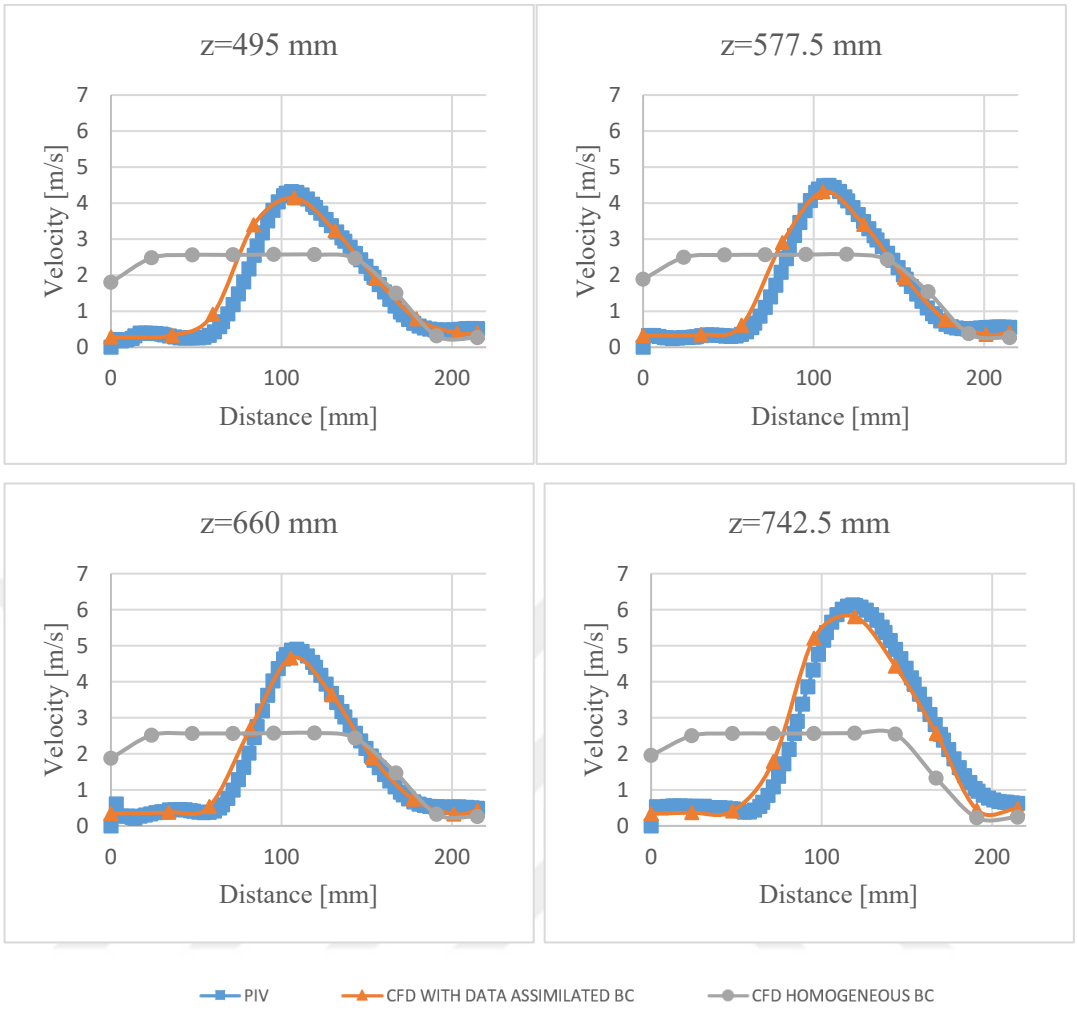


Figure 3.8 Velocity profile comparison between SPIV data and CFD data with different boundary conditions (Yücekaya et al., 2023)

The CFD results with investigated boundary condition alternatives compared with the SPIV experiment in Figure 3.8. It can be clearly seen that the CFD with data assimilated boundary condition is significantly more coherent to the experimental measurement than the conventional CFD with homogeneous boundary condition. Additionally, the boundary condition generated with data assimilation models the jet profile more accurately. This accuracy difference is evaluated quantitatively by the average velocities of the profiles in Table 3.1. The maximum difference between CFD with data assimilated boundary condition and SPIV experiments results is 4.74%, while the maximum difference between CFD with homogeneous boundary condition and SPIV experiments results is 24.03%.

The CFD analyses with different boundary condition definitions have the same average velocities at 82.5 mm. However, when examining Figure 3.8 at z=82.5 mm, it can be seen that despite the same average velocities, there are significant differences in the flow structure. This indicates that defining homogeneous boundary conditions in CFD analyses increases the error not only in terms of values but also in terms of flow characteristics.

Table 3.1. Average velocity comparison between SPIV and CFD at line

Plane Position (z)[mm]	SPIV Experiments Average Velocity at Comparison line [m/s]	CFD with Data Assimilated BC Average Velocity [m/s]	CFD with Homogeneous BC Average Velocity [m/s]	%Differences Between SPIV and CFD with Data Assimilated BC Results	%Differences Between SPIV and CFD with Homogeneous BC Results
82.5	1.98	1.91	1.91	-3.54%	-3.54%
165	2.07	2.03	1.91	-1.93%	-7.73%
247.5	2.15	2.07	1.91	-3.72%	-11.16%
330	1.9	1.81	1.91	-4.74%	0.53%
412.5	1.71	1.67	1.91	-2.34%	11.70%
495	1.54	1.58	1.91	2.60%	24.03%
577.5	1.56	1.54	1.91	-1.28%	22.44%
660	1.63	1.56	1.91	-4.29%	17.18%
742.5	2.4	2.31	1.91	-3.75%	-20.42%

3.4 Results

An investigation was conducted to assess the impact of various boundary condition (BC) specifications on the numerical analysis of the flow within the volume. The analysis was performed using four different combinations of velocity and temperature boundary conditions.

In the first of the analyses, the mean velocity and temperature values obtained from the SPIV and MIT experiments were defined as homogeneous velocity and homogeneous temperature boundary conditions (Fig. 3.9-a). In the second analysis, the velocity values obtained from the SPIV experiment were defined as the velocity boundary condition for the air conditioner outlet section. In this analysis, the mean value of the experimental data obtained from the MIT experiment was used as the homogeneous temperature value in the air conditioner outlet section (Fig. 3.9-b). In

the third analysis, the temperature values obtained from the MIT experiment were defined as the temperature boundary condition for the air conditioner outlet section. In this analysis, the mean of the velocity values obtained from the SPIV experiment was used as the homogeneous velocity boundary condition (Fig. 3.9-c). In the fourth analysis, the values obtained from the MIT and SPIV experiments were defined as the velocity and temperature boundary conditions for the outlet section of SAC (Fig. 3.9-d). The homogeneous velocity obtained by averaging the SPIV data is 1.91 m/s (Fig. 3.9-a and 3.9-c). The homogeneous temperature obtained by averaging the MIT test data is 294.39 K (Fig. 3.9-a and 3.9-b).

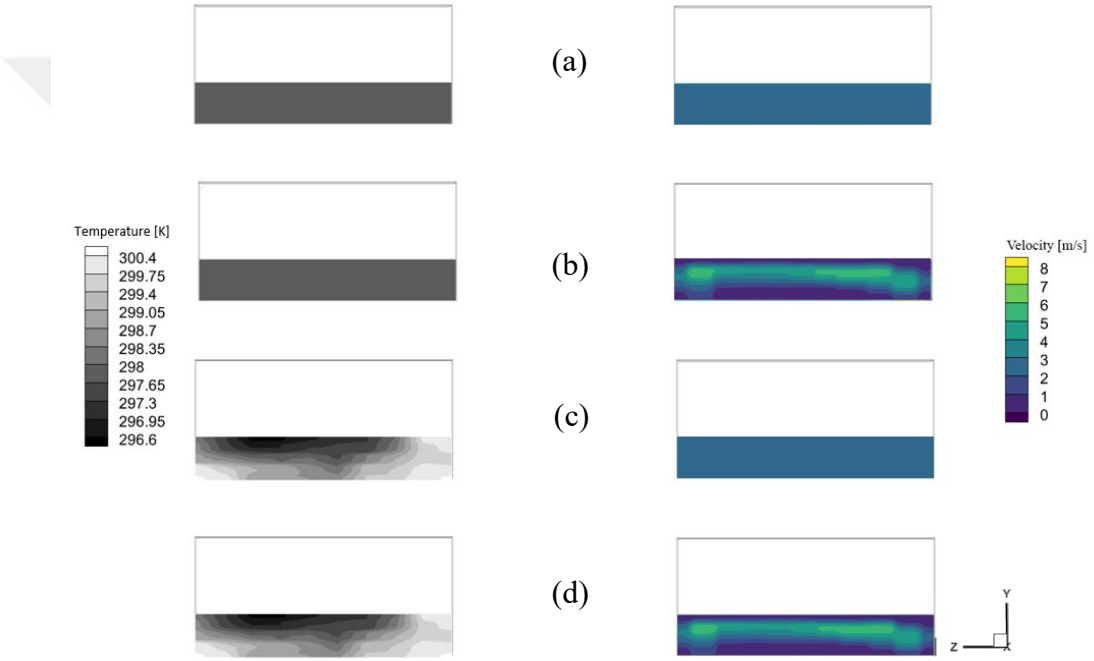


Figure 3.9 Boundary conditions of outflow section: a) Temperature BC: Homogeneous, Velocity BC: Homogeneous, b) Temperature BC: Homogeneous, Velocity BC: PIV, c) Temperature BC: MIT, Velocity BC: Homogeneous, d) Temperature BC: MIT, Velocity BC: PIV (Yücekaya et al., 2023)

The velocity profile (Fig. 3.9-a and 3.9-c) when a homogeneous velocity is defined to the indoor unit's outlet significantly differs from the velocity profile obtained from the experiments, and defining a homogeneous value to the outlet part is an assumption with a high error rate. On the other hand, using the data extracted from the SPIV experiments as the boundary condition enables more accurate three-dimensional representations of the jet profile in the analysis. Thus, higher vectorial accuracy can be obtained in the velocity definitions in the analysis.

In the experimental study section, it is seen that the outlet velocity distribution of the SAC indoor unit has a double-peaked velocity profile due to the blowing characteristic of the crossflow fan (Figure 3.4). This shows that the definition of a homogeneous velocity value as a boundary condition is not valid everywhere at the outlet. This affects many parameters, such as the penetration of the jet into the stagnant air in the room, the temperature distribution, and the flow pattern. As can be seen in Figure 3.10, the penetration of the jet into the stagnant air, which is a critical parameter in indoor air studies, differs depending on the definition of the velocity boundary conditions.

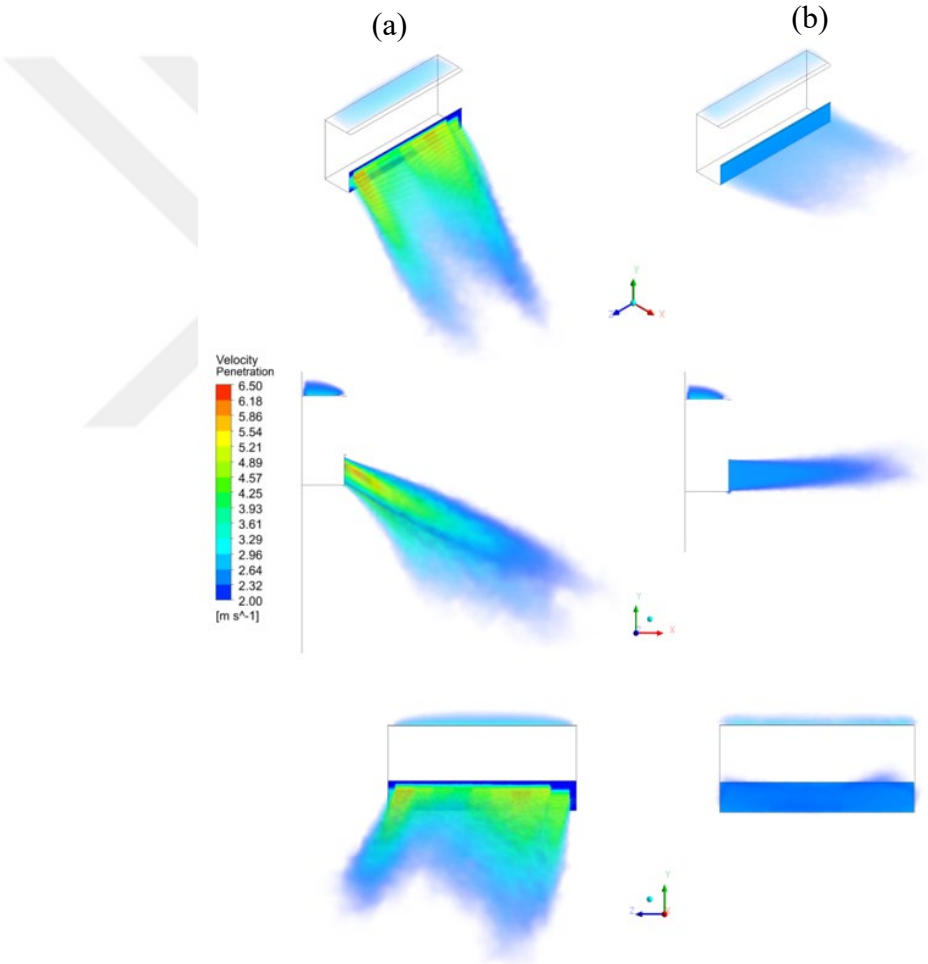


Figure 3.10 Penetration of outflow section of air conditioner indoor unit, a) Temperature BC: MIT, Velocity BC: PIV, b) Temperature BC: MIT, Velocity BC: Homogeneous (Yücekaya et al., 2023)

In Figure 3.10-a, when the flow profile obtained by defining the SPIV test results as the boundary condition for the analysis is examined, it is seen that the jet penetrates the stagnant air at different depths along its section and is affected by the flow

structures in the third dimension. On the other hand, in the velocity distribution defined as homogeneous in Fig. 3.10-b, unlike the real situation, it has been determined that the jet penetrates the stagnant air at the same depths throughout the section. This situation caused the jet flow in the Figure 3.10-b analysis to lose its effect at a shorter distance than the jet flow in Figure 3.10-a analysis. For the numerical comparison of the stagnant air penetration, the positions where the jet velocity drops to 2 m/s are taken as reference. In the comparison, the ratio of the maximum penetration depth in analysis a, where velocity data obtained from SPIV experiments is defined as the boundary condition, to the maximum penetration depth in analysis b, where the velocity boundary condition is defined as homogeneous, is 61%. The ratio of the average penetration depth in analysis a to average penetration depth in analysis b is 93%. It has been revealed that there is a significant difference between these two boundary condition definitions.

Velocity and temperature distributions at the XY midplane of the room were obtained by choosing a time (180th second) when the room started to cool (Figure 3.11). Fig. 3.11-a and 3.11-b show the analyses with the data assimilated boundary conditions, and Fig. 3.11-c and 3.11-d show the analysis in which the boundary conditions are defined as homogeneous.

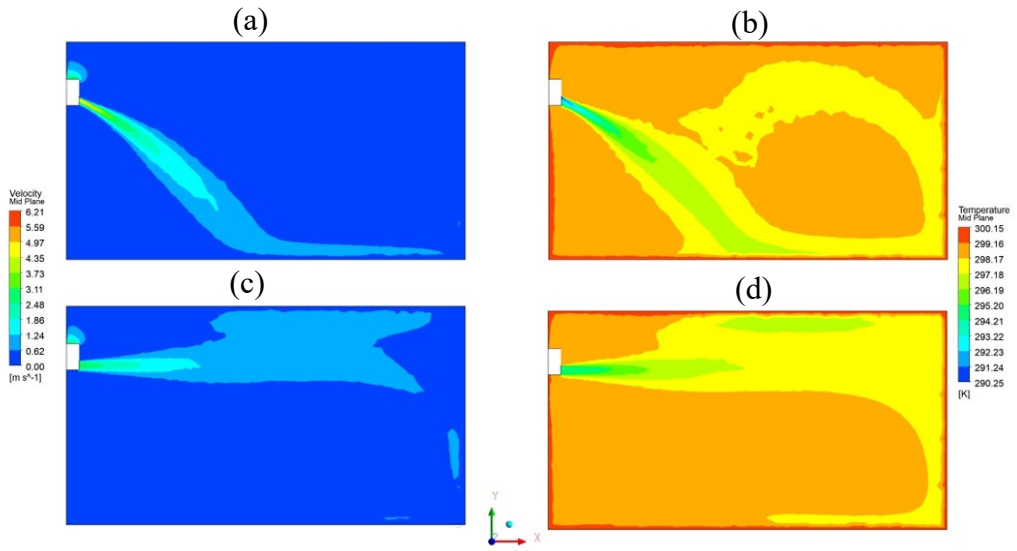
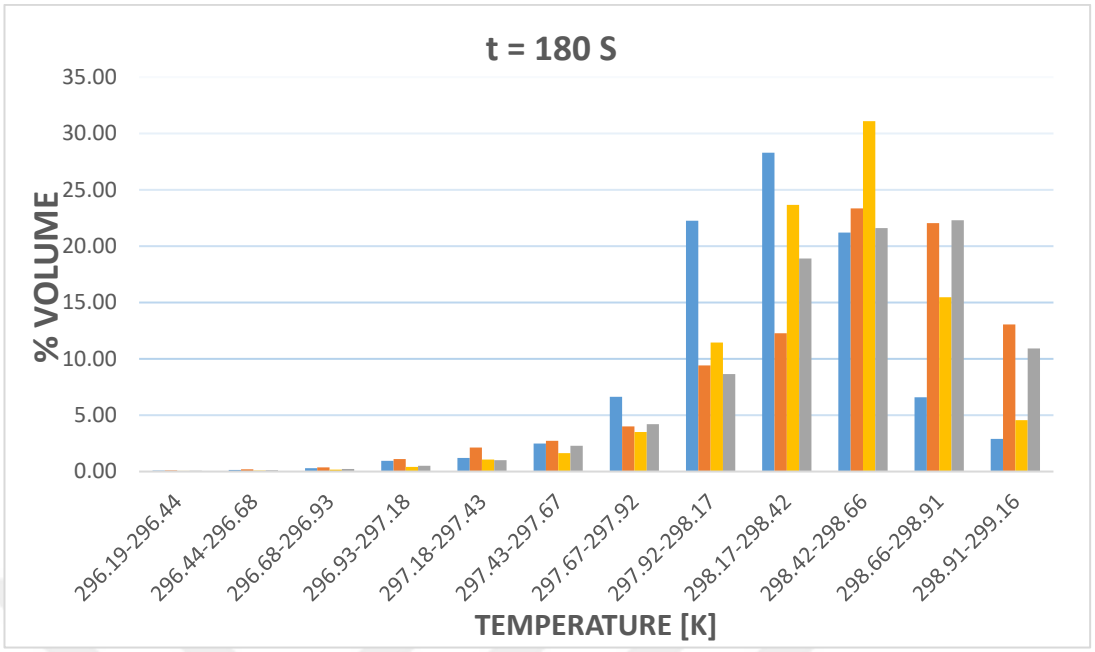
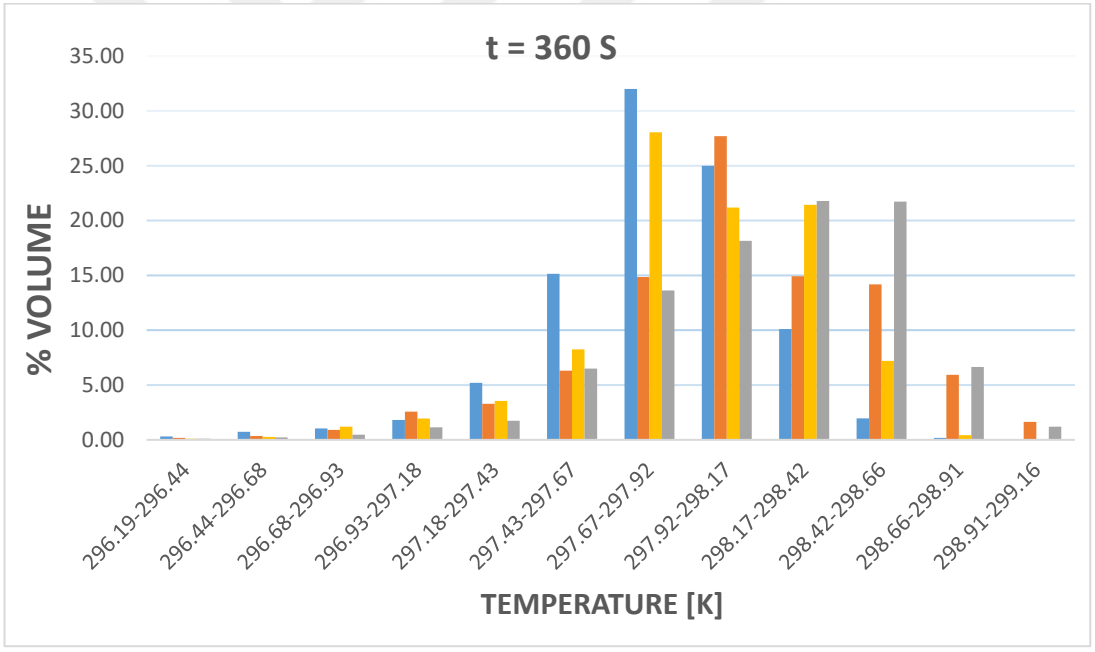


Figure 3.11 Temperature and velocity distributions of the XY midplane of the room at 180 seconds: a) Velocity BC: SPIV, b) Temperature BC: MIT, c) Velocity BC: Homogeneous, d) Temperature BC: Homogeneous (Yücekaya et al., 2023)

It is observed that the definition of different boundary conditions has a discernible impact on the velocity distribution and temperature distribution at a given time. In addition to influencing the flow structure of the room when it reaches a steady state, the flow dynamics of the room from the moment the air conditioner is initiated until it begins to stabilize are also influenced by the boundary conditions. The velocity boundary condition has a significant effect on the temperature distribution, as well as the velocity distribution within the room, depending on the time. The histograms of the temperature distribution at 180 s, 360 s, and 600 s in Fig. 3.12 illustrate the influence of the velocity boundary condition on heat transfer through convection in the entire room volume as a percentage.


t = 180 S
35.00
30.00
25.00
20.00
15.00
10.00
5.00
0.00
% VOLUME
296.19-296.44
296.44-296.68
296.68-296.93
296.93-297.18
297.18-297.43
297.43-297.67
297.67-297.92
297.92-298.17
298.17-298.42
298.42-298.66
298.66-298.91
298.91-299.16
TEMPERATURE [K]


t = 360 S
35.00
30.00
25.00
20.00
15.00
10.00
5.00
0.00
% VOLUME
296.19-296.44
296.44-296.68
296.68-296.93
296.93-297.18
297.18-297.43
297.43-297.67
297.67-297.92
297.92-298.17
298.17-298.42
298.42-298.66
298.66-298.91
298.91-299.16
TEMPERATURE [K]

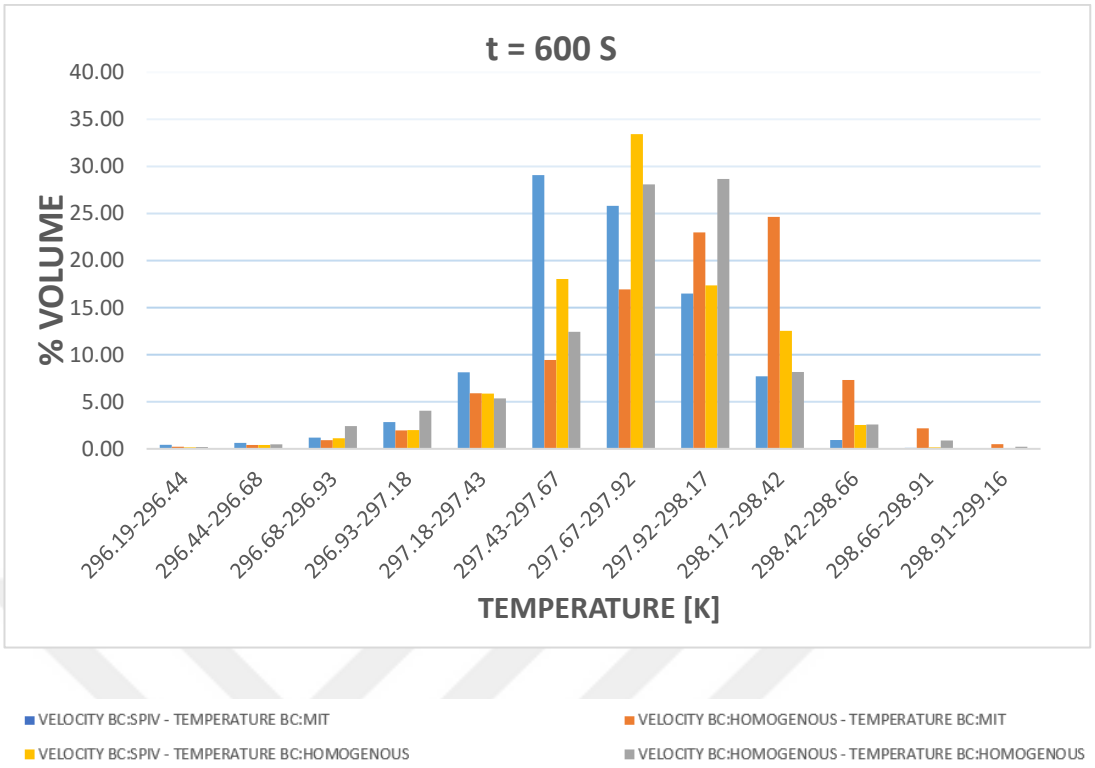


Figure 3.12 Temperature histograms at 180 s, 360 s, 600 s (Yücekaya et al., 2023)

The temperature histograms in Fig. 3.12 were created in the analyses with four different boundary condition definitions. In the histograms, it is seen that they have different characteristics at the same time step, and they also show different cooling characteristics over time. This demonstrates that the implementation of a homogeneous boundary condition in the analysis has an impact on the temperature distribution within the room, both in terms of planar and volumetric distribution. It is evident that this effect influences both the steady-state temperature distribution and the heating or cooling characteristics.

The importance of utilizing three-dimensional and three-component experimental data as velocity boundary conditions is highlighted when Fig. 3.11 and 3.12 are considered together. However, velocity data alone is insufficient for accurate prediction of the temperature distributions in the room with numerical study. It is also essential to experimentally obtain the temperature distribution of the air conditioning device's outlet and incorporate these values into the numerical model. Fig. 3.13-a, b and c show the temperatures of the room in the XY midplane at 180, 360 and 600 seconds, respectively, of the analysis where the data obtained by the MIT method is

defined as the boundary condition. Fig. 3.13-d, e and f show the temperatures of the room in the XY midplane at 180, 360 and 600 seconds, respectively, of the analysis with homogeneous temperature boundary condition definition.

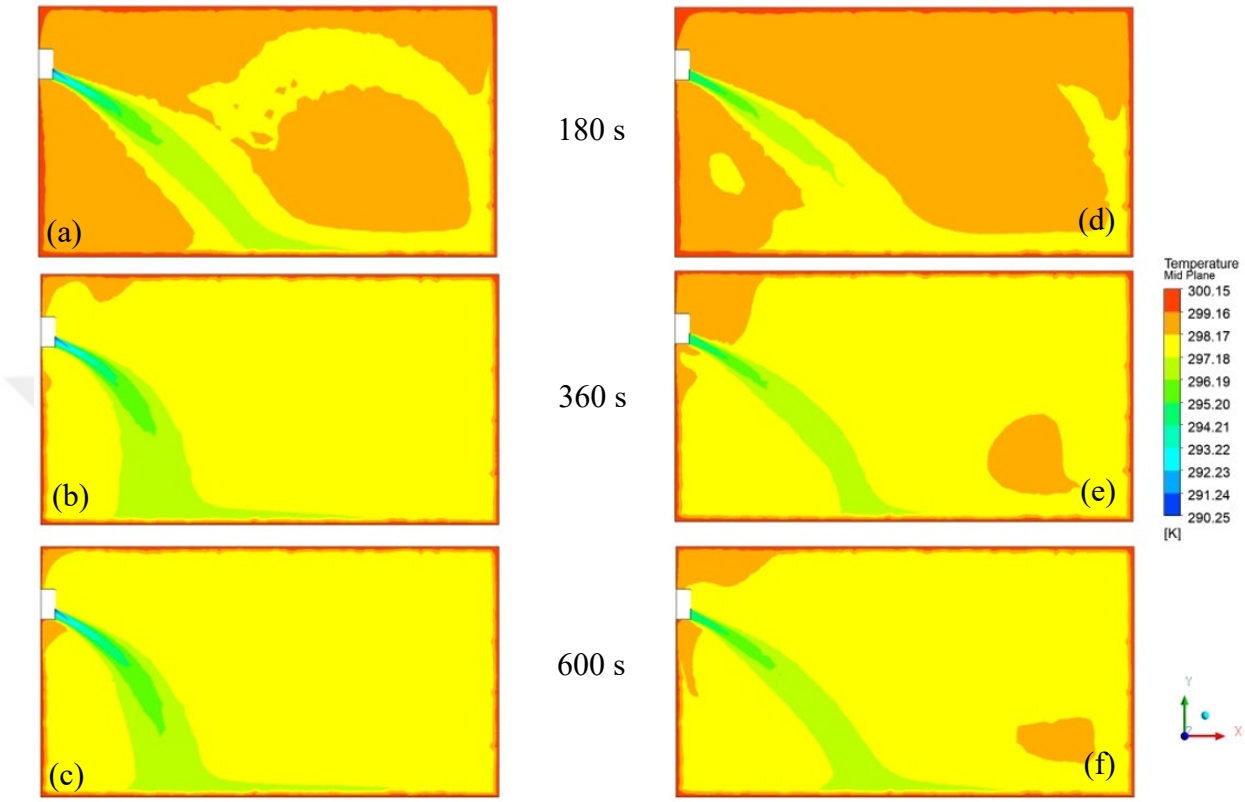


Figure 3.13 Temperature distributions of the XY midplane of the room at different times: a, b, c) Temperature BC: MIT, Velocity BC: SPIV, d, e, f) Temperature BC: Homogeneous, Velocity BC: SPIV (Yücekaya et al., 2023)

It is seen that defining a homogeneous temperature boundary condition for the SAC indoor unit outlet section with different temperatures at each point affects the temperature distribution in the room. In addition, when the temperature distributions in the two analyses at the same time step (Fig. 3.13 a-d, b-e, c-f) are evaluated, it is seen that the definition of the temperature boundary condition affects the cooling characteristic of the room as well as the distribution inside the room.

When all the results are evaluated, although the total flow rate and the average temperature of the outlet flow of the device are equal in all CFD analyses, the temperature distribution, the jet flow's velocity profile, and the penetration into the stagnant air have significant differences depending on boundary conditions. The CFD

with data assimilated boundary conditions presented significantly better accuracy than the CFD with conventional homogeneous boundary conditions.

CHAPTER FOUR
EXPERIMENTAL AND NUMERICAL INVESTIGATION OF FAN-BURNER SYSTEM OF THE COMBI BOILER

Wall-hang gas-fired heating appliances are now widely used for both space heating and hot water needs in regions where fuel is available. During the operation of the device, the fuel and air sucked in with the help of the fan are mixed and transmitted into the burner (Figure 4.1). The combustion characteristics are influenced by the uniform distribution of the air-fuel mixture from the burner to the outlet holes. This situation directly affects the formation of a homogeneous heat transfer in the combustion zone and emission characteristics. Since these effects cause changes in the heating performance and emission rates of the device, they are essential for both environmental impacts and design criteria.

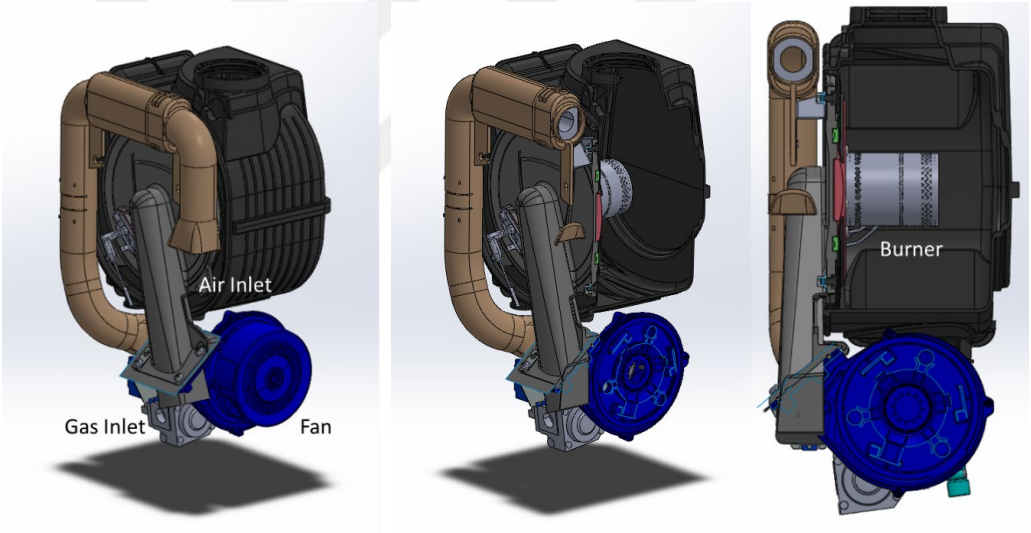


Figure 4.1 CAD of combi boiler fan-burner system

As mentioned in Section 1.1.3, the homogenous burner outlet assumption is widely used in the design phase of combi boilers. This assumption includes that the air-fuel mixture proceeds homogeneously in the duct from the fan outlet, is evenly distributed in the burner, and exits at the same flow rate and structure in the holes. In combi boilers using centrifugal fans, the fan does not have a homogeneous flow profile at the outlet due to its structure. Since the upper part of the fan is usually tangent to the fan blades, higher velocity is observed in the upper parts, while the velocity may be slower in the

lower parts of the outlet section of the fan. For this reason, the homogeneous assumption of the flow structure of the fan-burner system affects the burner design, the combustion volume and heat exchanger designs.

The fan-burner outlet of a 24 kW combi boiler, which is the currently produced and most demanded capacity, is analysed by SPIV method and the burner inlet is examined and the effect of spatial resolution on the three dimensional data in the use of SPIV method is presented in Section 4.1 in detail.

A cover design is at the burner inlet to increase the homogeneity of the flow. The CAD design of this region is given in Figure 4.1.2. Since this region is an obstacle in front of the fan, it can create a pressure difference and directly affect the fan's flow rate. The SPIV experiments carried out by adding this region to the fan outlet are presented in Section 4.1.2 in detail.

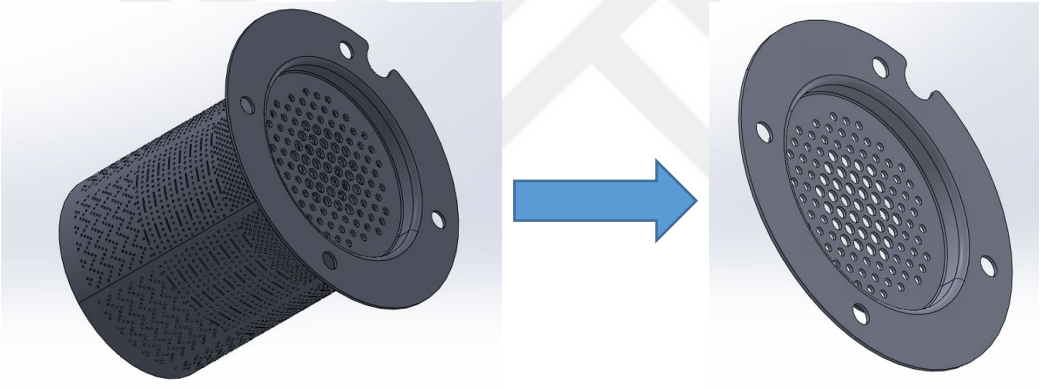


Figure 4.2 CAD of cover at the burner inlet

CFD analyses of the burner were performed by applying the data obtained in Sections 4.1, 4.1.1 and 4.1.2 to the numerical model using the data assimilation method. Detailed information is presented in Section 4.2.

4.1 Flow Structure of Fan-Burner System in Combi Boiler

In combi boiler systems, fuel is transferred to the fan with the help of the gas valve. Fresh air is sucked through a duct shown in Figure 4.3 and reaches the fan to be mixed with the fuel.

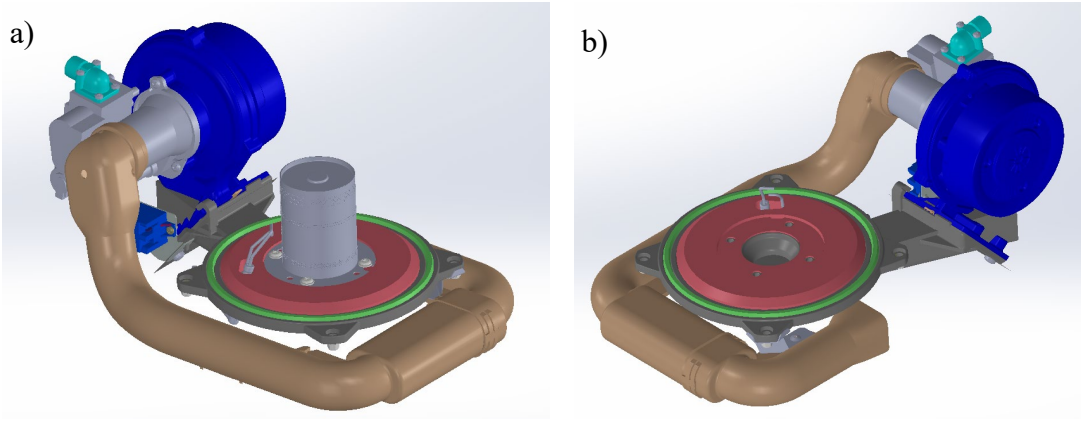


Figure 4.3 CAD drawing of the fan outlet area of the 24 kW capacity combi boiler device a) Fan system without burner b) Fan system with burner

The inlet of the fluid driven by the fan to the burner, which is shown in detail in Figure 4.3-b, is critical for the flow structure in the burner. The homogeneity of the flow in this region can help the homogeneous distribution inside the burner. For this reason, this region was investigated by SPIV method. The air visualisation of the fan-burner system placed in the schematic of SPIV experimental setup is presented in Figure 4.4.

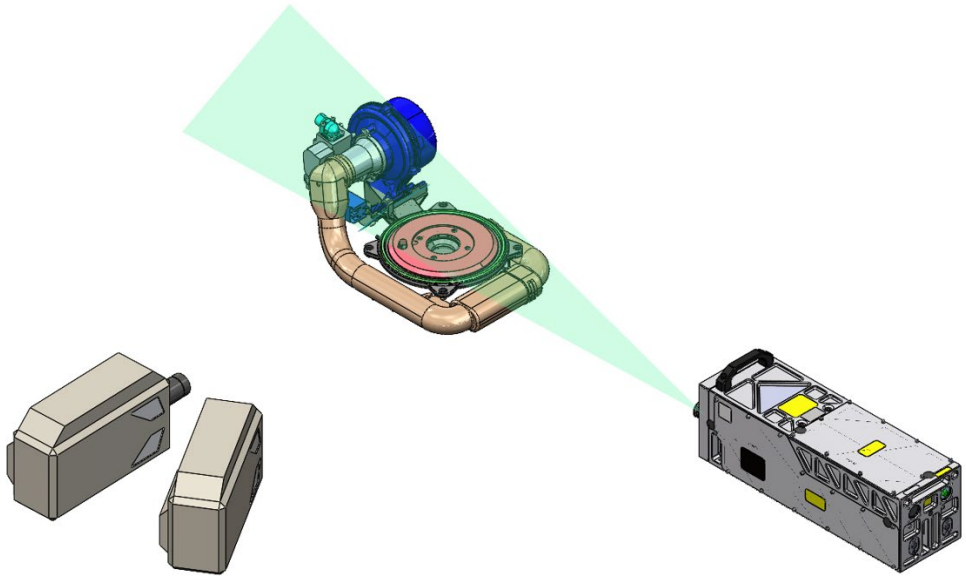


Figure 4.4 The Schematic of SPIV experiment setup

The investigation volume for the fan system on the SPIV plane was determined at the burner inlet. Figure 4.4 shows the location. The region depicted in Figure 4.5 has a total width of 105.5 mm, with the fan transferring the air-fuel mixture to the burner in a 60 mm section. An examination distance of 80 mm was determined to enable SPIV experiments to examine the behaviour of the air after this section.

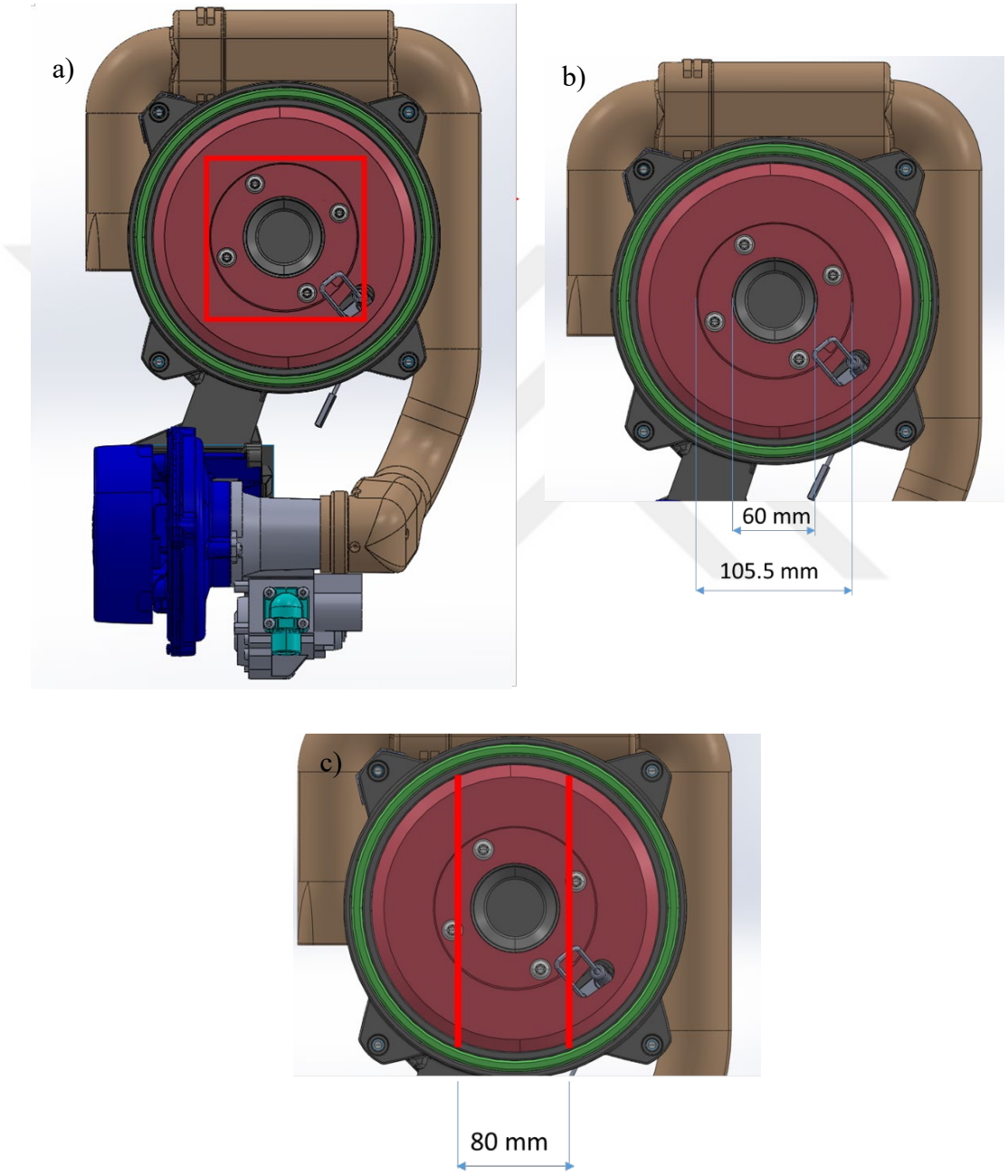


Figure 4.5 Combi boiler fan-burner system investigation region a) fan-burner system of the combi boiler, b) dimensions of the burner inlet, c) SPIV investigation area

To obtain volumetric data in SPIV experiments, the region of interest must be scanned at regular intervals. The resolution of the data improves with higher frequency of these interval values. In the study, an 80 mm area was examined in 5 separate planes of 20 mm each. The SPIV examination planes are showed in Figure 4.6.

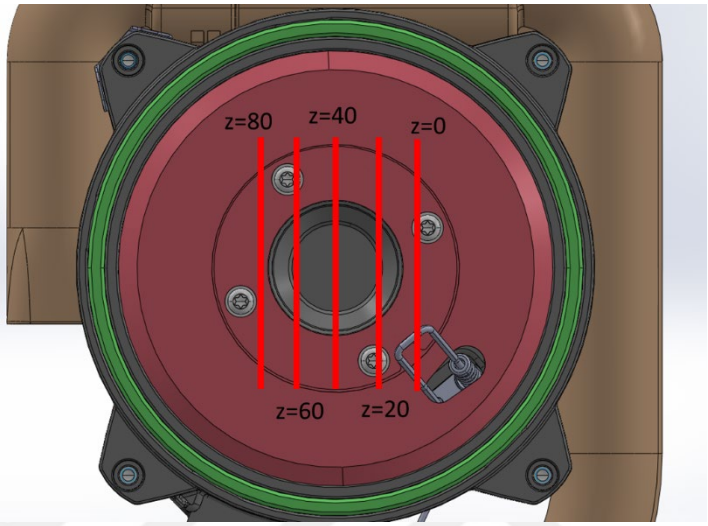


Figure 4.6 Investigation planes of SPIV experiment

The SPIV experiment utilized two cameras to meticulously obtain 2-dimensional 3-component velocity data from varying angles. One camera, positioned perpendicular to the plane of investigation, provided a comprehensive view, while the other, angled, contributed data on the third component of the velocity.

The image obtained for the z=40 mm plane, a mid-plane among the examination planes shown in Figure 4.6, is presented in Figure 4.7.

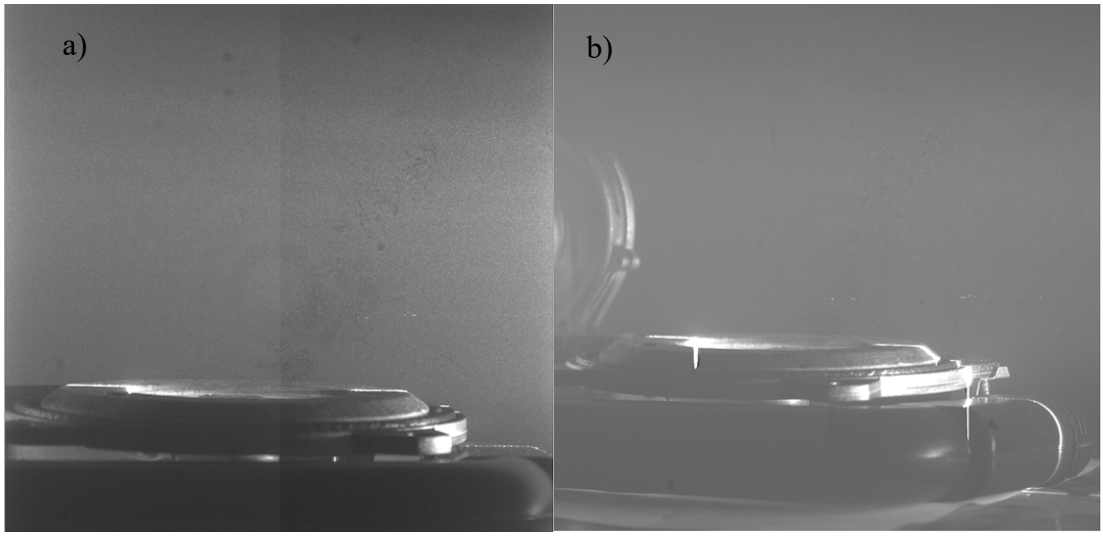
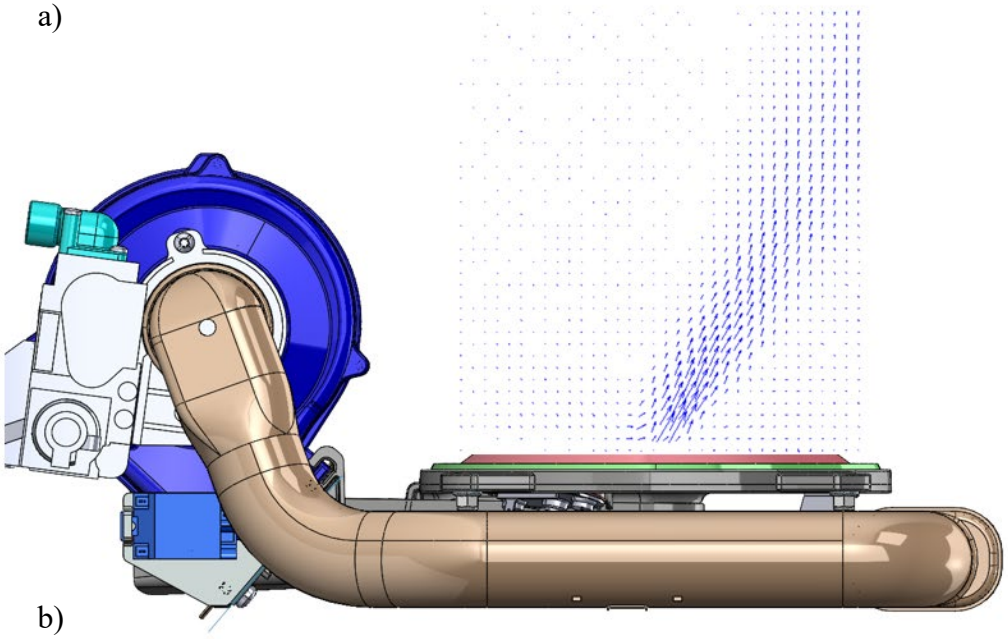


Figure 4.7 z=40 mm SPIV experiment results a) direct camera b) angular camera

Data collection process was thorough, with 150 image pairs captured from each camera. This approach resulted in a total of 600 images for a single z value. Subsequently, cross-correlation was performed, as detailed in Chapter 2.1, leading to the acquisition of velocity maps. An example of these maps is presented in Figure 4.8 for z=40.

a)



b)

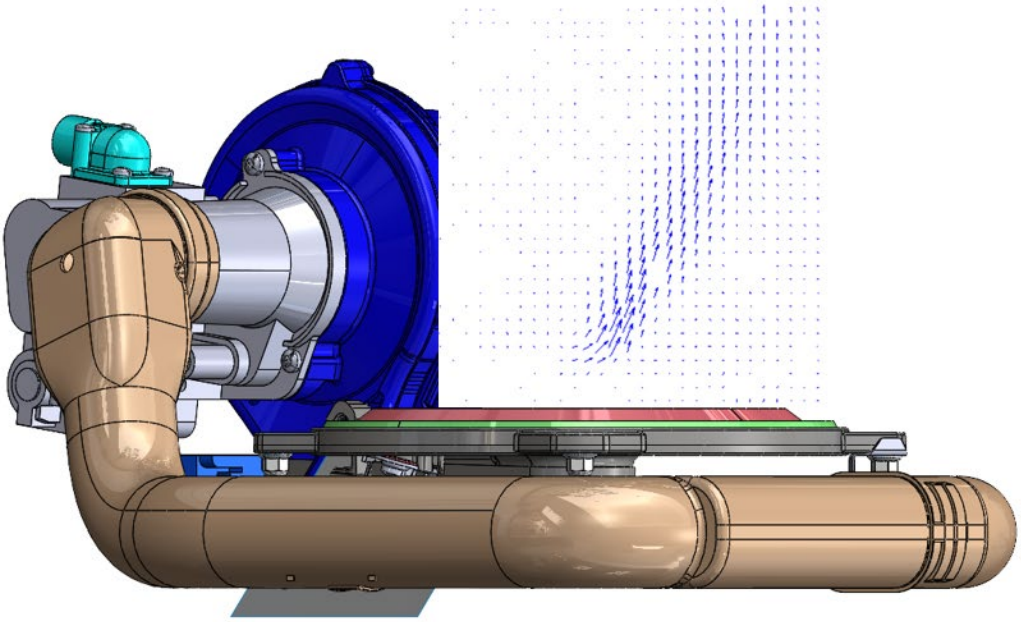


Figure 4.8 z=40 mm SPIV experiment velocity distribution results a) direct camera b) angular camera

The velocity profiles in Figure 4.8 show that the flow is separated at an angle from the front of the outlet area. In other parts of the outlet area, the velocity values are very low. The velocity data obtained from two cameras were combined to obtain a stereo result. With the stereo result obtained, the data of 3 components of the velocity could be displayed on a single map. In addition, a line was determined directly above the

outlet region to graphically obtain the 2-dimensional 3-component velocity data obtained as a result of the experiments. The stereo velocity map for Z=40 and the line of investigation are presented in Figure 4.9.

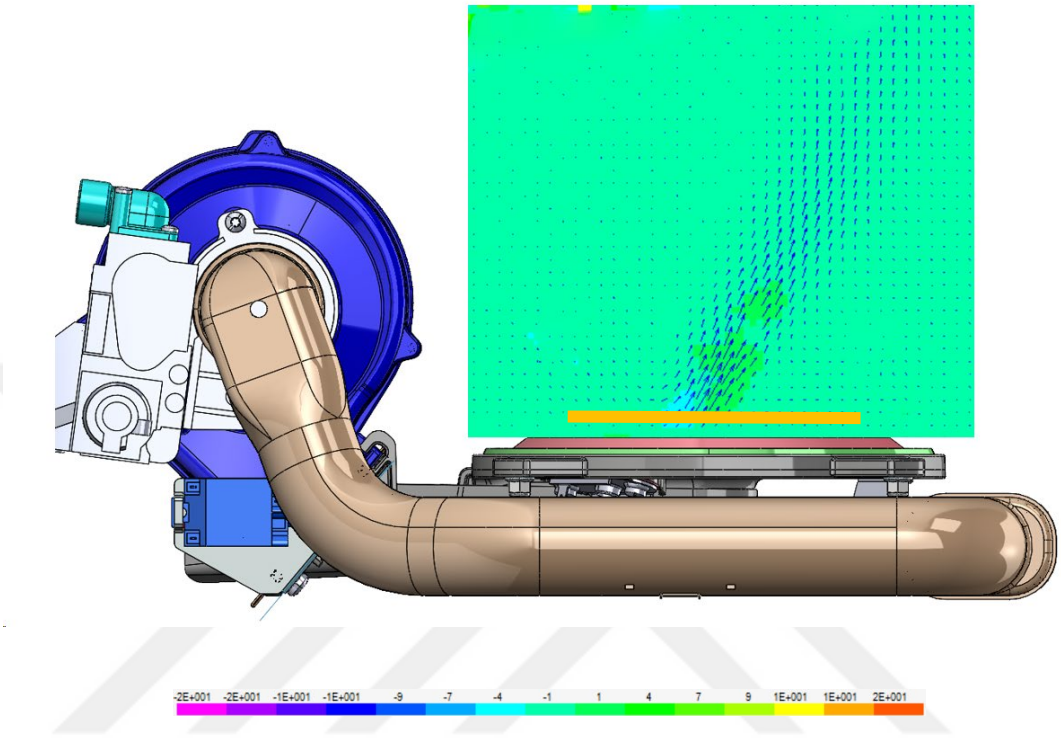
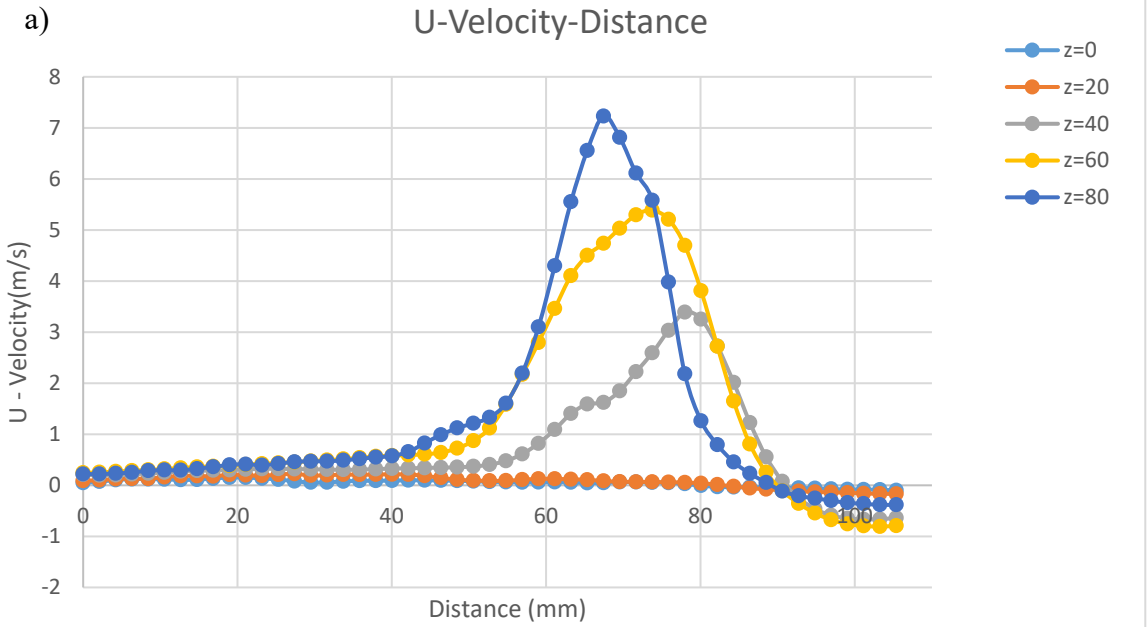


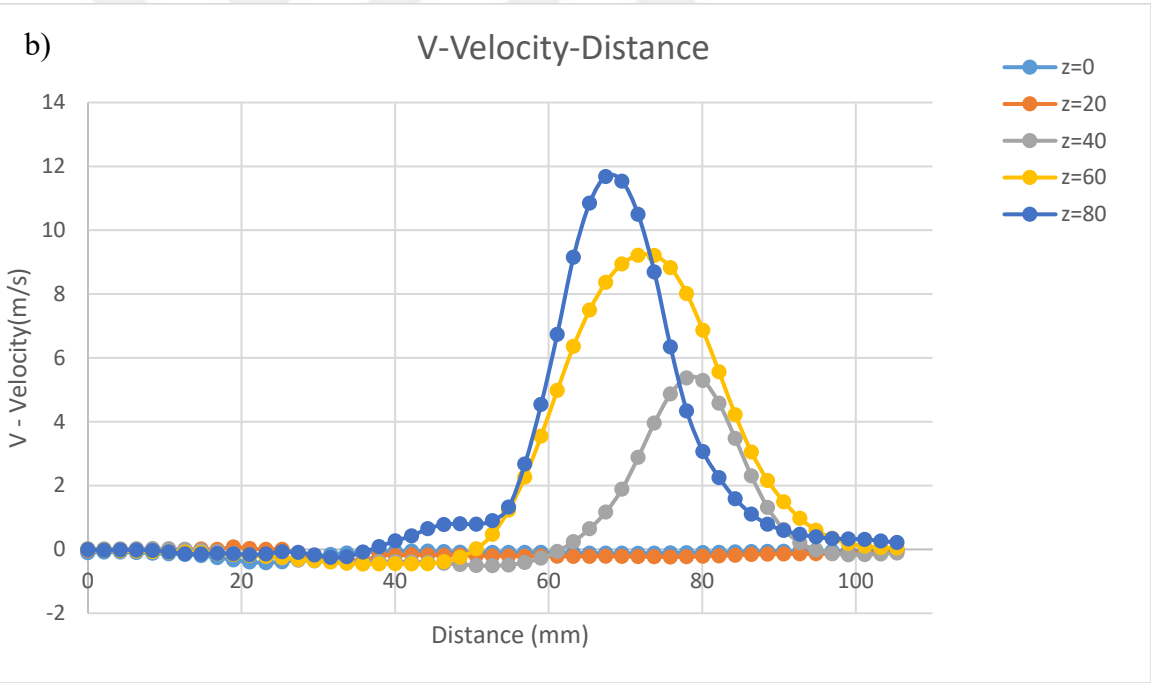
Figure 4.9 z=40 mm SPIV 3 component velocity map

The u, v and w components of the velocity and the resultant velocity data were obtained for a total of 5 investigation planes from the line indicated in green in Figure 4.9. The obtained data are presented in the graphs in Figure 4.10.

a)


U-Velocity-Distance
U - Velocity(m/s)
Distance (mm)
z=0
z=20
z=40
z=60
z=80

b)


V-Velocity-Distance
V - Velocity(m/s)
Distance (mm)
z=0
z=20
z=40
z=60
z=80

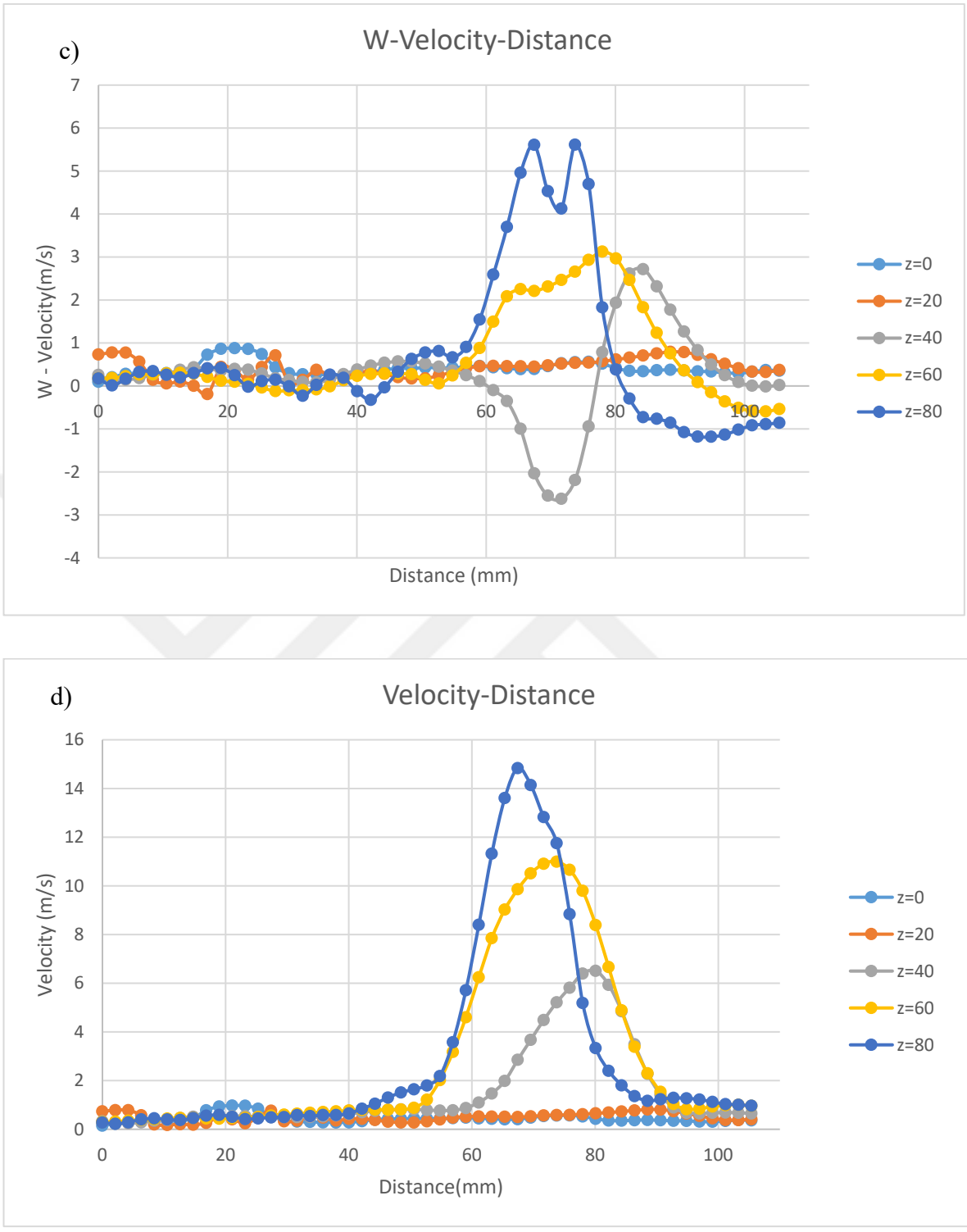


Figure 4.10 SPIV results at line a) u-velocity b) v-velocity b) w-velocity d) resultant velocity

Figure 4.10-c shows the non-homogeneous nature of the flow in the outlet region with a diameter of 105 mm. Here, the flow exhibits a significant velocity between 50 mm and 90 mm, while the velocity drops below 1 m/s in other regions. This

observation underscores that the flow, originating from the fan and channelled to the burner, is not uniform at the burner inlet. Instead, it enters the burner with a distinct orientation, a key finding of our study.

For a comprehensive understanding of the flow structure, a total of 3000 images from 5 different planes were processed, and the velocity maps obtained were converted into a volumetric velocity map with the TECPLOT program. The regions between the investigation planes were carefully interpolated by the Kriging method (De Baar et al., 2014). The 5 m/s, 8 m/s and 10 m/s iso-surfaces of the three-dimensional and three-component velocity map obtained as a result of this thorough process are presented in Figure 4.11.

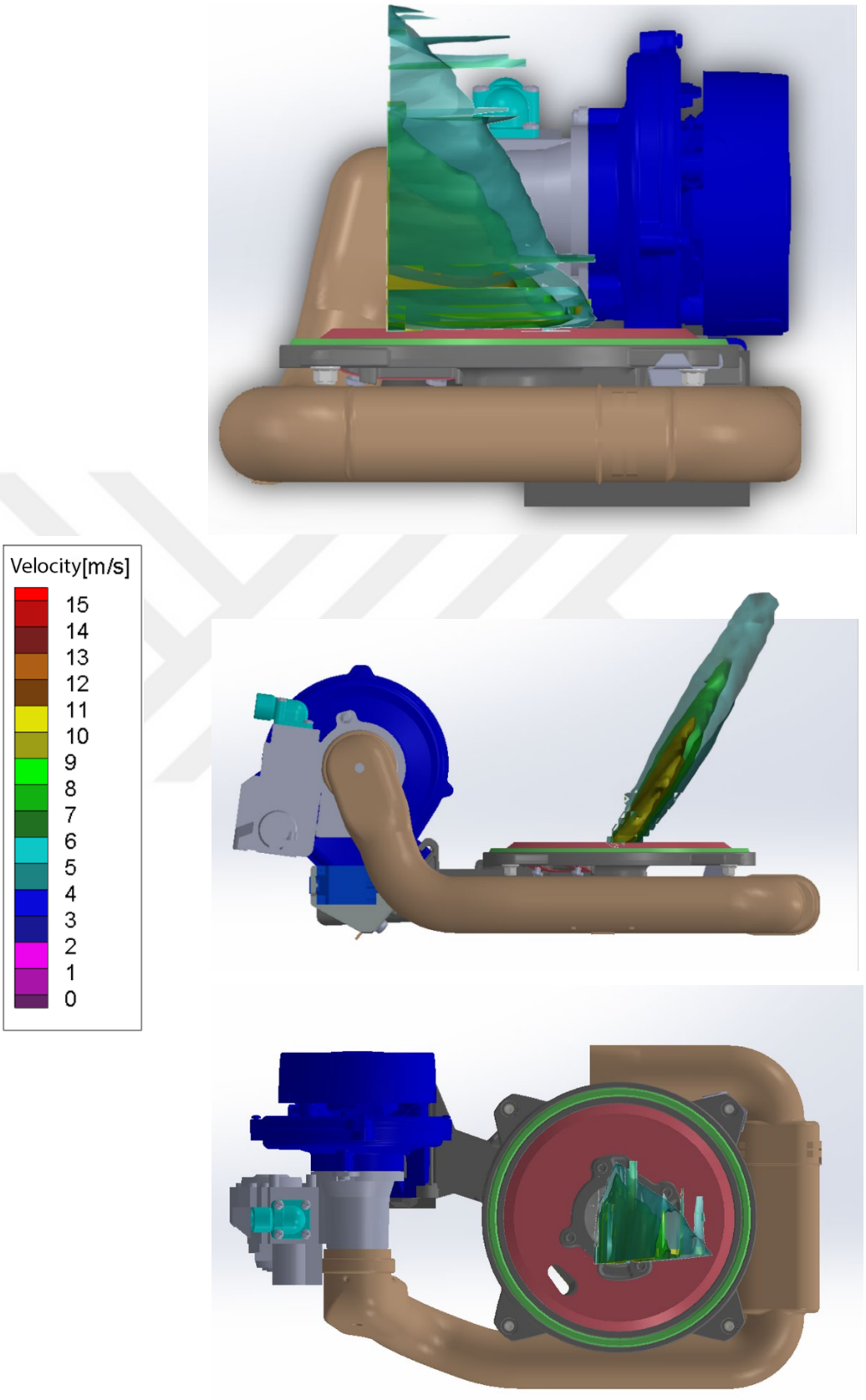


Figure 4.11 Fan-Burner system three-dimensional velocity 5 m/s, 8 m/s and 10 m/s iso-surfaces

In Figure 4.11, the flow is angled towards the front and right side after leaving the fan duct, a component that plays a crucial role in directing the flow. This shows that it is incorrect to assume homogeneous flow. The study's results demonstrate that this assumption, when applied in numerical studies that analyse the internal structure of the burner or the burner holes, can lead to a significant increase in the margin of error.

As a result of the investigation, volumetric data was created by interpolating the data obtained from 5 planes. However, the experiment resolution has a direct effect on the volumetric data. This situation is analysed in detail in Chapter 4.1.1.

4.1.1 The Spatial Resolution of Investigation Planes' Effect on Three-Dimensional Reconstruction of Jet Flow Structure of Fan-Burner System in Combi Boiler

The flow structure in the region described in Chapter 4.1, where the fan delivers the air-fuel mixture to the burner inlet, is of critical importance for burner and afterburner combustion volume investigations. Analysing this region with a high precision measurement method such as SPIV provides detailed information about the flow structure of the region.

In SPIV experiments, taking data over the examination planes at certain intervals and interpolating these data and converting them into volumetric data provides detailed information about the flow structure. However, in cases such as burner inlet, where the entire area of investigation can be geometrically visualised in the experiment, the examination of the region from a single plane increases the spatial resolution in order to increase the resolution of the experiment.

In order to increase the spatial resolution in SPIV experiments, the Fan-Burner system was placed in the experimental system with the burner inlet region parallel to the laser sheet (Figure 4.12).

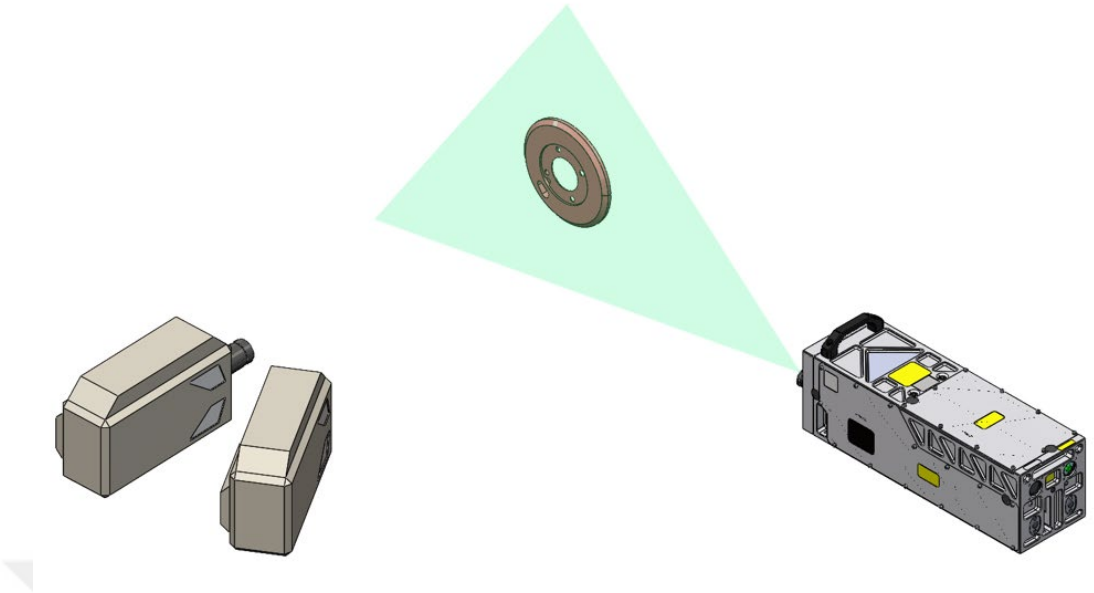


Figure 4.12 Schematic of Fan-Burner system experiment setup for SPIV

The fact that the entire burner inlet area can be seen with the cameras allows us to obtain experimental resolution directly related to the resolution of the cameras.

As can be seen in Figure 4.12, SPIV experiment was carried out after the calibration process with the placed fan-burner system. In Figure 4.13, there are 2 images belonging to the vertical and angled camera out of 600 images obtained after the experiment.

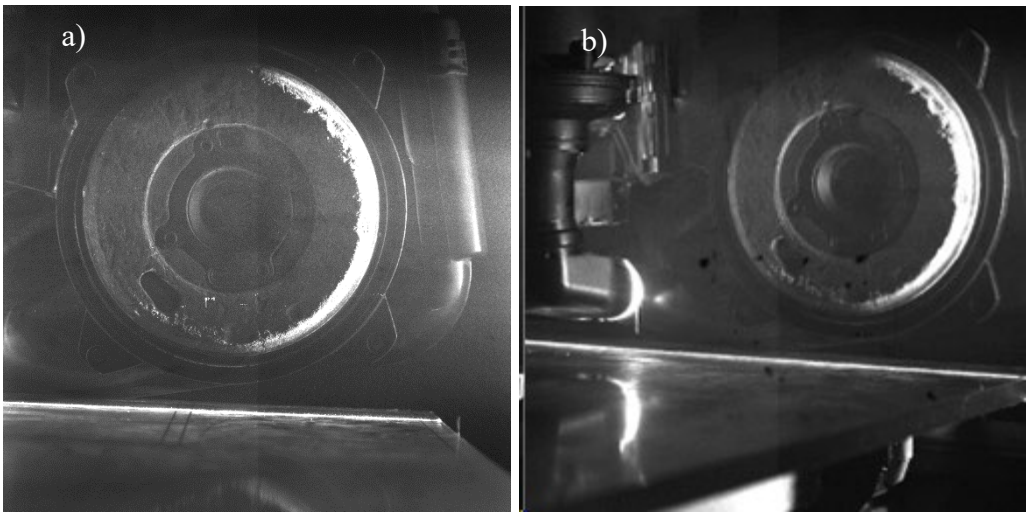


Figure 4.13 SPIV experiment images a) direct camera b) angular camera

The obtained 300 image pairs were processed by cross-correlation and velocity maps were obtained. The obtained velocity maps are presented in Figure 4.14.

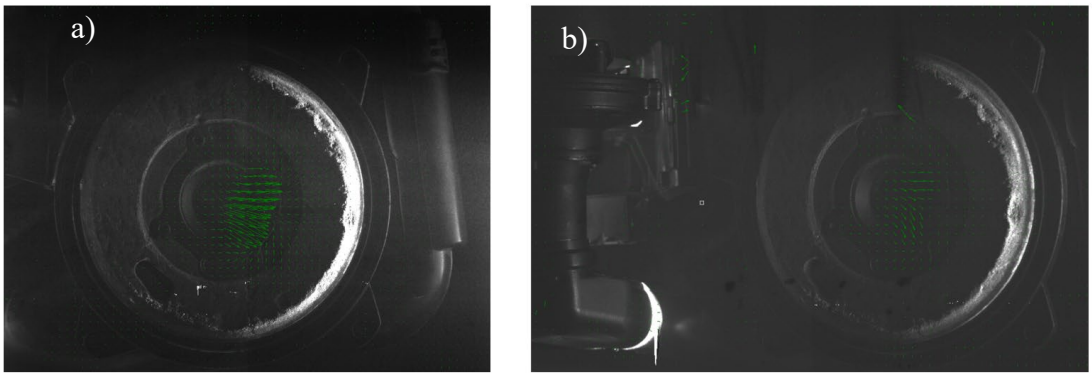


Figure 4.14 Velocity distribution obtained by SPIV of the burner inlet a) direct camera b) angular camera

The velocity data detailed in Figure 4.14 a and b can provide the velocity data of the entire area of interest without the need for interpolation. This increases the spatial resolution of the investigation area.

In order to make a comparison with the volumetric velocity data of the same area obtained by interpolation and presented in Figure 4.11, the velocity maps shown in Figure 4.13 were visualised volumetrically with TECPLOT software. The 7 m/s, 12 m/s and 20 m/s iso-surface results of the volumetric velocity data are presented in Figure 4.15.

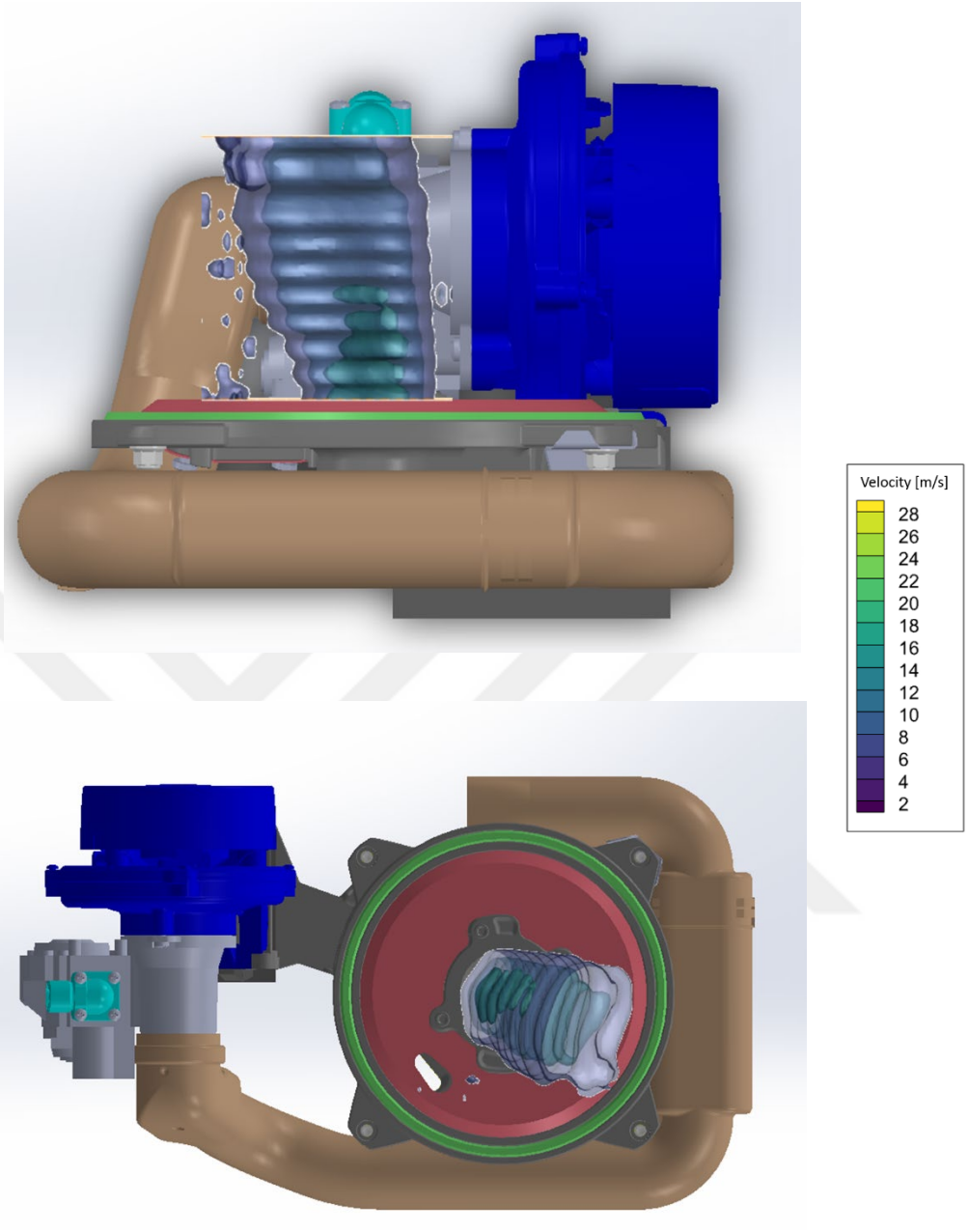


Figure 4.15 Fan-Burner system three-dimensional velocity 7 m/s, 12 m/s and 20 m/s iso-surfaces

When Figure 4.11 and 4.15 are analysed comparatively, it is seen that the errors in the intermediate regions due to interpolation are not present in Figure 4.4. Thus, it is shown that the spatial resolution of the region examined in the SPIV experiment is directly related to the examination region and the examination method.

It is aimed to transfer the obtained data to numerical studies by data assimilation, especially to be compared with the numerical studies in the literature where homogeneous boundary condition is assumed. Detailed information is given in Chapter 4.2.

4.1.2 The Burner Cover Effect on Flow Structure of Fan-Burner System in Combi Boiler

It is important to accurately obtain the boundary condition from the experiments when performing data assimilation for numerical studies. The 3D flow structures shown in Figures 4.11 and 4.15 are the results of SPIV experiments performed without the burner geometry connected to the fan duct.

Fans are devices with different flow rates according to the pressure difference. In the investigated fan-burner system, the pressure difference that will occur when the burner is installed in the fan duct may affect the operating point of the fan. In order to investigate this situation and to obtain a boundary condition with higher reliability as a result of numerical studies, the cover of the burner inlet area shown in Figure 4.16 was prepared with a 3D printer.

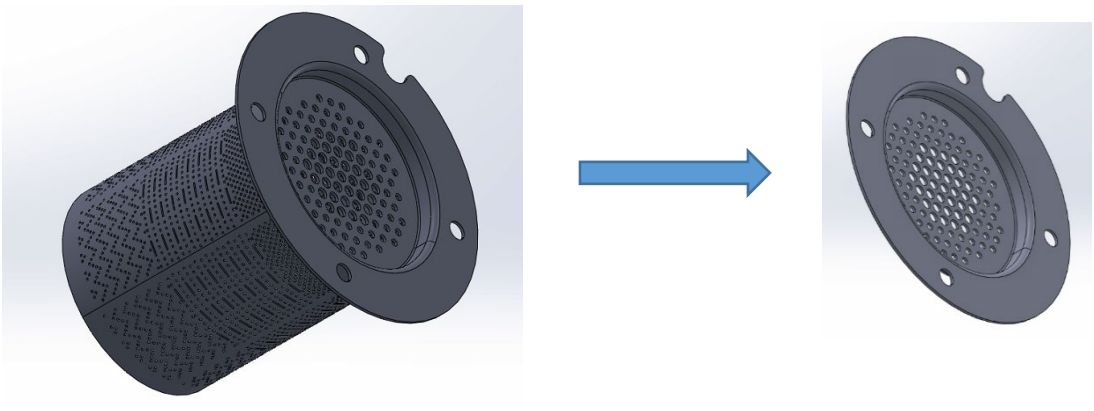


Figure 4.16 Burner inlet cover

The part prepared with 3D printer was fixed to the duct-outlet region of the fan-burner system mentioned in Chapter 4.1 and 4.1.1. The system was placed in the SPIV setup and the experiments were carried out in such a way that the spatial resolution mentioned in Chapter 4.1.1 was increased and the cameras were viewed from the

opposite side. The raw images obtained as a result of the experiments are presented in Figure 4.17.

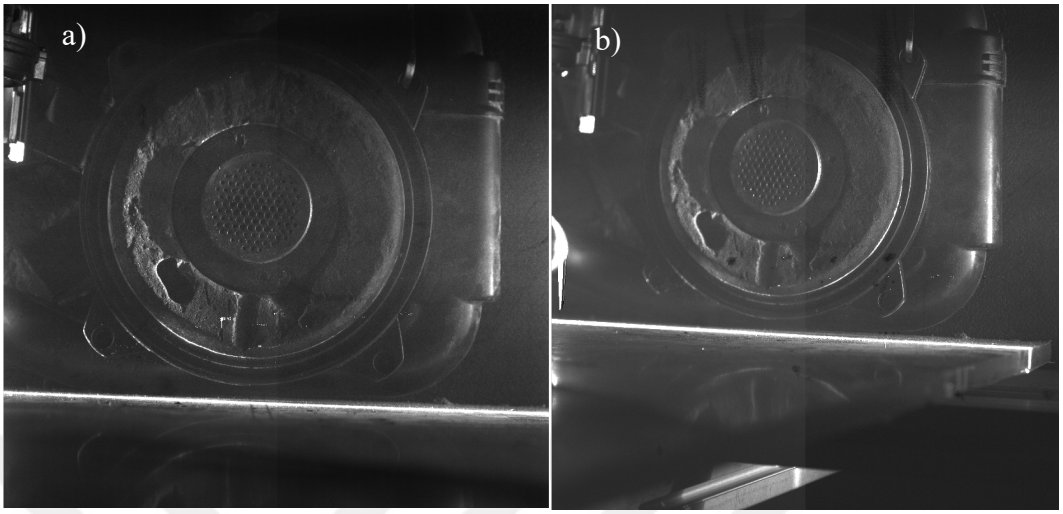


Figure 4.17 Velocity distribution obtained by SPIV of the burner inlet a) direct camera b) angular camera

The raw images were processed with the cross-correlation method and velocity vectors were obtained for images from 2 different angles. When the velocity vectors were superimposed on both the vertical camera image and the angled camera image, the maps in Figure 4.18 were created.

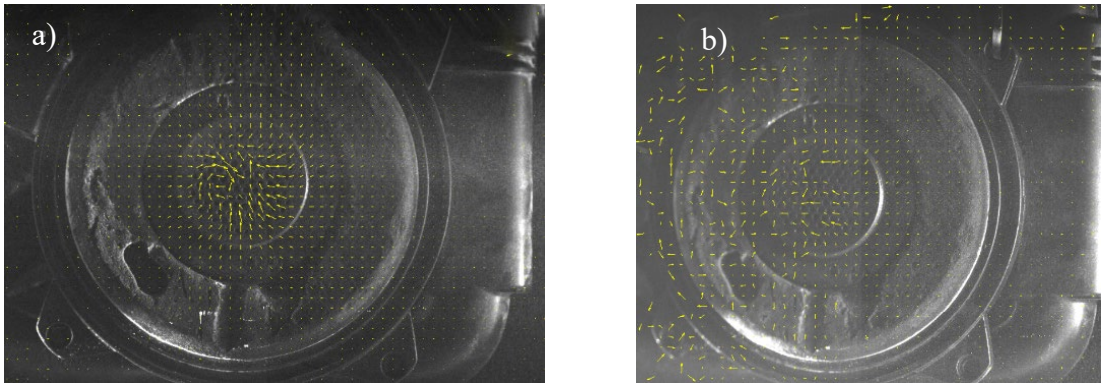


Figure 4.18 Velocity distribution obtained by SPIV of the burner inlet a) direct camera b) angular camera

The velocity maps obtained from two different angles were processed in stereo to obtain two-dimensional three-component velocity maps. The SPIV result is presented in Figure 4.19.

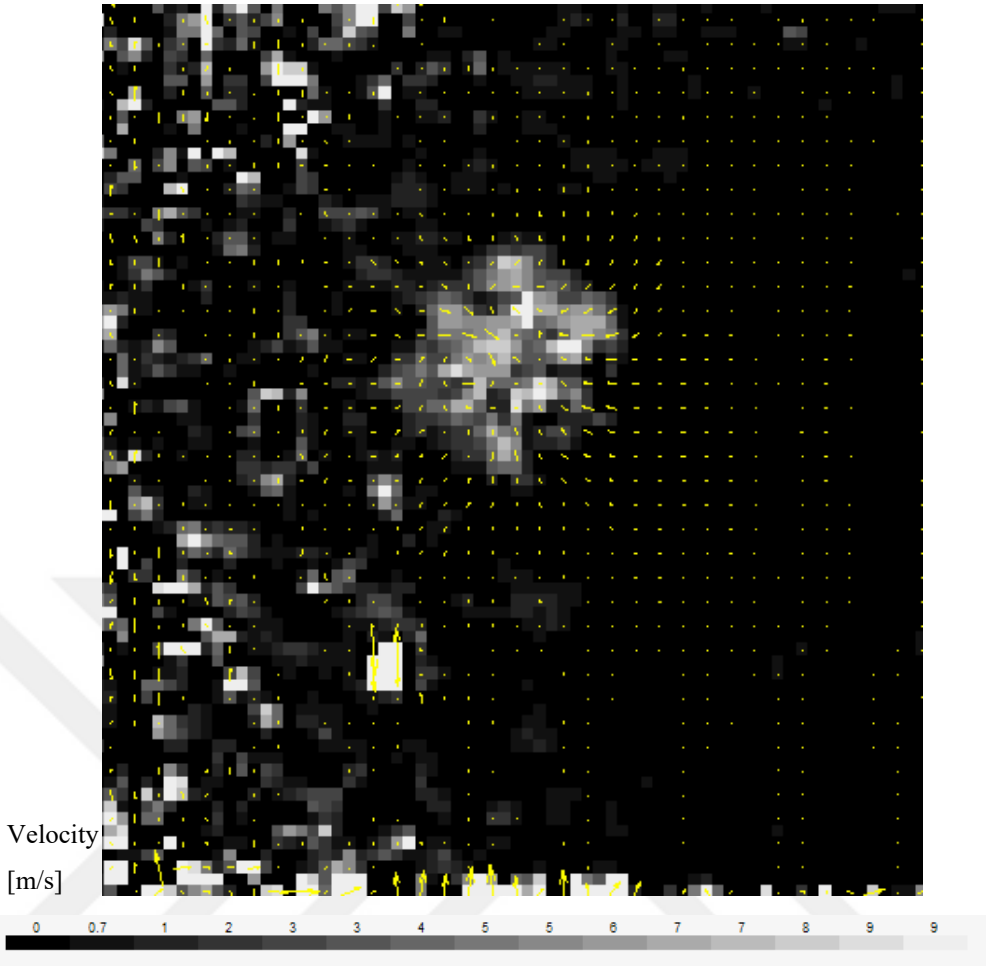


Figure 4.19 Stereo velocity distribution obtained by SPIV of the burner inlet

The vector magnitude change seen in the centre region in Figure 4.18 shows the region where the burner inlet is located. It is seen that the velocity in the z direction (out of the plane) is high in this region.

The obtained data were defined as boundary conditions in numerical studies with the data assimilation method, which has not been applied in the literature before, and verification studies were carried out. Detailed information is presented in Chapter 4.2.

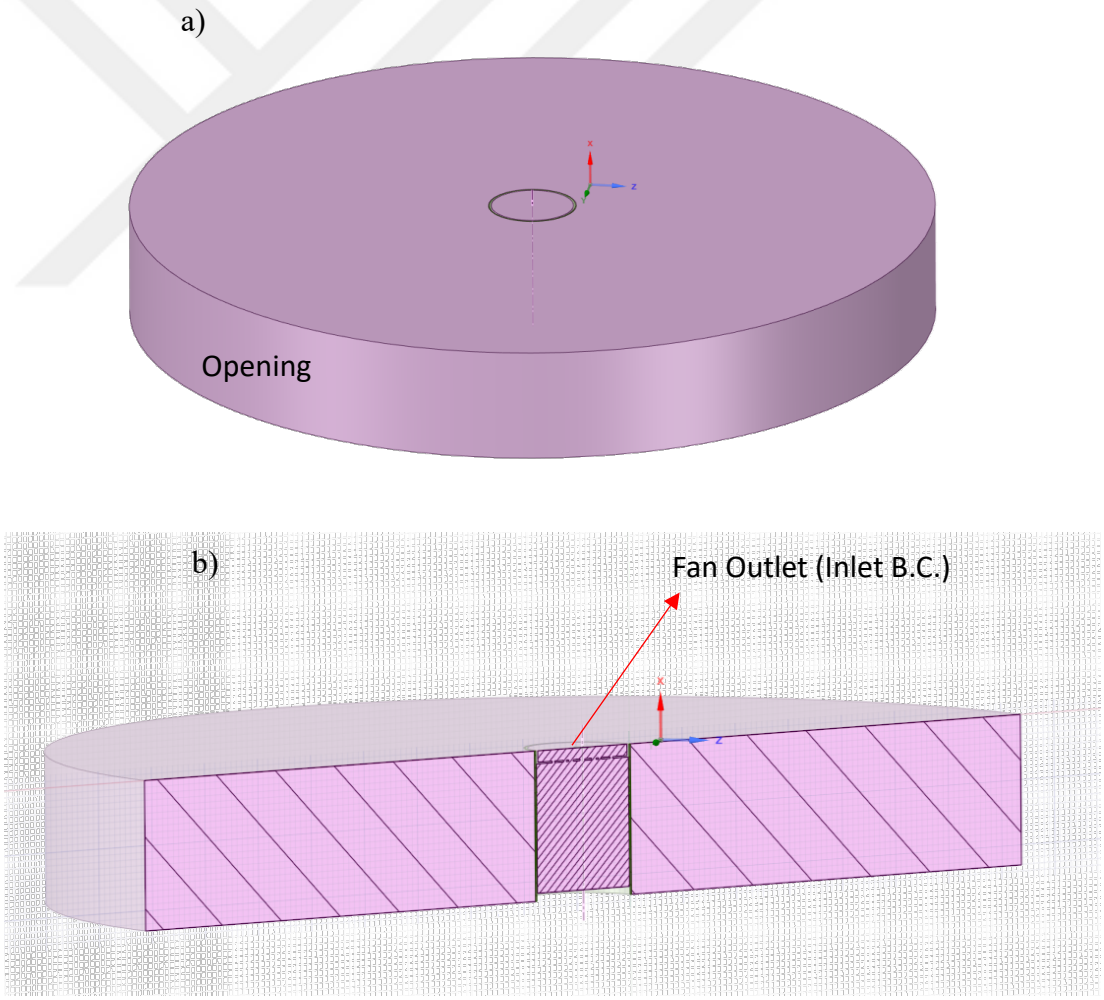
4.2 Numerical Investigation of Combi Boiler Fan-Burner System by Data Assimilation with Stereo Particle Image Velocimetry

The flow structure of the fluid inside and outside the burner is critical in a combi boiler. This aspect significantly affects the homogeneity of the combustion process and, consequently, directly impacts heat transfer, gas emissions, and energy efficiency.

Numerous studies addressing this phenomenon can be found in the literature, with detailed information provided in Chapter 1.1.3.

In the literature studies, it is assumed that the flow rate of the air-fuel mixture is the same in all burner outlet holes. However, SPIV experiments in Chapter 4.1 show that the flow in the burner inlet area is not homogenous. The most important reason for this is the use of centrifugal fans.

In order to use the experimental data obtained in Chapter 4.1 with data assimilation as a boundary condition in numerical studies, a numerical study of the combustion volume from the burner inlet was carried out. The fluid domain of the region is shown in Figure 4.20.



c)

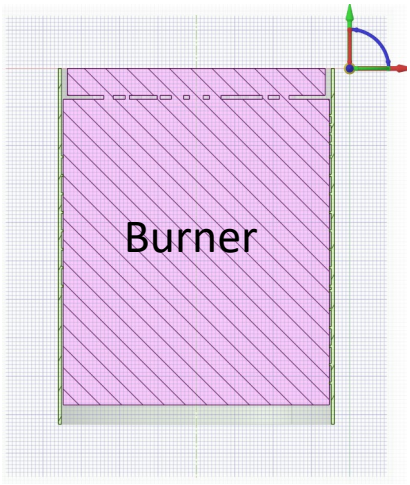


Figure 4.20 Fluid domain to investigate burner flow structure a) burner and environment b) cross-section of fluid domain c) burner fluid domain

In order to analyse the fluid domain numerically, a network structure was constructed. The holes of the burner leading to the combustion zone of the air-fuel mixture are approximately 0.8 mm in diameter. In order to investigate 3276 holes numerically, the mesh density in this narrow region must be made reliably. The mesh structure presented in Figure 4.21 was created.

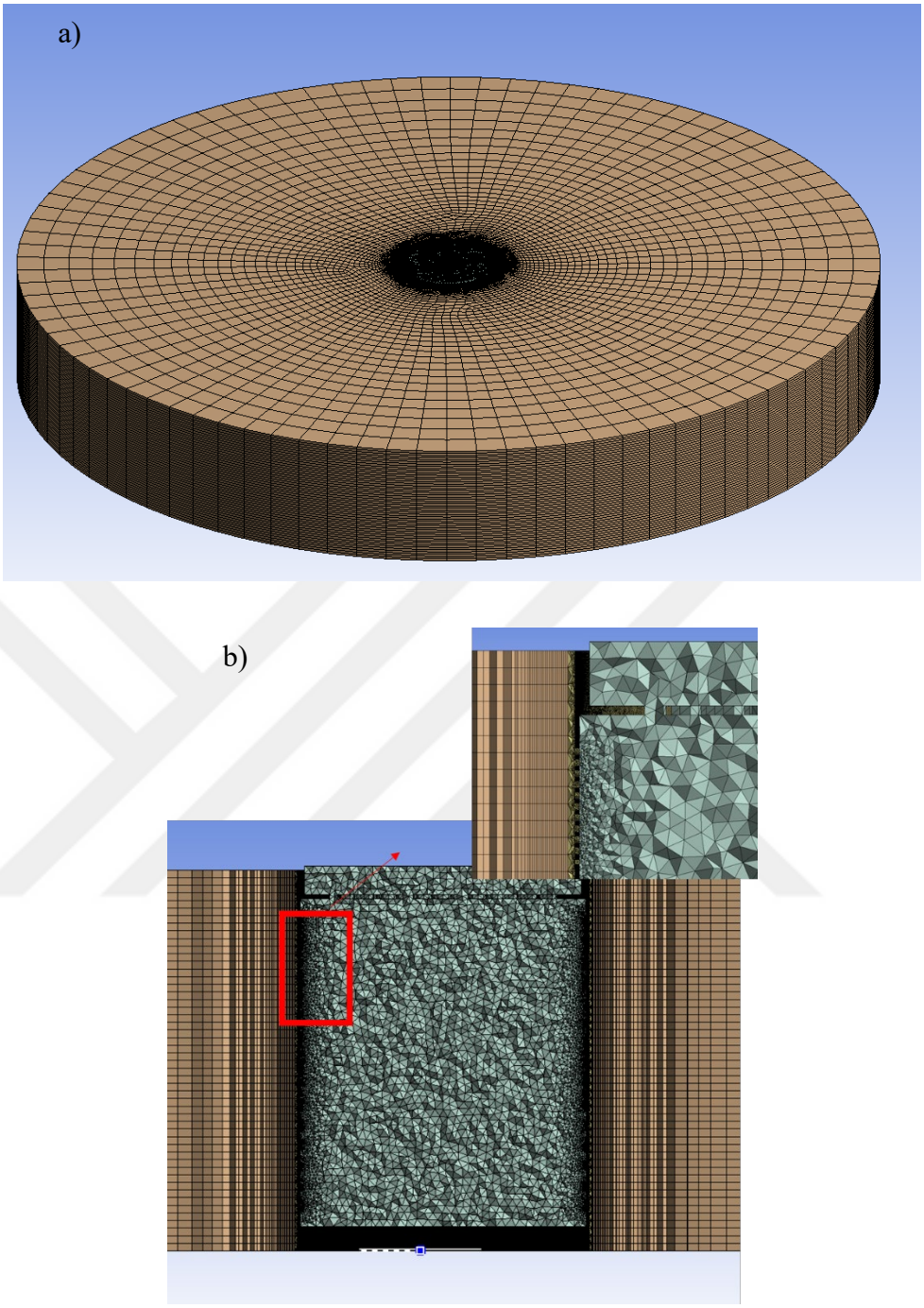


Figure 4.21 Mesh structure of fluid domain a) mesh structure b) details of mesh

The mesh structure shown in Figure 4.21 has approximately 30 million elements. Although this number seems to be negative for computational cost, it is acceptable due to the hole diameters. The validation data obtained from the SPIV experiments described in this chapter support this conclusion.

To compare the inlet boundary condition defined by the data assimilation method, a constant flow rate inlet boundary condition was defined, as it is commonly done in the literature. To define the burner inlet zone, the average flow rate of the inlet zone was determined as 0.0101 kg/s using the velocity data obtained from SPIV experiments. This flow rate was then defined as the inlet boundary condition to the fan outlet section in Figure 4.20.

In order to define the volumetric velocity distribution obtained by SPIV to the input region in the numerical study, a matrix containing experimental results, including position information and velocity information, was created. The matrix obtained from the experimental study and the location information obtained from the numerical study are compared and matched according to the nearest neighbour algorithm, and the data obtained from the experiments are defined for each mesh on the surface where the boundary condition is located. The nearest neighbour algorithm is reliable for studies with a high density of measurement points, such as SPIV, because there are approximately 13 times more experimental measurement points in the meshed surface than the number of elements.

Figure 4.11 shows the volumetric data generated by interpolating the 2D results obtained from 5 different planes with the TECPLOT programme and defined as a boundary condition to the numerical model in Figure 4.22.

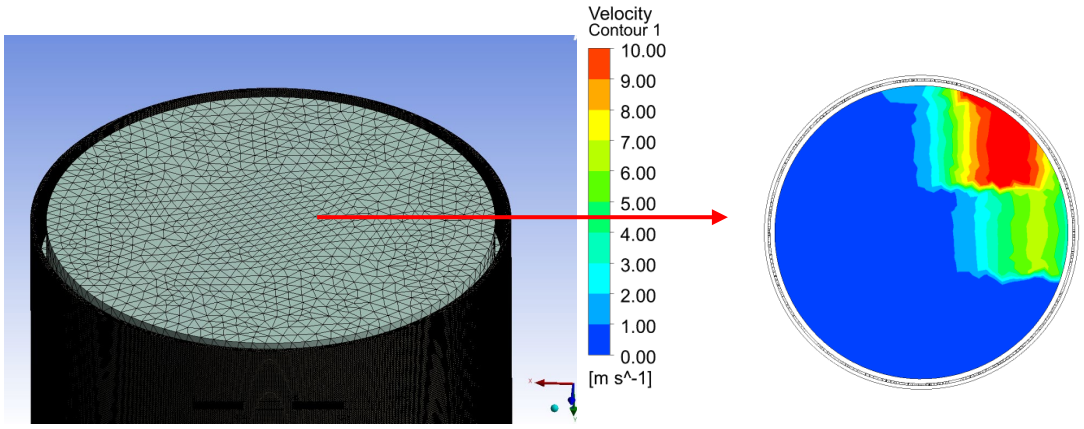


Figure 4.22 Data assimilated inlet boundary condition

The vectorial representation of the boundary condition defined by data assimilation and its comparison with the experimental volumetric data is presented in Figure 4.23.

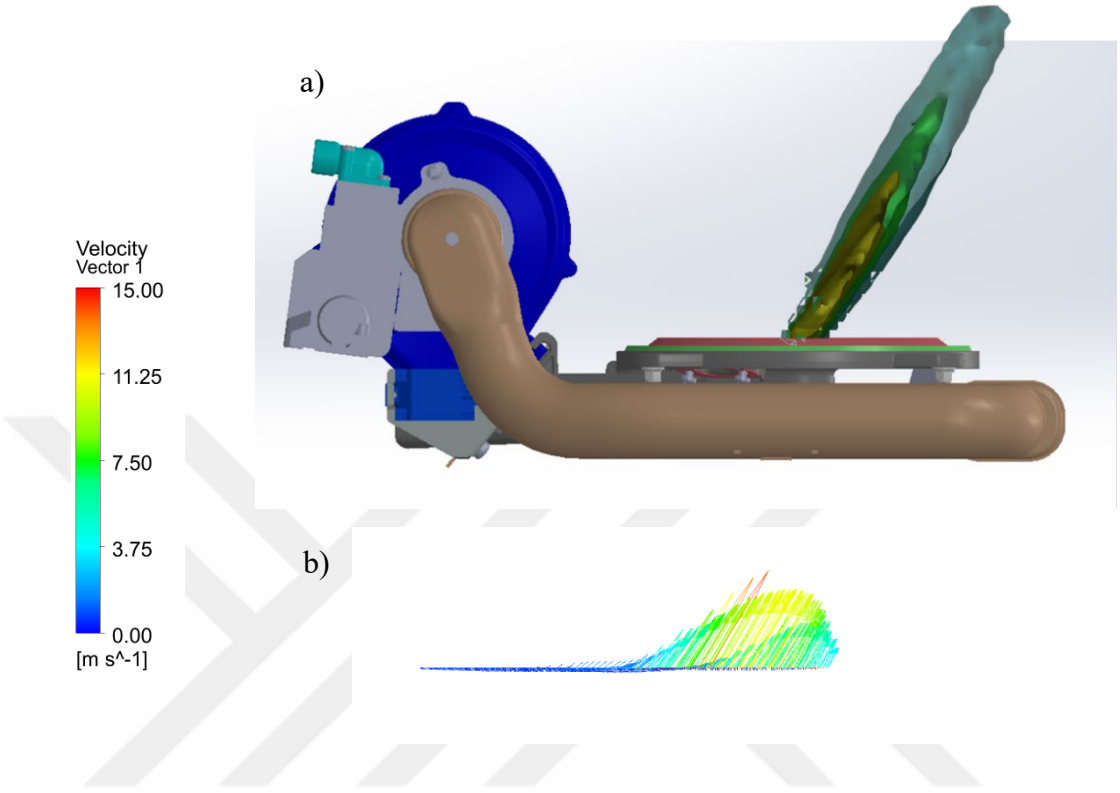


Figure 4.23 Data assimilated inlet boundary condition comparison with SPIV volumetric velocity results a) generated volumetric velocity distributions using SPIV b) data assimilated boundary condition

Figure 4.23 shows the volumetric velocity distribution obtained by SPIV experiments and the boundary condition defined in the CFD analysis by data assimilation method. Two analyses were carried out in the burner inlet region, one with a constant flow rate boundary condition as frequently accepted in the literature and the other with the assimilated results from the SPIV experiments as the boundary condition as shown in Figure 4.23. Figure 4.24 shows the results of these analyses showing the velocity distribution in the burner inlet region.

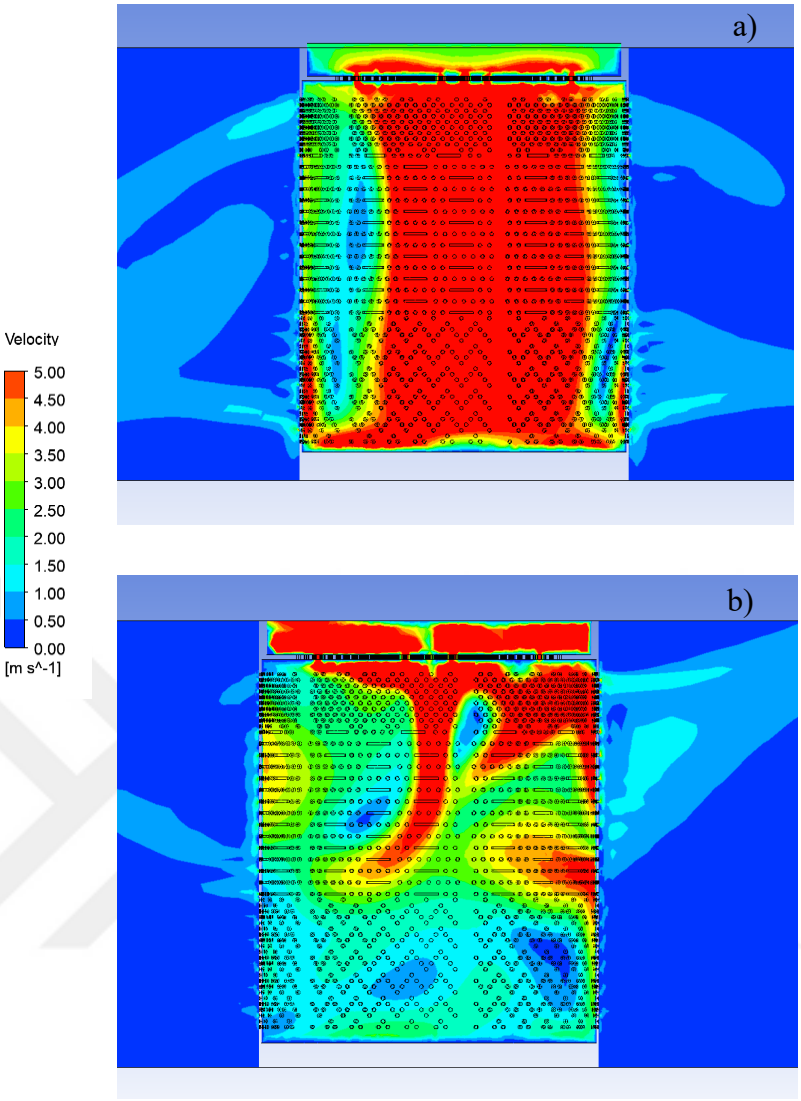


Figure 4.24 Velocity distributions of burner inside a) homogeneous flowrate B.C. b) data assimilated B.C.

In Figure 4.24-a, where the homogeneous flow rate boundary condition is defined, it is seen that the flow structure is significantly different from that in b, where the boundary condition is defined using experimental data. The differences in the flow structure in the inner region of the burner also affect the velocity and direction of the flow from the burner holes to the combustion volume.

In order to gain a better understanding of the data assimilation method, various numerical studies were conducted to investigate the effect of spatial resolution discussed in Chapter 4.1.1. The inlet boundary condition was defined by assimilating data obtained from five different planes using SPIV method (Chapter 4.1). This

resulted in the inlet velocity profile displayed in Figure 4.22. However, the region between the five planes was calculated using interpolation.

To improve the accuracy and resolution of the inlet region, a volumetric velocity distribution was obtained by increasing the spatial resolution of experiment discussed in Chapter 4.1.1. This was then utilized as a boundary condition in the numerical study. The results of the study are presented in Figure 4.25. This figure shows the experimental result obtained with high spatial resolution of the inlet region and the boundary condition defined in the numerical study by data assimilation.

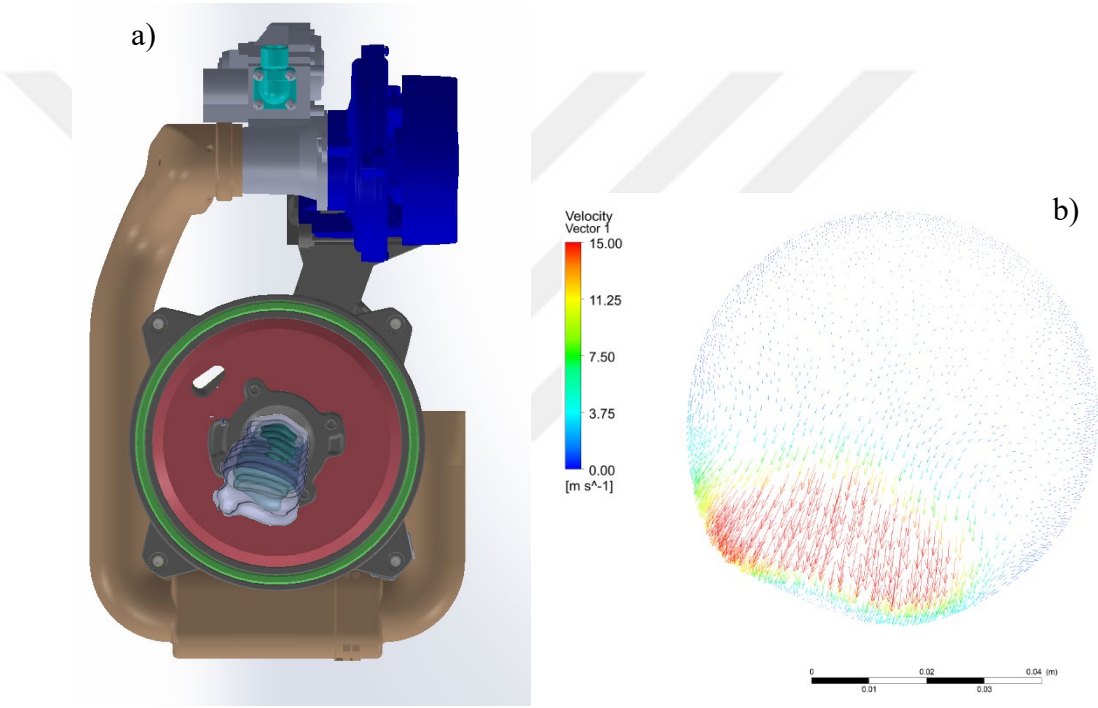


Figure 4.25 a) Volumetric velocity distributions obtained by SPIV b) Inlet boundary condition by data assimilated volumetric velocity data

The numerical study where the volumetric data obtained from the high spatial resolution experiment is defined as the inlet boundary condition is compared with the numerical study where the volumetric data obtained from the interpolated experiment is defined as the boundary condition. The comparison is presented in Figure 4.26.

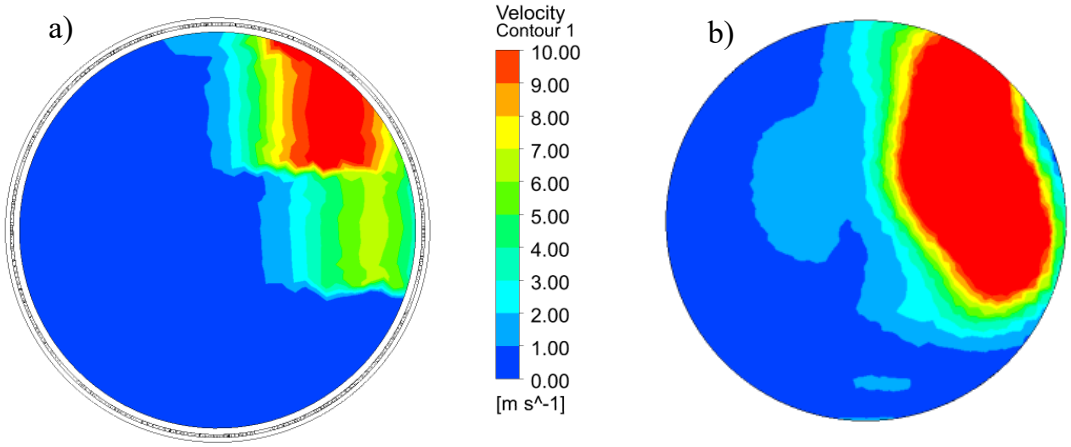


Figure 4.26 Inlet boundary condition by data assimilated volumetric velocity data a) interpolated data from SPIV b) directly used SPIV data

Although the boundary conditions obtained from two different experiments appear to be regionally close, they differ from each other, especially in terms of the velocity magnitude and width of the high-velocity region. The boundary conditions, which are similar in terms of the direction of the velocity, show large differences in terms of the magnitude of the velocity in Figure 4.26-b, where the resolution of the experiment is increased. This difference is presented in detail in Figure 4.27 with velocity vectors.

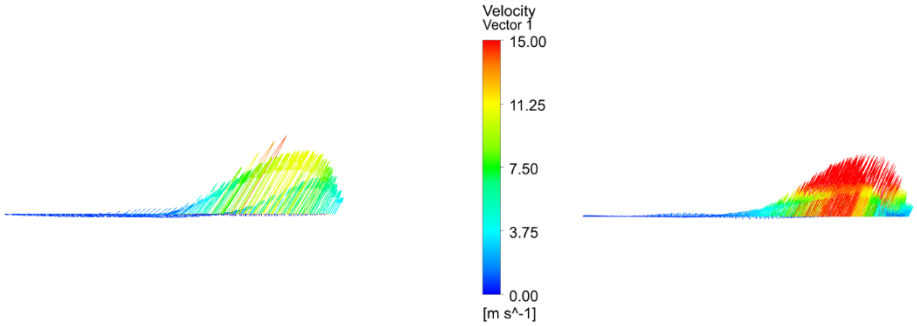


Figure 4.27 Velocity vectors of inlet boundary condition a) interpolated data from SPIV b) directly used SPIV data

To the analyses with the homogeneous constant flowrate boundary condition and the boundary condition obtained by data assimilation by interpolating the experimental data, which are presented in Figure 4.24, the results of the analyses using high-

resolution direct SPIV data as a boundary condition were added. In all three analyses, the velocity map results from the mid-plane of the burner are presented in Figure 4.28.

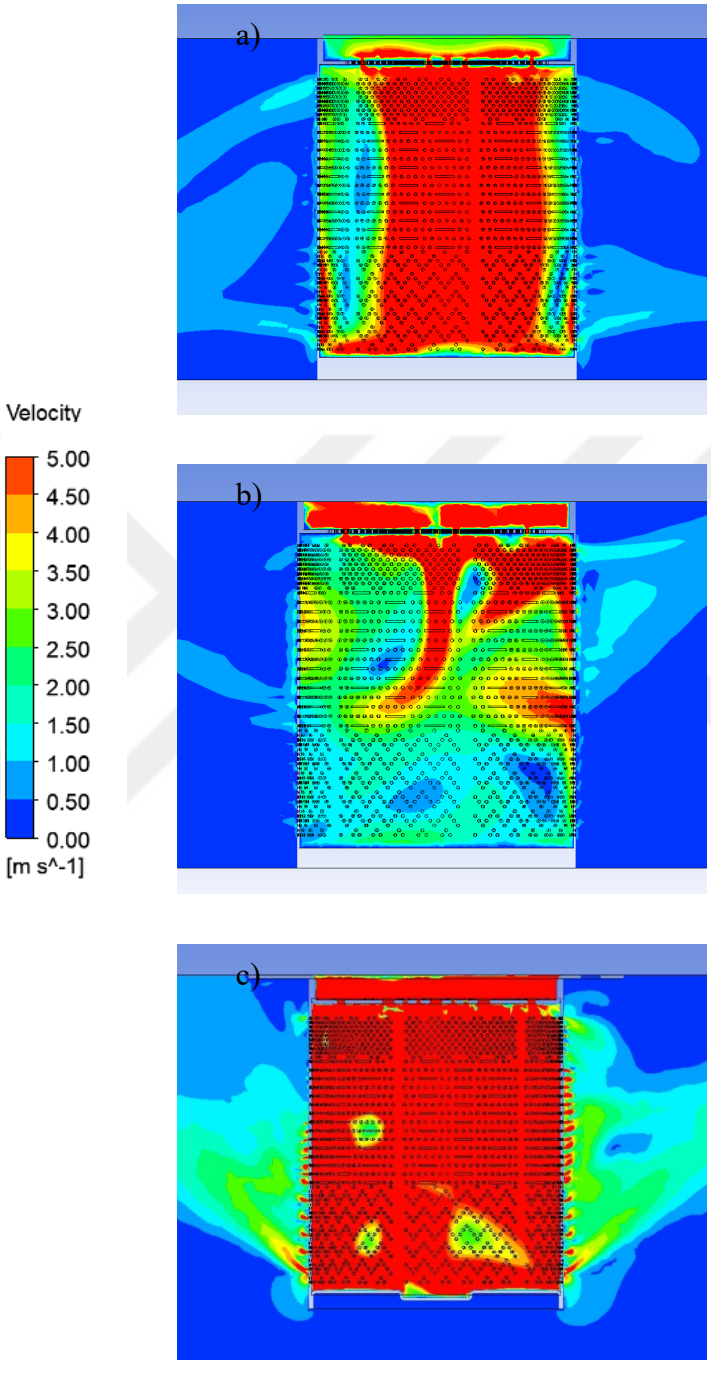


Figure 4.28 Velocity distributions of burner mid-plane a) homogeneous flowrate B.C. b) data assimilated B.C. from interpolated data from SPIV c) data assimilated B.C. from directly used SPIV data

The velocity distribution in the burner's mid-plane contains different flow structures and magnitudes for each inlet boundary condition definition. This difference directly affects the examination and design processes of the internal structure of the burner and the examination and development processes of parameters such as emission and performance by examining the combustion volume. Boundary condition definitions in this region, which are far from the actual situation, will seriously increase the margin of error in the analyses. For this reason, to validate the results obtained from 3 different analyses, the velocity distribution of the air coming out of the burner holes was obtained by SPIV experiments. The images obtained in the SPIV experiment are presented in Figure 4.29.

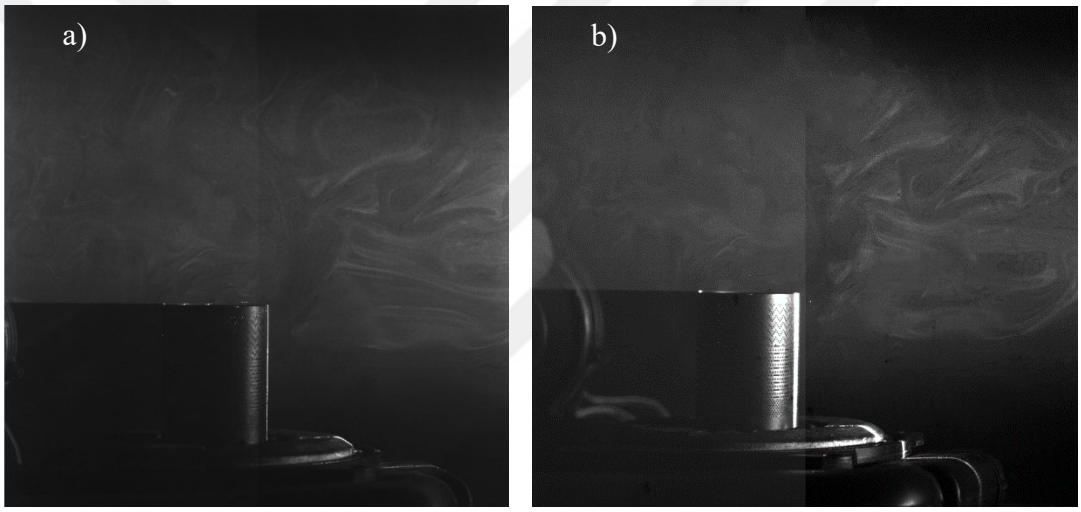


Figure 4.29 SPIV experiment images a) direct camera b) angular camera

The obtained images were processed by cross-correlation and SPIV result was obtained. The result is presented in Figure 4.30.

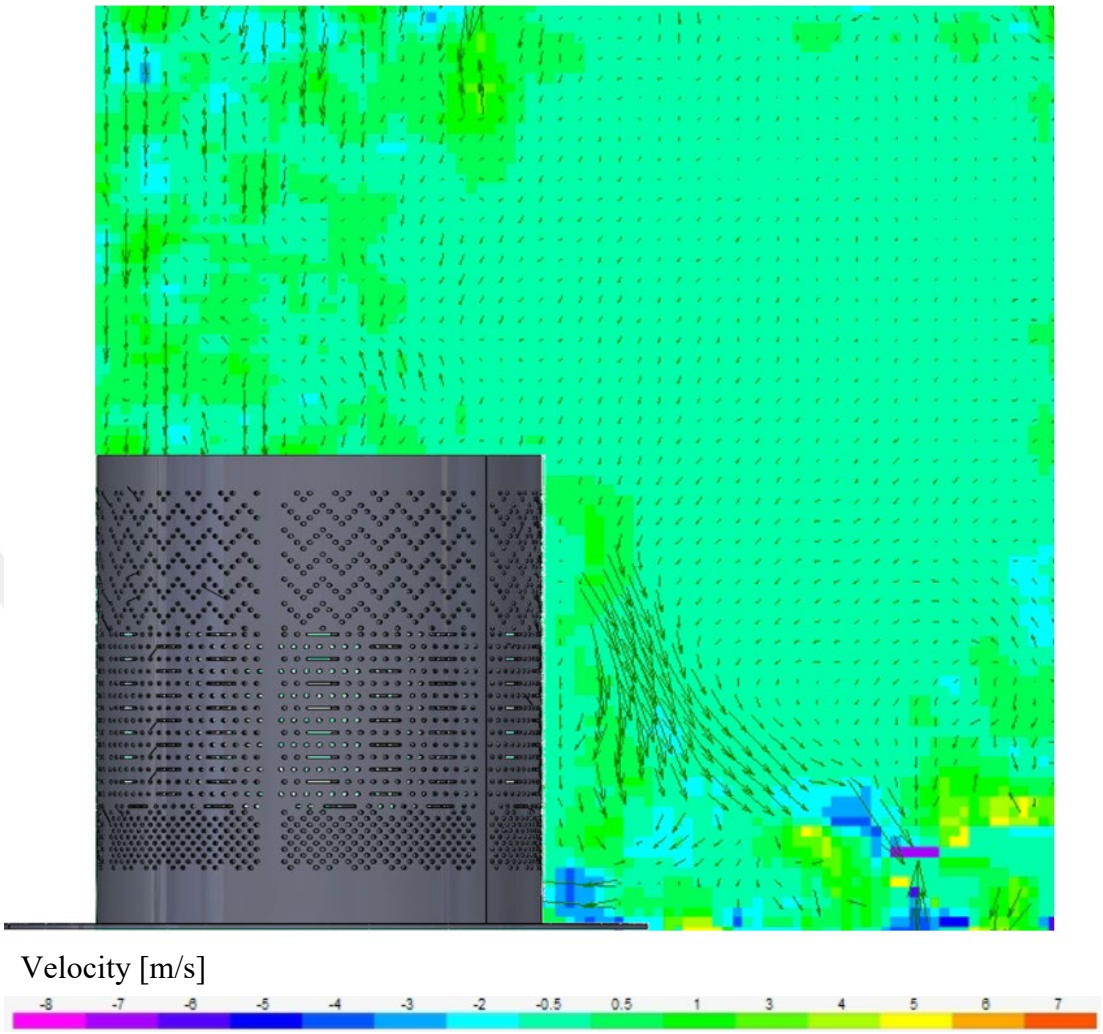


Figure 4.30 SPIV two-dimensional three component velocity distributions of burner surface

As a comparison parameter over the velocity distribution obtained as a result of the experiment, a line 10 mm ahead of the burner surface was determined as a validation line (Figure 4.31).

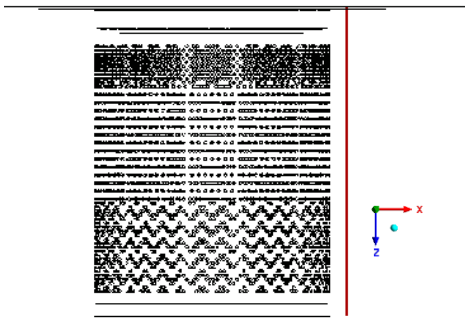


Figure 4.31 Validation line (red)

The main reason why the verification line is close to the surface is to compare the jet flow values coming out of the holes. For this reason, velocity data were obtained over the line. The velocity distribution on the line obtained as a result of SPIV experiments and numerical studies is presented in the graph in Figure 4.32.

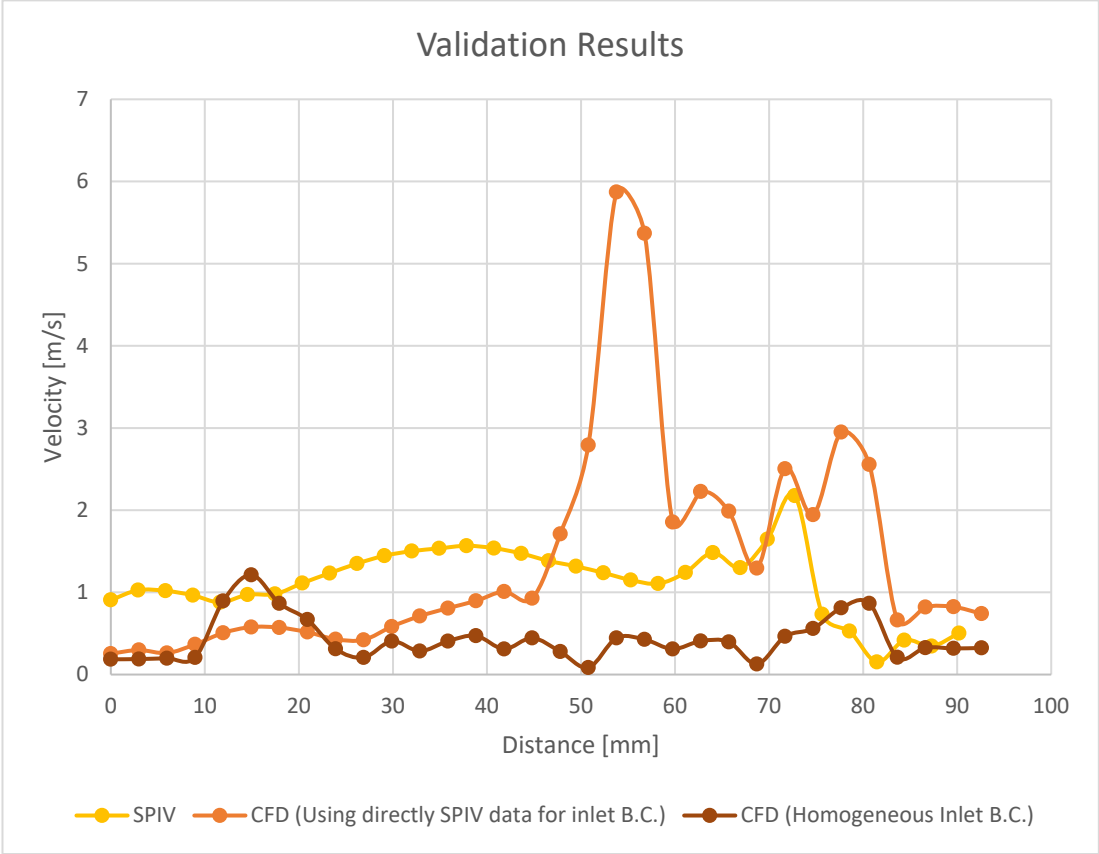


Figure 4.32 Velocity distribution of validation line at Figure 4.31

The results obtained from CFD and SPIV show that the velocities are very low in the 0-50 mm distance range. However, in the 50-100 mm range, which is the middle lower region of the red line in Figure 4.31, it is seen that the high-velocity peaks in CFD that directly assimilated by SPIV are not present in SPIV. In addition, significant differences are observed between the analysis with homogeneous inlet boundary conditions and SPIV results in terms of both flow structure and velocity magnitudes. This result shows that the analyses in which homogeneous flowrate and the assimilated data was defined as the inlet boundary condition gave inaccurate results. In addition, since a single validation line may have a high margin of error, a second line was used as a validation line. The second line was placed at a distance of 10 mm from the surface of the burner at 90 degrees to the first line. The positioning of the line is shown in Figure 4.33.

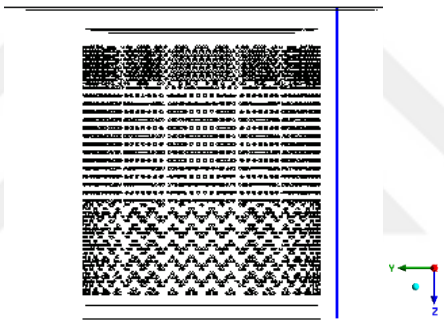


Figure 4.33 Second validation line (blue)

In the SPIV experiments, the velocity distribution was obtained from a line at the same location in Figure 4.33 and compared with the CFD results. The comparison results are presented in Figure 4.34.

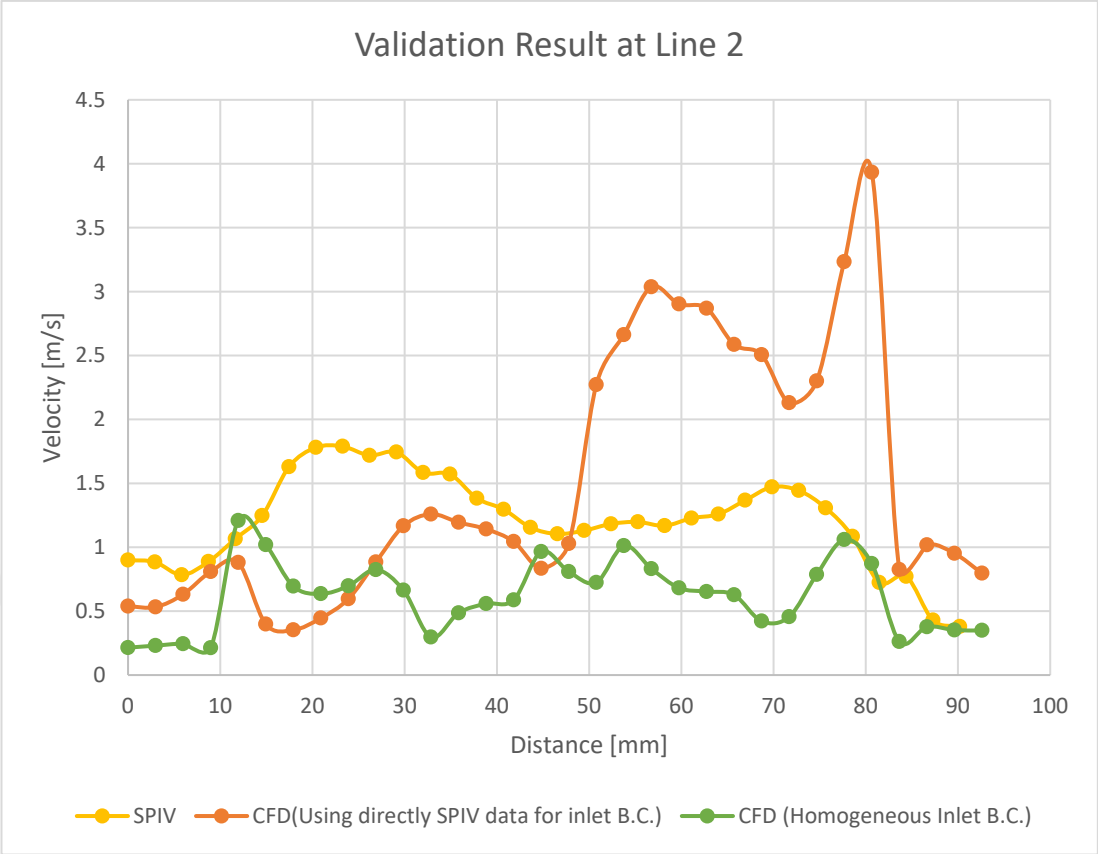


Figure 4.34 Velocity distribution of validation line at Figure 4.33

Different flow structures are observed in the second validation line, especially between 50 and 100 mm. The main reason for this situation is the burner cover effect, explained in detail in Chapter 4.1.2.

The pressure differences the burner cover creates directly affects the flow at the burner inlet, inside and at the burner outlet holes. For this reason, the assimilation of the volumetric velocity data obtained from the SPIV results in Chapter 4.1.2 was added to the numerical analyses and defined as an inlet condition. The result of the analysis where SPIV experiments with burner cover in Chapter 4.1.2 are used as inlet boundary condition by data assimilation is given in Figure 4.35.

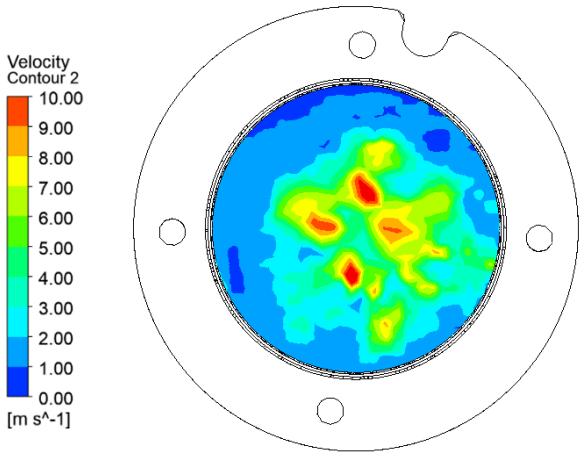


Figure 4.35 Inlet boundary condition by data assimilated volumetric velocity data from SPIV experiment with burner cover geometry

The inlet boundary condition obtained as a result of SPIV experiments with burner cover differs significantly from the interpolated and directly defined experimental results in Figure 4.26, both in terms of size and location of the high-velocity zone. This situation affects the flow of the burner. For this reason, there are also differences in the fluid flow structure coming out of the burner holes. The velocity distribution was also taken from the analysis result in which the effect of the burner cover was included in the validation lines shown in Figures 4.31 and 4.33. The results obtained are presented in Figure 4.36.

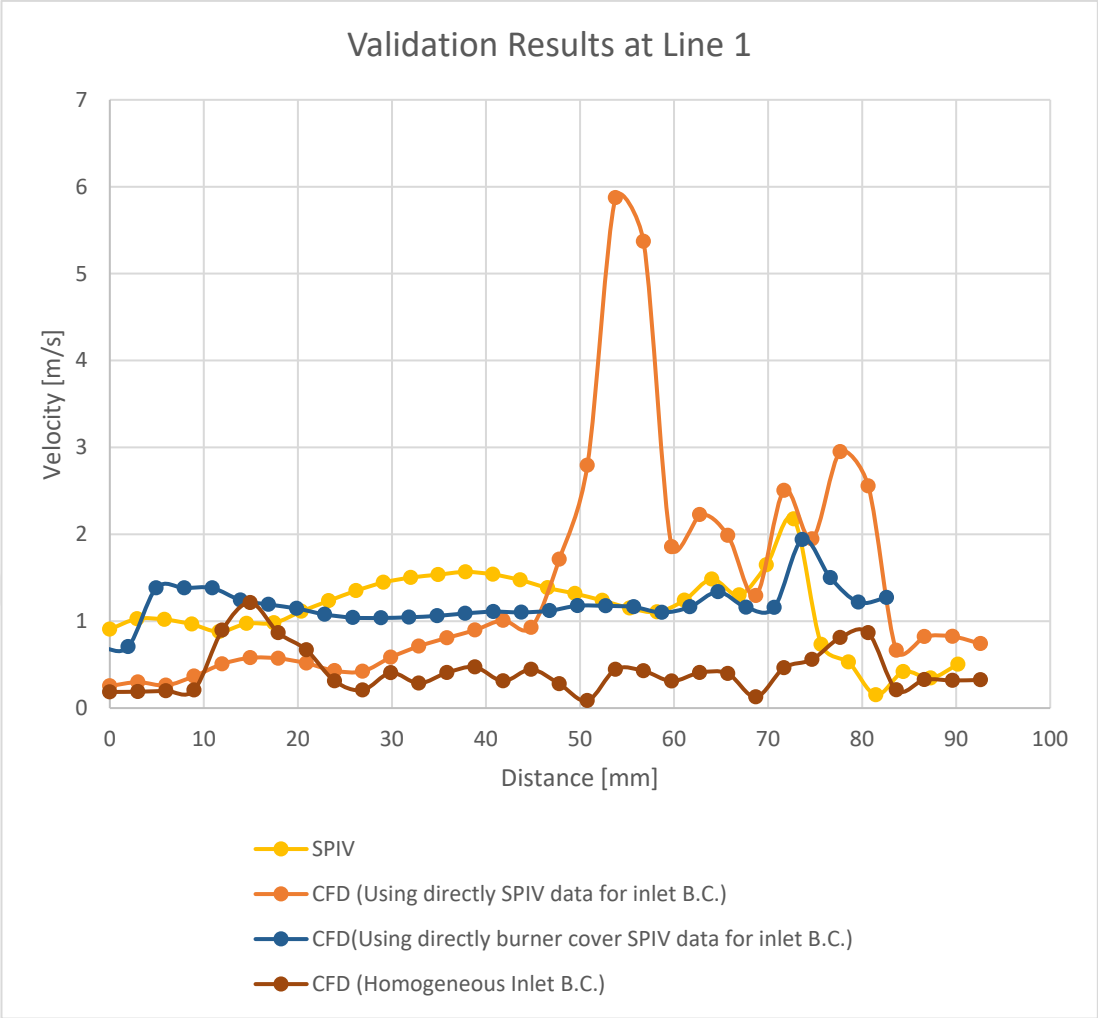


Figure 4.36 Velocity distribution of validation line at Figure 4.31

When the SPIV results are compared with the data assimilated and homogenous boundary conditions, there is a significant difference with the data assimilated analysis without the burner cover effect. Especially in the analysis without the burner cover effect, it is observed that there are many high-velocity regions. In addition, the average velocity of the SPIV result is 1.13 m/s, while it is around 1.41 m/s in the analysis without the burner cover effect. This shows that there is an error of approximately 25%. In the homogeneous boundary condition definition, the average velocity is 0.42 m/s and the error is about 62% compared to experimental.

The analysis using the data assimilated from the SPIV with the burner cover is similar to the SPIV results in terms of flow structure. In both the analyses and experimental results, there is a low-velocity flow with no peak value before 60 mm,

while there are two velocity peaks in the same regions after 60 mm. In addition, the average velocity of the SPIV result is 1.13 m/s, while the analysis result is 1.12 m/s. This shows that the analysis is validated with the experimental results with a margin of error of approximately 1%.

The analysis using the data assimilated from the SPIV with the burner cover is also validated from analysis line 2. For this, a second validation was performed on a line positioned at 90 degrees to line 1, shown in blue in Figure 4.33. The velocity results obtained from Line 2 are presented in Figure 4.37.

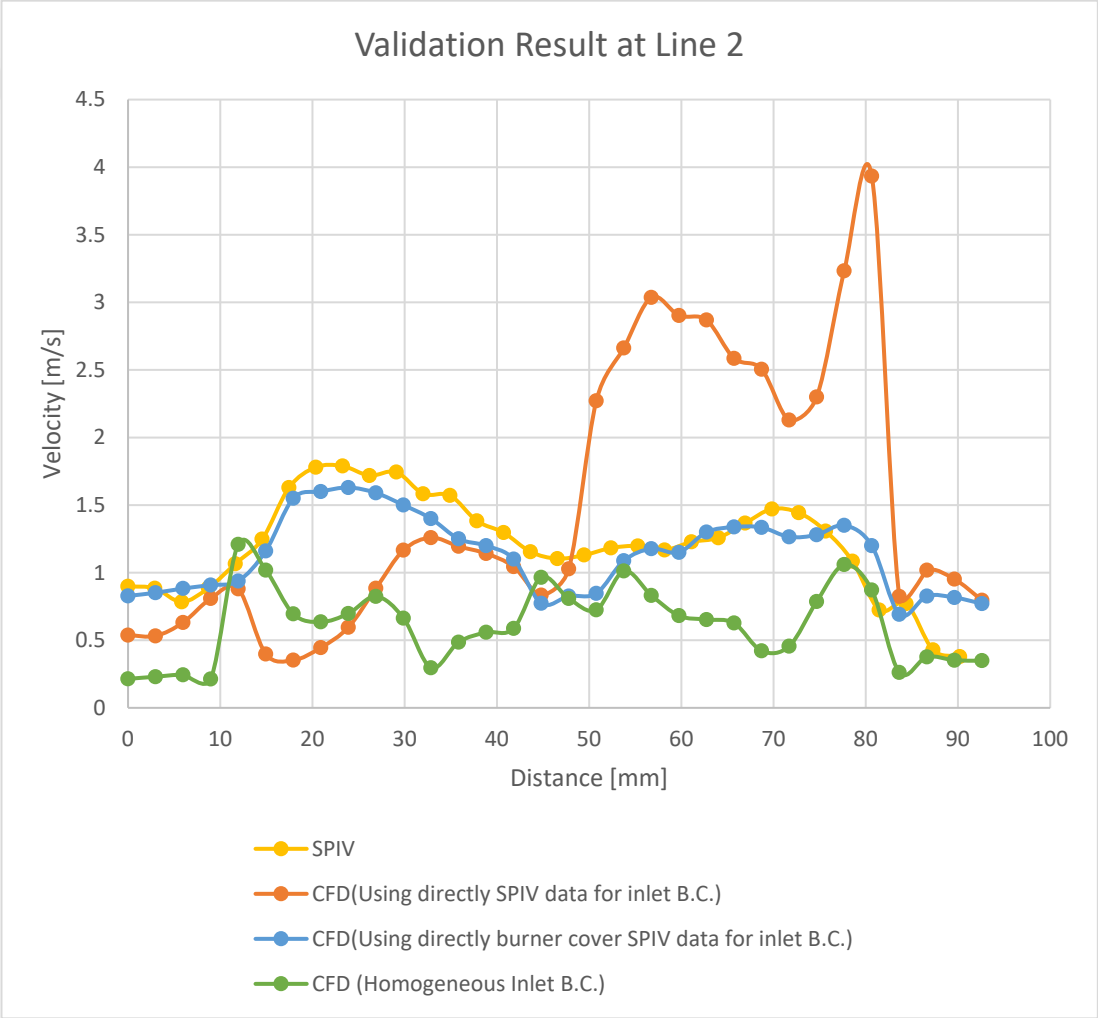


Figure 4.37 Velocity distribution of validation line at Figure 4.33

The burner cover effect is clearly seen on Line 2. While there are high velocity regions in the analysis without burner cover effect, it is seen that these regions do not

exist in the SPIV results. In addition, while the average velocity was 1.21 m/s in the SPIV results, it was obtained as 1.49 m/s in the analyses without burner cover. This situation, which means a margin of error of approximately 24%, shows that when the burner cover is not included, even if the boundary condition is defined from the experimental data, large margins of error occur in terms of both flow structure and average velocity. In the homogeneous boundary condition definition, the average velocity is 0.62 m/s and the error is about 48% compared to experimental.

As in Line 1, in the validation made on Line 2, it is seen that the numerical analysis using the experiments, including the pressure effect created by the burner cover, has a flow structure compatible with the SPIV experimental results. It is concluded that the velocity increase with the same characteristic in certain regions on the line, and the velocity are close in magnitude. In terms of average velocity, while SPIV experiments were 1.21 m/s, the analysis result was 1.16 m/s with a margin of error of 4%.

It is concluded that defining constant and homogeneous boundary conditions in systems where devices with non-homogeneous flow characteristics, such as fans, pumps, etc., are used dramatically increases the margin of error in numerical studies.

The results of the study show that the SPIV experiments defined in the numerical study by data assimilation show the importance of the design of the experiment. Especially in systems involving forced flows, not including the elements that will create pressure difference in the experiment negatively affects the experimental results and provides incorrect data to the numerical analysis.

In the fan-burner system of the combi boiler examined in the thesis study, the SPIV experiments taken from the burner cover were defined as the inlet boundary condition in the numerical study by the data assimilation method, and the analyses were validated by experiments. This study is the first example in the literature to analyse the relevant region using the data assimilation method. The experimental data and analyses served as the foundation for publications in the academic literature. In these publications, our working team investigated the combustion characteristics and emission gases pertaining to the design of combi boilers (Yılmaz et al., 2024).

CHAPTER FIVE
EXPERIMENTAL AND NUMERICAL INVESTIGATION OF AIR PURIFIER SYSTEMS

The vast majority of our daily lives are spent within indoor environments, the air quality of which directly impacts both our health and our living standards throughout the day. Therefore, enhancing indoor air quality is of critical importance.

In addition to the necessity of clean air within indoor environments, the filtration of harmful particles present indoors is also crucial. These particles can range from those causing pandemics and other diseases, which can be neutralized using auxiliary technologies such as Ultraviolet (UV) technology, to particles containing odours and other adverse elements.

The need for fresh air within indoor environments is fulfilled through ventilation systems. This can range from the simple act of opening windows to the use of HVAC systems to provide the required fresh air. The purification of particles present within indoor spaces is accomplished through filters. The most commonly used High Efficiency Particulate Air (HEPA) etc. filters can clean the indoor environment by capturing particles of different sizes. For these filters to capture particles, the air containing the particles must pass through them, after which the purified air is reintroduced into the indoor environment. Devices that facilitate this cycle are referred to as air purifiers.

Air purifiers consist of an outer casing, electronic components, a filter system and a fan. The fan performs the task of sucking the air through the filter and cleaning it from particles. For this reason, the most critical and extensively studied components of air purifiers are the fan and filter systems (Figure 5.1).

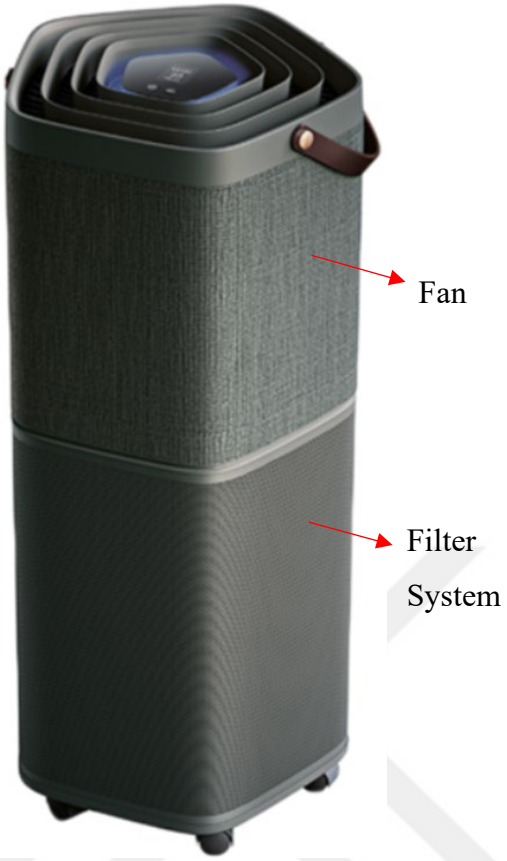


Figure 5.1 Investigated air purifier system

The studies in the literature assume that the suction side of the air purifiers from the filter area is homogeneous, as mentioned in Chapter 1.1.4. This assumes that air passes through the entire filter surface simultaneously at the same flow rate. A constant velocity assumption is used in the entire region of the blowing.

In Chapter 5.1, this situation is discussed in detail, and both suction and blowing characteristics are obtained by SPIV experiments. In Chapter 5.2, the obtained experimental data are defined to the numerical model by the data assimilation method, and a comparative analysis of the literature is presented.

5.1 Stereo Particle Image Velocimetry Experiments to Investigate Air Purifier

In air purifier systems, air is sucked through the filter by a fan, purified from particles, and then released back into the indoor environment. The fan's characteristics are crucial in determining the suction velocity due to the pressure difference. The

purified air from the fan travels through the flow duct and enters the indoor environment through the blowing nozzle. It is important to evaluate the fan and the flow channel together, and to design the channel according to the fan being used.

The results of the flow structure of the air purifier, examined as part of the thesis and with its CAD model presented in Figure 5.2, were obtained by SPIV analysis.

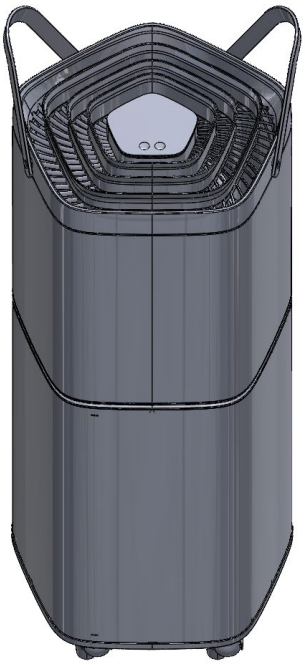


Figure 5.2 CAD geometry of investigated air purifier

The device to be examined to obtain the blowing flow structure of the Air Purifier was placed in the schematic SPIV experimental setup (Figure 5.3). The outlet section of the device was positioned perpendicular to the cameras. The reason for this is that the jet flow structure coming out of the outlet section can be examined in detail.

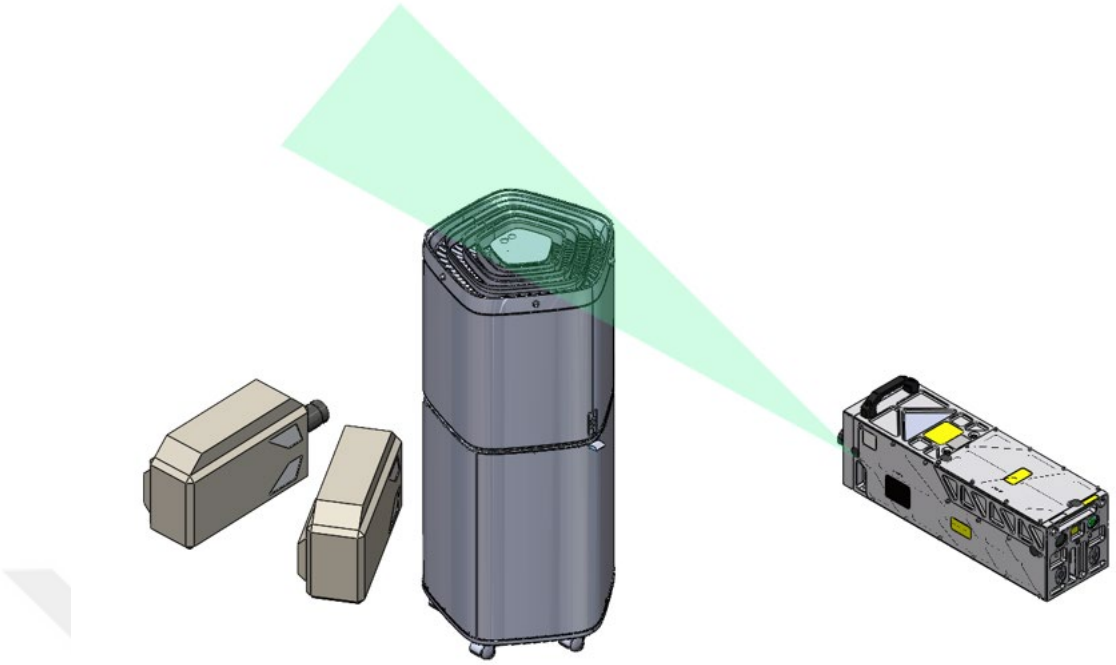


Figure 5.3 The Schematic of SPIV setup to investigate the air purifier

The outlet section of the device has a width of 320 mm. Experimental images were obtained from 11 planes at 40 mm intervals in order to visualise the added flow from environment. Examples of raw experimental images taken from the mid-plane as a result of SPIV are presented in Figure 5.4.

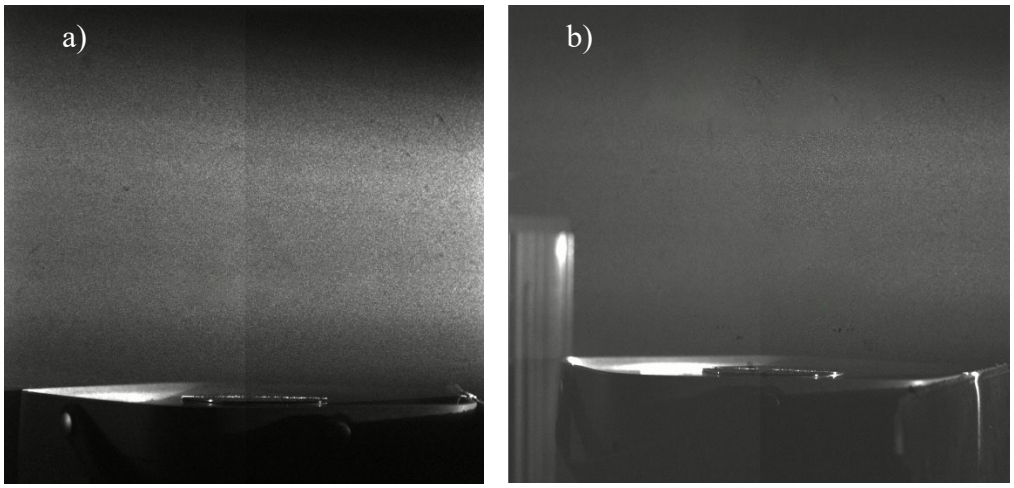


Figure 5.4 z=160 mm SPIV experiment results a) direct camera b) angular camera

The 400 image pairs (800 images) obtained during the experiment were processed by cross correlation method to obtain velocity vectors. The velocity vectors obtained for z=160 mm, which is the mid-plane of the device, are presented in Figure 5.5.

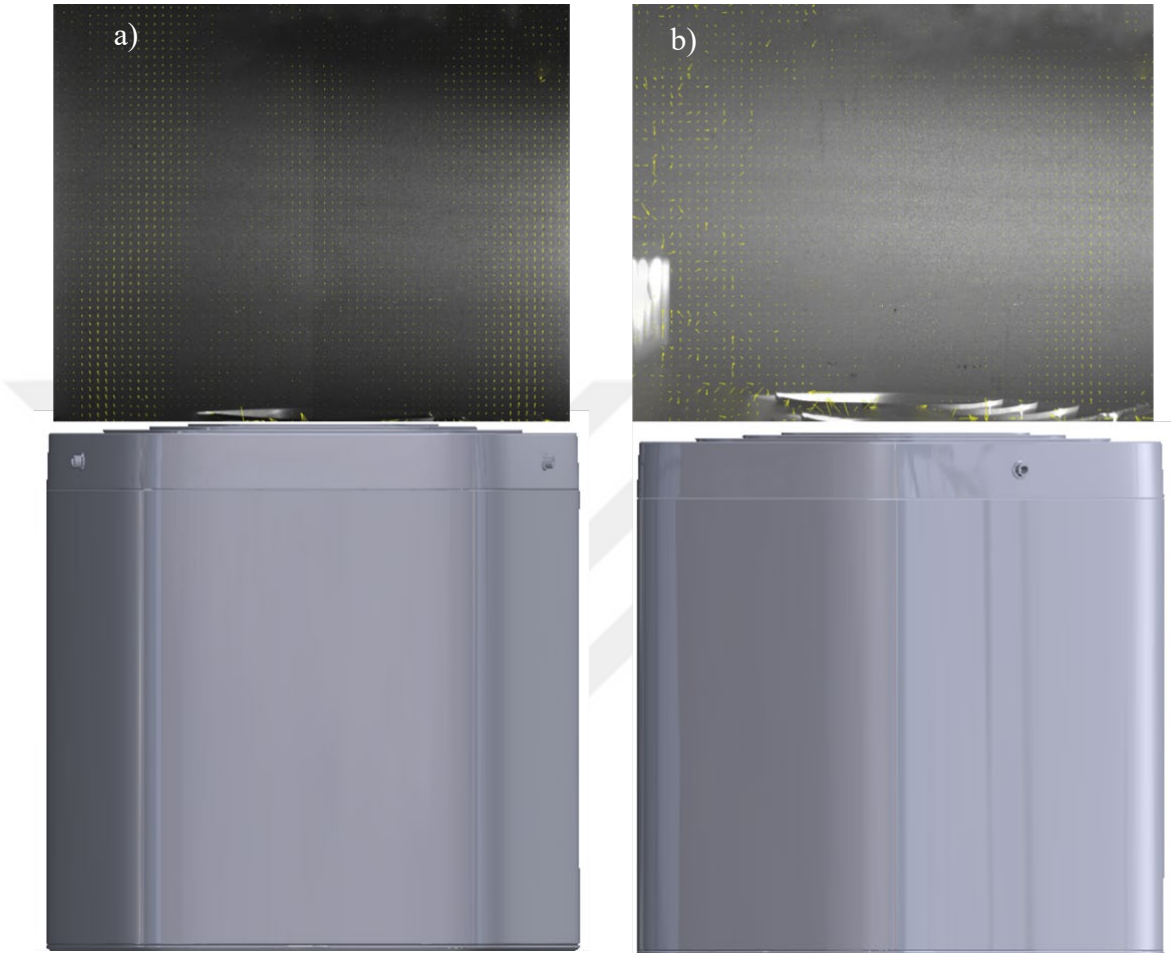


Figure 5.5 z=160 mm SPIV experiment velocity vector map a) direct camera b) angular camera

The results show that the flow has a high velocity in the region close to the walls of the flow channel. This situation shows that the filtered and purified air penetrates the room in an upward direction. However, these two-dimensional results of the flow cannot clearly present the flow effect in the third dimension. To examine the orientation of the flow at the outlet section in more detail, the device was placed parallel to the cameras. The image of the device in the schematic of SPIV experimental setup is shown in Figure 5.6.

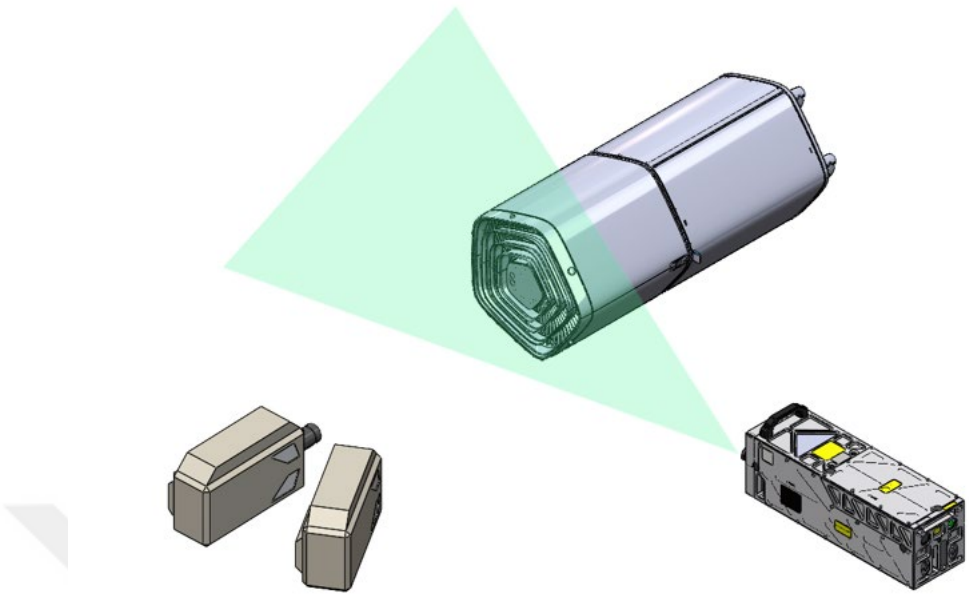


Figure 5.6 The Schematic of SPIV setup to investigate the air purifier outlet section

As shown in Figure 5.6, the flow structure was obtained by SPIV experiments. The velocity vectors of the flow structure obtained from the plane tangent to the outlet section are shown in Figure 5.7.

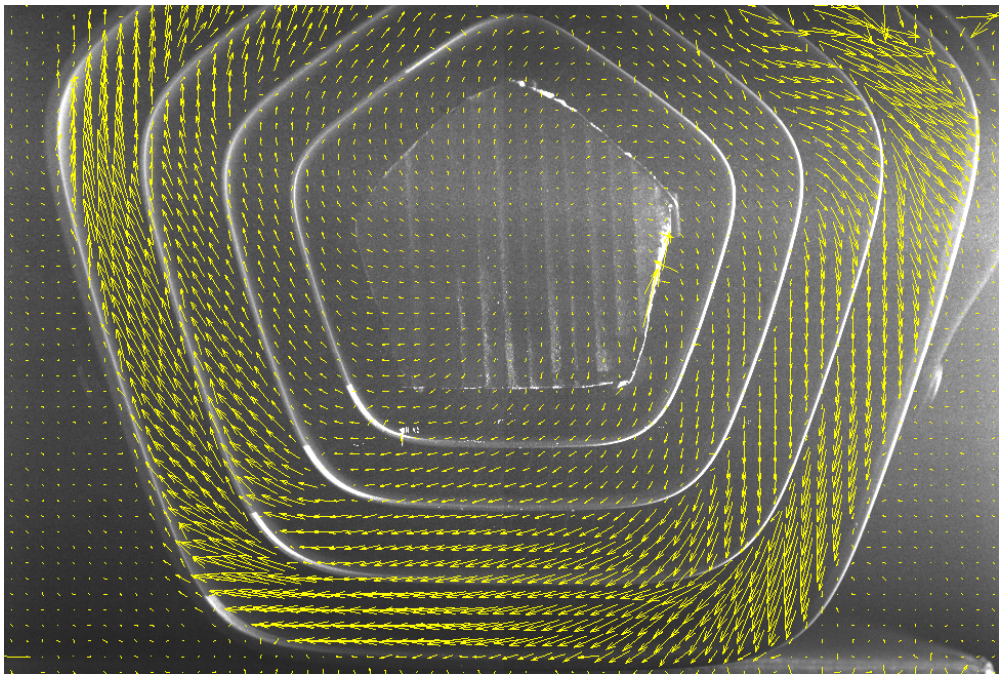


Figure 5.7 z=0 mm SPIV experiment velocity vector map

Figure 5.7 shows that the purified air blown into the room from the device penetrates the area close to the walls of the flow channel with high velocity and clockwise rotation. When Figures 5.5 and 5.7 are analysed together, it is seen that the flow follows the outer wall of the device. In addition, the effect of the crown structure at the outlet section on the flow was analysed (Figure 5.8).

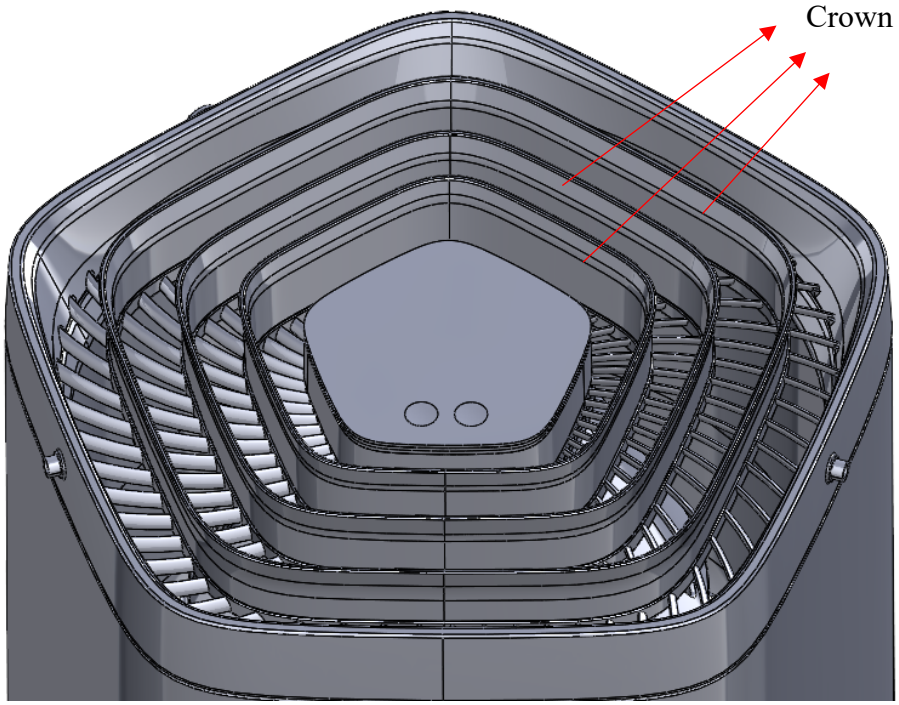


Figure 5.8 Air purifier outlet section crown

In the SPIV experiments for the Crown structure, the air purifier was placed perpendicular and parallel to the cameras. The results obtained are presented in Figure 5.9.

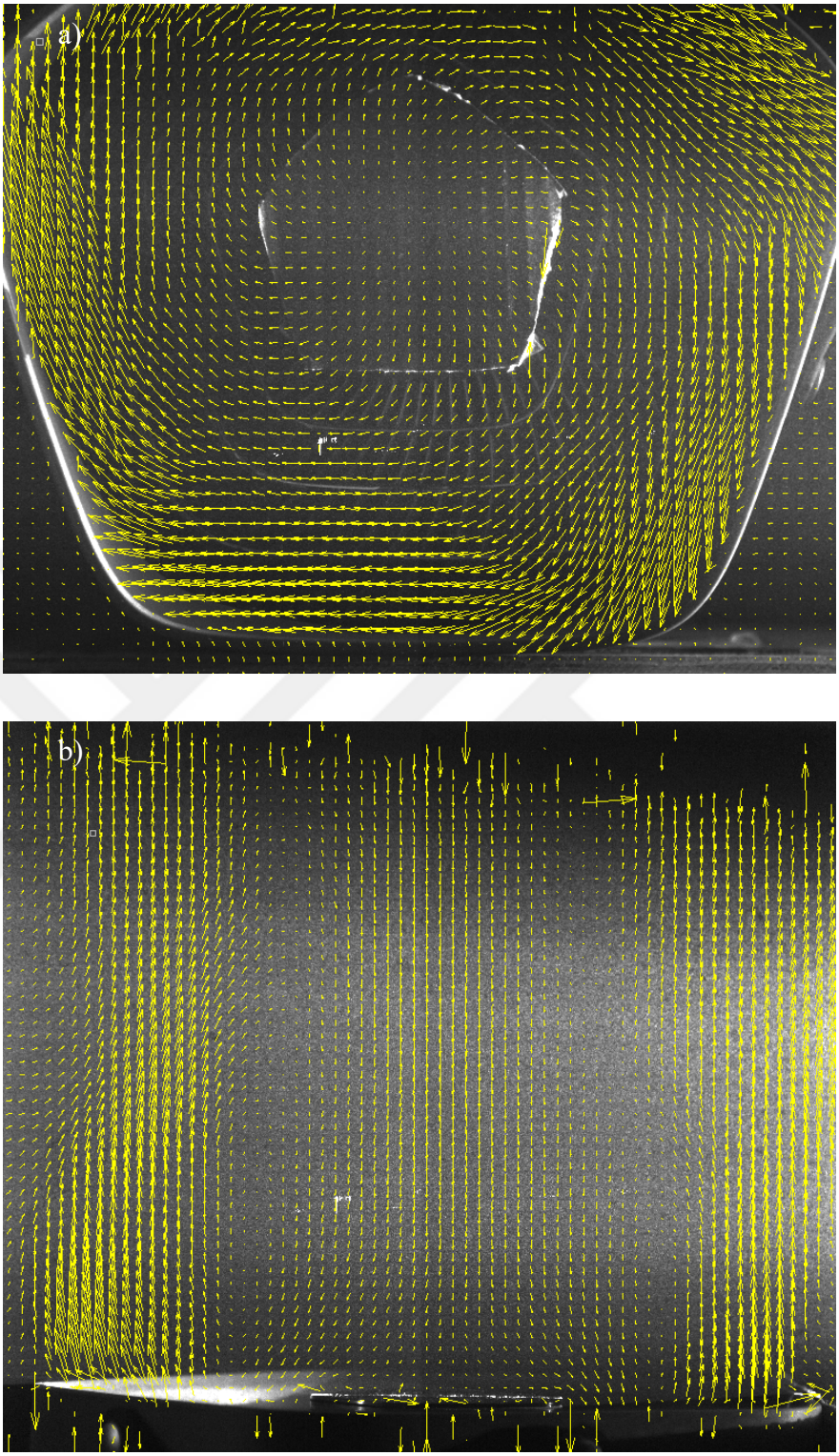


Figure 5.9 SPIV results of air purifier outlet section without crown a) z=0 from parallel angle b) z=160 (mid-plane) from direct angle

In Figure 5.9-b, the velocity profiles obtained from the outlet section where there is no crown structure show that the flow leaves the outlet opening close to the walls of

the flow channel. In Figure 5.9-a, it is seen that the flow moves clockwise and penetrates the room. For a more detailed examination, Figure 5.10 shows the SPIV results with and without crown.

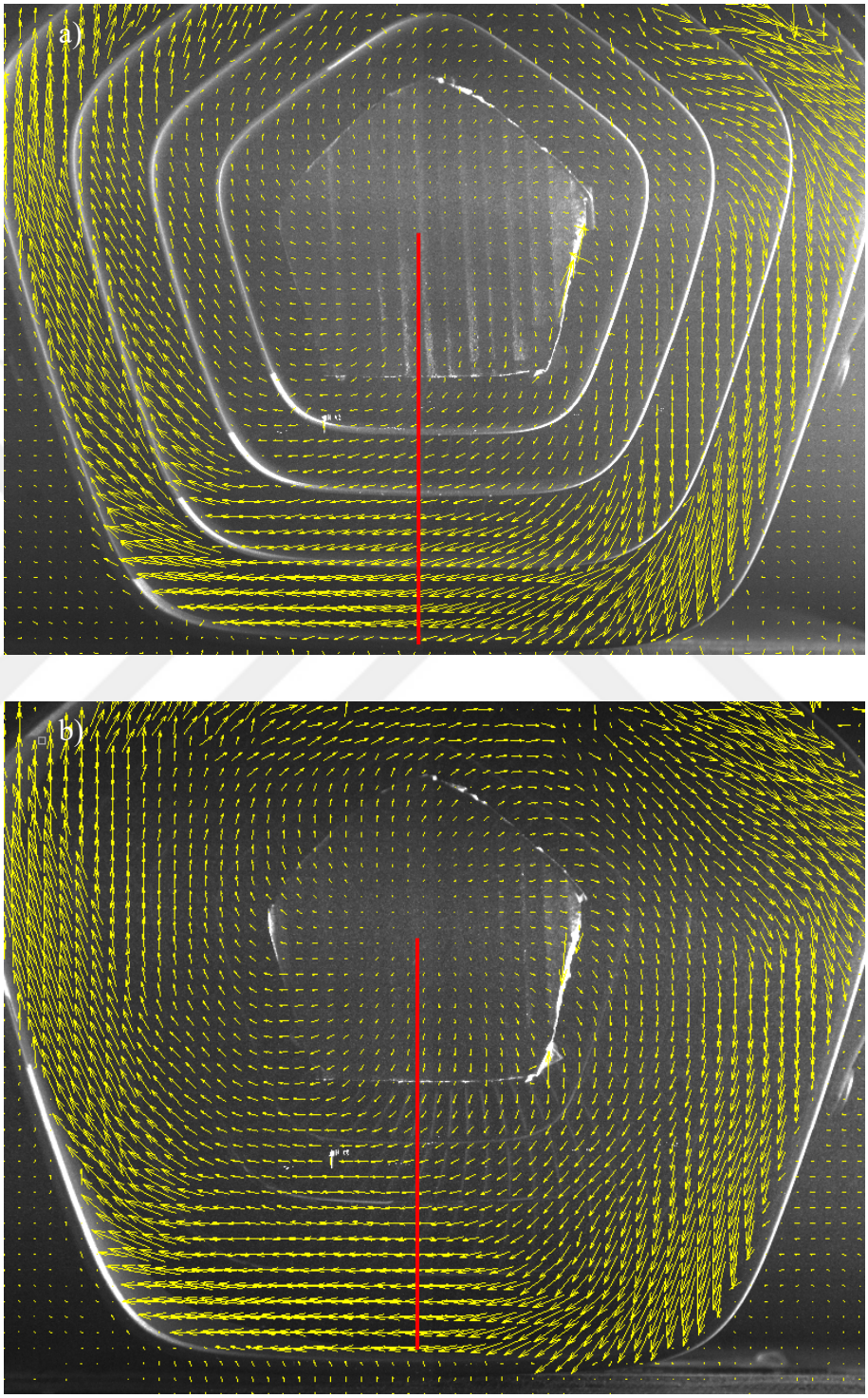


Figure 5.10 SPIV results of air purifier outlet section a) with crown b) without crown

The results of the SPIV experiments indicate that the crown's structure does not have a considerable impact on the flow structure of the device, except for the final crown position where flow acceleration is observed as a result of the narrowing effect of the crown. The narrowing effect is found to be less in the version without the crown. For a more comprehensive analysis, velocity data were obtained along the red lines shown in Figure 5.10 and are presented graphically in Figure 5.11.

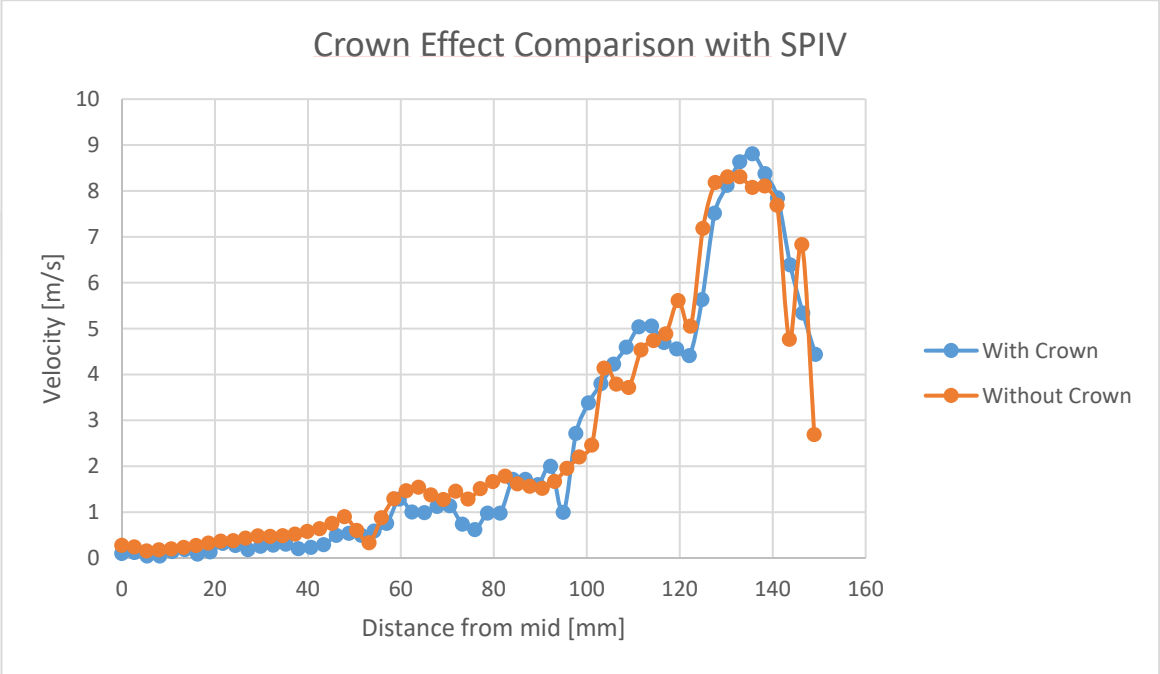


Figure 5.11 Velocity distribution of red line in Figure 5.10

The SPIV results indicate that the crown structure has no impact on the flow characteristics and velocity of the device. Moreover, at low velocities, a backflow region forms in the centre of the device. These findings are utilized in Chapter 5.2 to validate the application of numerical studies through data assimilation.

To validate the data assimilation method in the numerical model, it is imperative to acquire the input boundary condition from the SPIV experiment data. Consequently, SPIV experiments were conducted on the suction area of the Air Purifier. The 2-dimensional 3-component velocity distribution obtained from the SPIV data from the suction area of the device is illustrated in Figure 5.12.

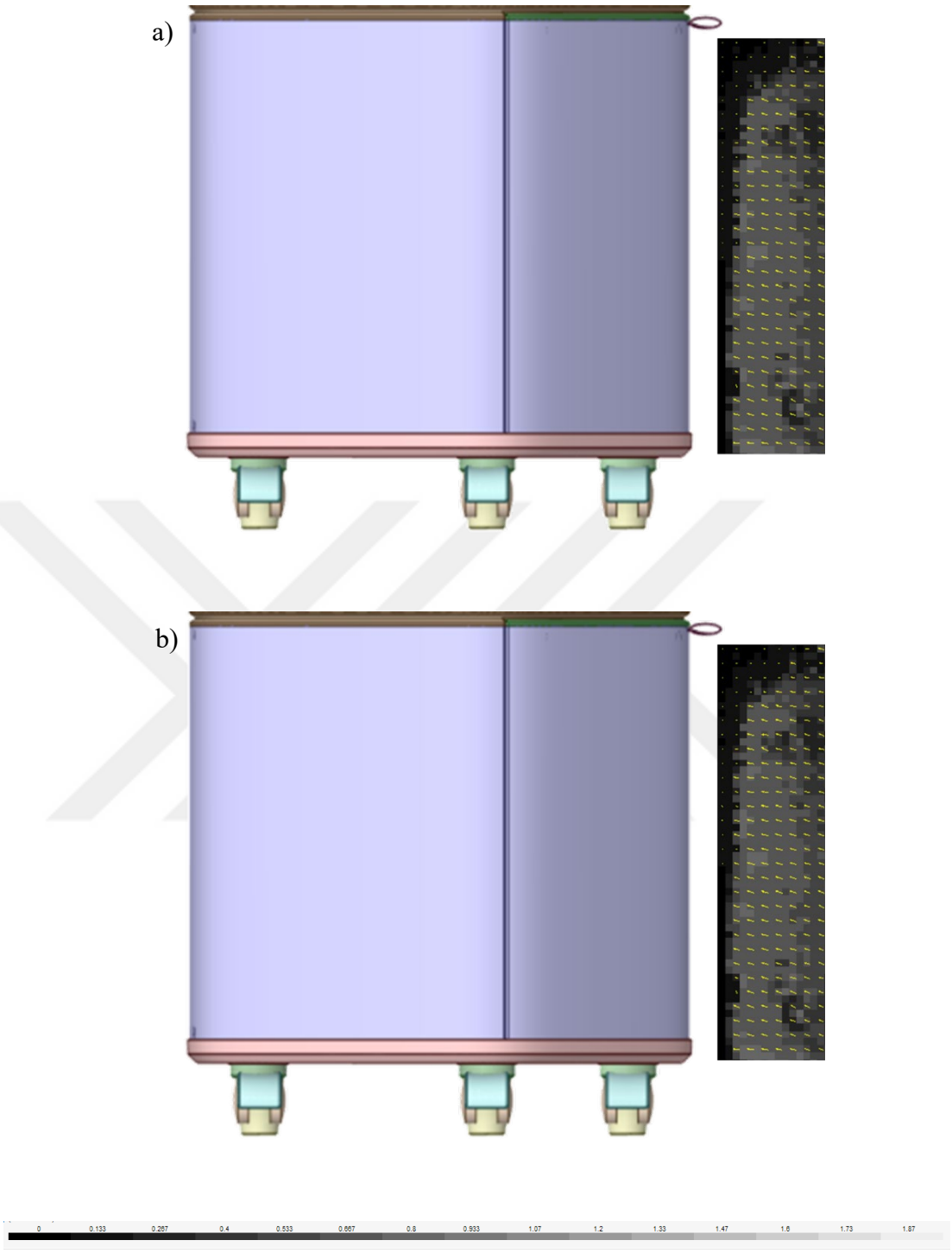


Figure 5.12 SPIV results of air purifier suction region a) with filter b) without filter

The primary factor affecting the performance of an air purifier's fan is the suction area filters. These filters are responsible for purifying the air, but they also create a pressure drop that directly impacts the fan's operation and the flow rate. Figure 5.12 illustrates how this effect influences velocity magnitudes. During SPIV experiments,

the average velocity of the suction zone with filters was measured at 0.55 m/s, whereas it increased to 1.13 m/s when the filters were removed. Both scenarios, depicted in Figure 5.12 (a and b), demonstrate a homogeneous suction across the entire surface.

The data obtained from SPIV experiments were utilized as boundary conditions for the numerical model using the data assimilation method. A comprehensive explanation of the numerical study is provided in Chapter 5.2.

5.2 Numerical Investigation of Air Purifier by Data Assimilation with Stereo Particle Image Velocimetry

In air purifiers, the flow channel, with the fan and filters, is one of the most critical parameters affecting the flow rate and, therefore, the system's performance. Due to the device's outer casing, it is challenging to investigate the flow structure in the inner region experimentally. For this reason, SPIV data obtained from the boundary conditions were defined for numerical studies using the data assimilation method, and validation was carried out.

In the numerical model presented in Figure 5.13, the air purifier is positioned in a room.

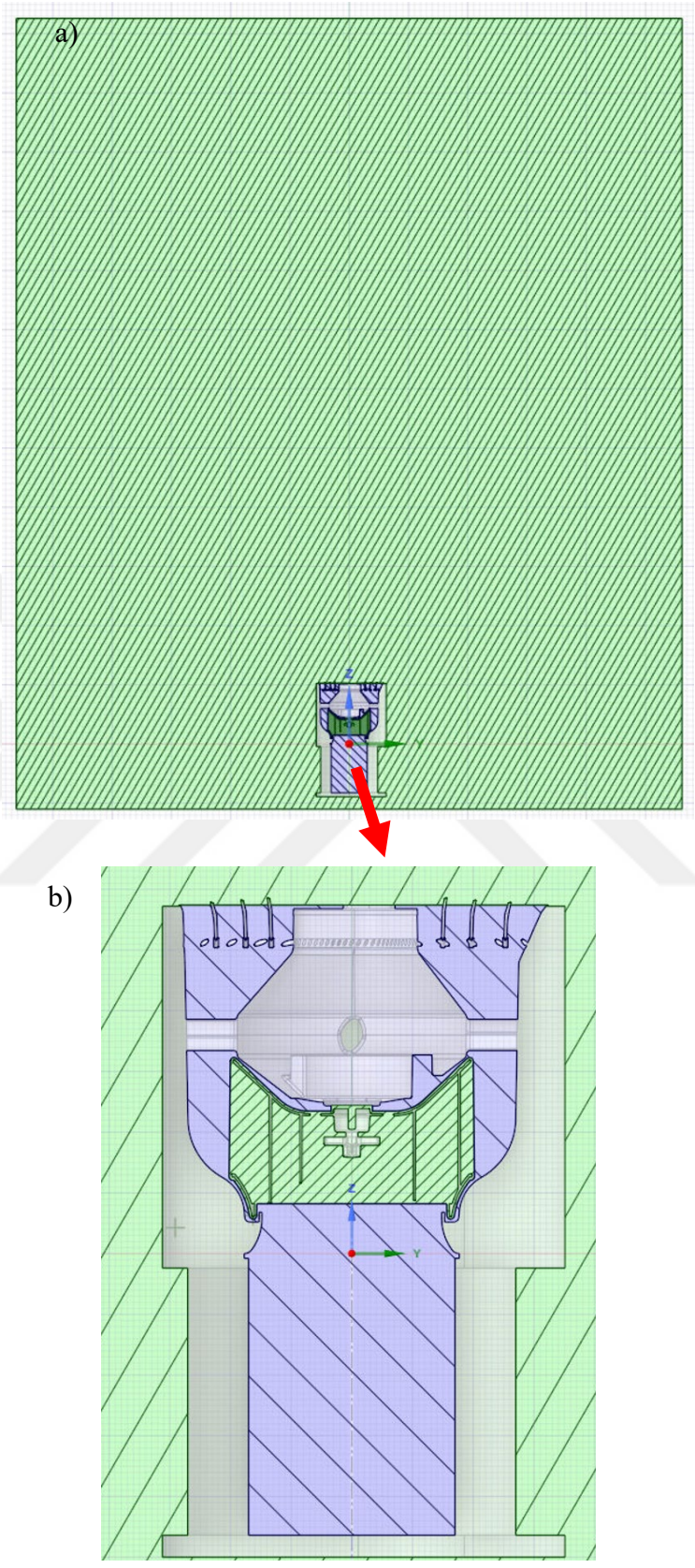


Figure 5.13 Numerical model of air purifier CFD analysis a) room and air purifier fluid domain b) air purifier fluid domain

In the numerical model, the flow volume of the air purifier is divided into three primary sections: the inner region before the fan, where the air passes through the filters to reach the fan; the fan region; and the flow channel, where the purified air is delivered into the room after passing through the fan. The rotational speed of the fan in the numerical model is 1500 rpm, and as a result, the mesh structure of the fan fluid domain is of utmost importance.

The studies conducted as part of the thesis utilized approximately 20 million mesh elements. Figure 5.14 illustrates the mesh structure of the fluid domain of the device.

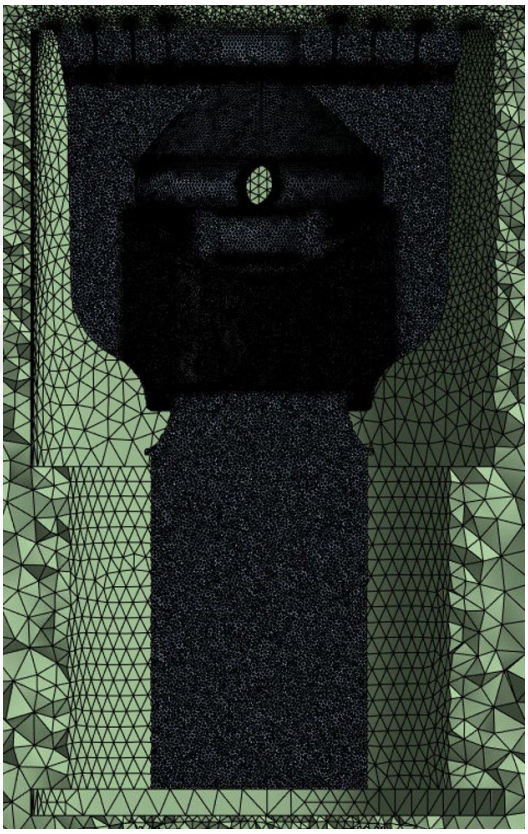


Figure 5.14 Mesh structure of air purifier fluid domain

During the numerical study, the fan is operated at a speed of 1500 rpm to draw air from the suction zone and distribute it into the room. However, when the data from the SPIV is directly applied to the suction zone and the fan is operated at the same rpm, it exhibits behavior similar to that of an additional fan connected in series. Thus, it is essential to determine the required pressure drop to correlate the velocity data obtained from the SPIV experiments. After conducting various analyses, it has been established

that a pressure drop of 45 Pa yields identical flow rates. The flow distribution for the mid-plane obtained from the analysis is illustrated in Figure 5.15.

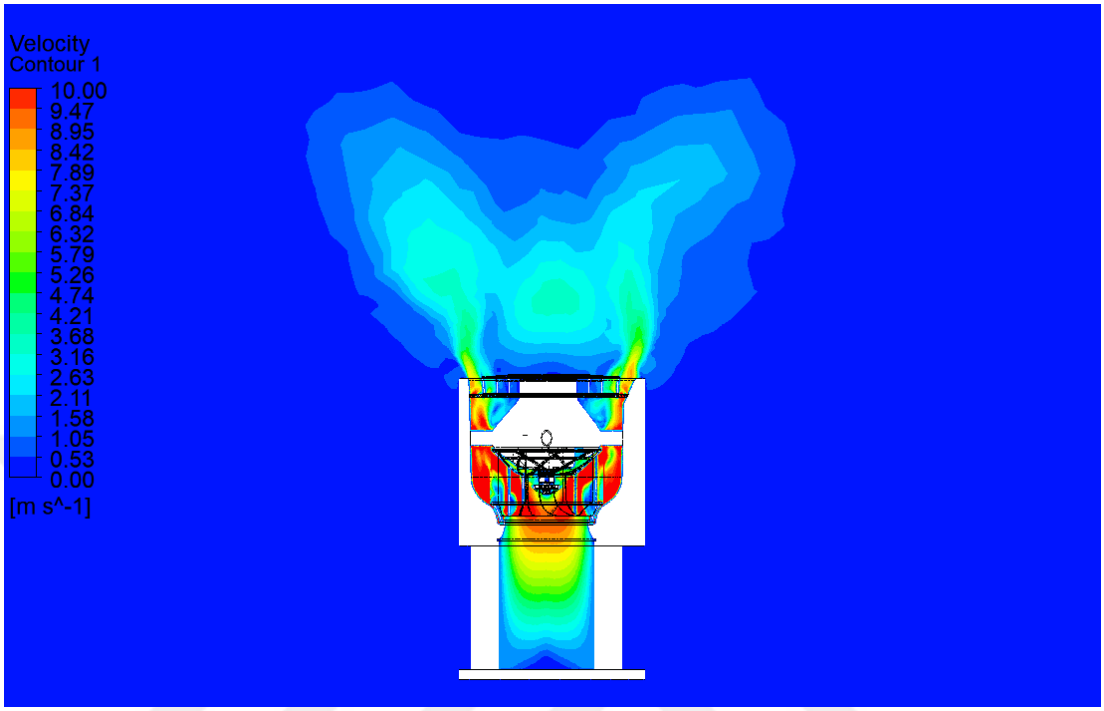
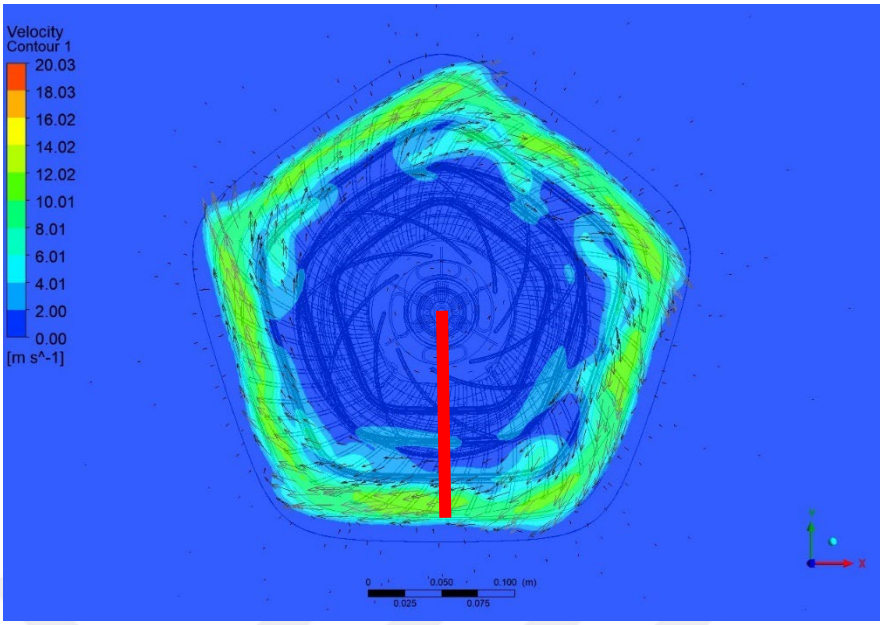


Figure 5.15 Velocity distributions of mid-plane

As a result of CFD analysis, it is seen that the fan draws air homogenously from the suction area and penetrates into the room. As a result of the analysis, the flow rate is determined to be 623 m3/h, while the catalogue and SPIV results of the device are 600 and 613 m3/h, respectively. Thanks to the data obtained from SPIV experiments, the CFD analysis result was verified with a 3.8% error margin in terms of flow rate using the data assimilation method. In addition, the velocity distribution and velocity vectors obtained from the outlet section of the air purifier were obtained for validation with SPIV and presented in Figure 5.16.

a)



b)

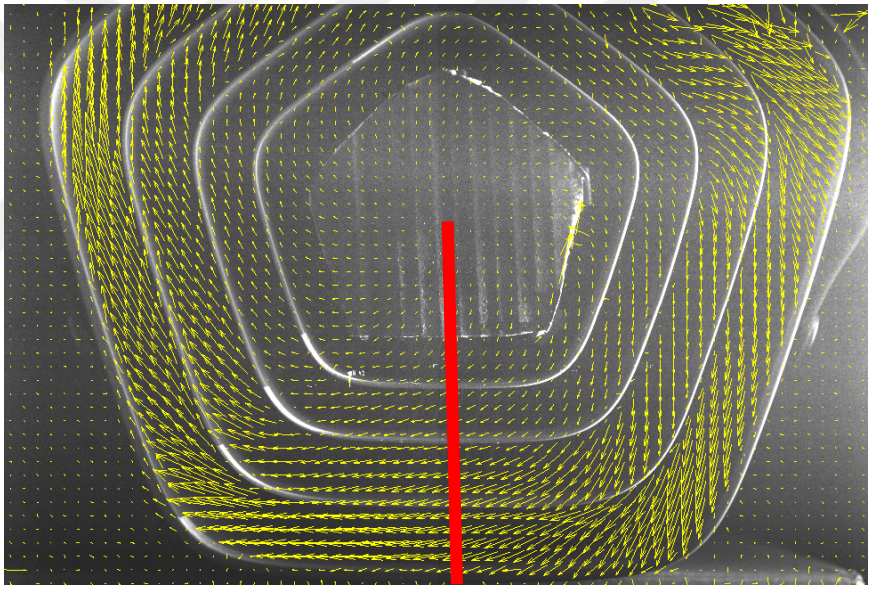


Figure 5.16 Velocity distributions of outlet section of air purifier a) CFD result b) SPIV result

In Figure 5.16, it is evident that the results from both the SPIV and CFD demonstrate a consistent flow structure. The flow moves in a clockwise direction and penetrates the room, with velocities decreasing as it nears the central regions. To facilitate comparison of velocity magnitudes, velocity data was extracted from the red lines in Figure 5.16, with the resulting comparison graph displayed in Figure 5.17.

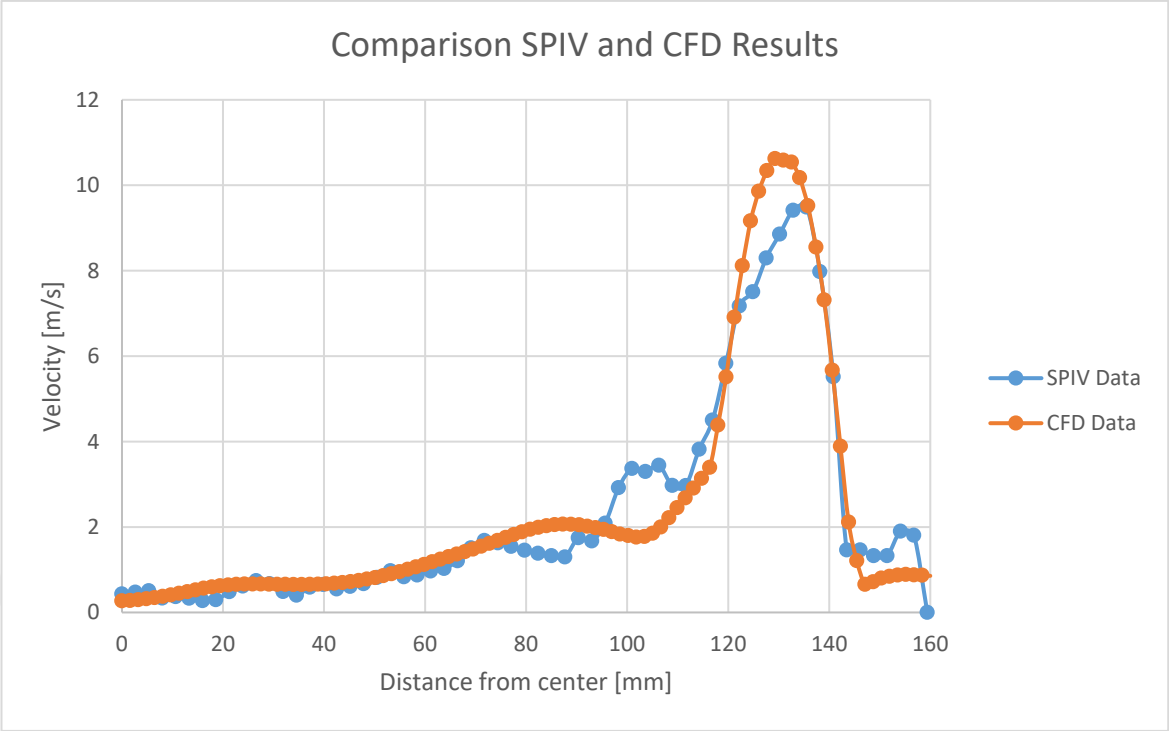


Figure 5.17 Comparison of SPIV and CFD results

In experimental and numerical analyses, it was observed that velocity remained low within approximately 80 mm from the centre. However, beyond this distance, velocities increased to up to 10 m/s due to the flow exiting the fan and moving tangentially to the flow channel wall. The average velocity obtained from this region are detailed in Table 5.1 as a result of the numerical and experimental study.

Table 5.1 Average velocity comparison of SPIV and CFD results

	SPIV	**CFD**
Average Velocity at line (m/s)	2.33	2.34
Average Velocity between 80-150 mm (m/s)	4.17	4.18

In the evaluation of average velocities, CFD analyses were conducted with a margin of error of less than 1% throughout the entire line and in the high-velocity region. The results demonstrate that the data assimilation technique enhances the accuracy of CFD analyses in simulating turbomachinery. This is the first time in the literature that a fan-driven flow is modelled with a fan using data assimilation method and thus the reliability of the numerical study is increased using SPIV data.

CHAPTER FIVE
CONCLUSIONS

In this thesis, the flow structures of SAC, combi boilers and air purifiers are analysed with SPIV and MIT and temperature and velocity data are obtained volumetrically. These data were defined as input boundary conditions for numerical studies using the data assimilation method and enabled high-fidelity analyses unlike the literature.

The effects of data assimilated boundary conditions on a numerical room model conditioned by a SAC were investigated and compared against CFD analyses with conventional homogeneous boundary conditions. The experimental volumetric velocity data used in data assimilation was obtained by scanning SPIV, and the experimental temperature distribution was measured by the MIT method. These experimental results were also used to generate average homogeneous temperature and velocity boundary conditions that were conventionally used. The CFD analyses with assimilated boundary conditions were validated by using volumetric SPIV results.

The CFD with the data assimilated boundary conditions supplied more than four times more accurate results than the CFD with conventional boundary conditions. While the CFD with data assimilated boundary conditions has an average error of 3.13% and a maximum error of 4.74% according to the experimental data, the CFD with conventional boundary conditions has an average error of 13.19% and a maximum error of 24.03% according to the experimental data.

Regarding temperature and velocity distributions, using volumetric velocity data as boundary conditions has a more substantial impact than using temperature data. However, combining both experimental data with data assimilation presents the most accurate results.

Defining a homogeneous velocity and temperature boundary condition affects not only the steady-state analyses but also the heating or cooling characteristics of the room in the time-dependent analyses. For this reason, using the volumetric

experimental data as boundary conditions in all numerical indoor air distribution studies is recommended.

The comprehensive analysis of the fan-burner system in the 24 kW boiler highlights the critical role of the burner inlet flow structure on the results of the numerical analyses and therefore on the overall performance and emission characteristics of the boiler.

The SPIV experiments revealed that the flow distribution at the burner inlet is non-homogeneous due to the centrifugal fan's inherent flow characteristics. The velocity profiles showed significant variations across the burner inlet, affecting the subsequent combustion process.

The thesis demonstrated that higher spatial resolution in SPIV experiments leads to more accurate volumetric velocity maps. The direct use of high-resolution experimental data reduced interpolation errors and provided a clearer understanding of the flow structure.

The inclusion of the burner cover in SPIV experiments significantly altered the flow structure. The pressure differences created by the cover impacted the fan's flow rate and direction, highlighting the necessity of incorporating such components in experimental setups for realistic boundary condition data.

The data assimilation method used to define inlet boundary conditions in CFD analyses proved effective in improving the accuracy of flow simulations. The comparison between homogeneous flow rate boundary conditions and those derived from experimental data underscored the importance of accurate boundary condition definitions.

The validation of the CFD results with SPIV experimental data showed that, assuming homogeneity and neglecting the burner cover effect, there are inconsistencies in the velocity distributions, especially in regions where high velocity peaks are expected. The inclusion of the burner cover effect in the CFD analyses brought the numerical results closer to the experimental observations and the error margins decreased from 24% to 4% approximately.

The detailed investigation of the flow structure in the fan-burner system of a 24 kW combi boiler using SPIV and CFD analyses highlighted the critical importance of accurate boundary condition definitions for numerical studies. The thesis demonstrated that non-homogeneous flow distributions significantly impact combustion efficiency and emission rates, underscoring the need for precise experimental data and advanced data assimilation techniques in the design and optimization of heating appliances.

The thesis has thoroughly explored the flow structure of air purifiers, emphasizing the critical role of indoor air quality on health and living standards. By integrating data assimilation techniques with SPIV experiments, a comprehensive understanding of the flow structures within these devices, highlighting several key findings.

Through detailed SPIV experiments, it was found that the air flow through the filter surface is homogeneous and constant across the filter surface. This insight is crucial for optimising the design and performance of air purifiers.

The SPIV experiments demonstrated that the flow structure within air purifiers is significantly influenced by the design of the fan and the flow channel. The SPIV experiments showed that the purified air follows the outer wall of the device with a high velocity and a clockwise rotational pattern. Furthermore, our analysis indicated that the crown structure at the outlet section has a minimal impact on the overall flow characteristics, except for a slight acceleration due to the narrowing effect.

In addition to experimental analysis, data assimilation method were used to integrate SPIV data into numerical models. This approach allowed us to validate our experimental findings and provided a more detailed understanding of the flow dynamics within air purifiers. The numerical simulations, conducted with a high-fidelity, confirmed that the fan effectively homogenizes the suction area and distributes purified air into the room.

The thesis also addressed the practical implications of these findings. By demonstrating the impact of filter presence on suction velocity and the overall flow rate, provided valuable insights for the design and optimization of air purifiers. The

validated numerical model, which accurately represented the flow rate and velocity distribution with minimal error margins (approx. 1%), serves as a reliable tool for future research and development in this field.

In conclusion, the data assimilation method utilizing volumetric optical flow diagnostics has a significant potential for more realistic and accurate CFD analyses. The integration of volumetric optical flow diagnostics such as SPIV, MIT with numerical simulations through data assimilation methods represents a novel contribution to the literature, enhancing the reliability of CFD analyses. These findings not only contribute to academic knowledge but also offer practical solutions for enhancing industrial applications such as the designer and the engineers to understand flow structure of household devices.

REFERENCES

Adrian, R. J. (2005). Twenty years of particle image velocimetry. *Experiments in Fluids*, *39*(2), 159–169. https://doi.org/10.1007/s00348-005-0991-7

Anderson, R., Hassani, V., Kirkpartrick, A., Knappmiller, K., & Hittle, D. (1991). Visualizing the air flow from cold air ceiling jets. *ASHRAE Journal*, *33*(5), 30–35. http://cat.inist.fr/?aModele=afficheN&cpsidt=5390337

Andersson, H., Cehlin, M., & Moshfegh, B. (2022). A Numerical and Experimental Investigation of a Confluent Jets Ventilation Supply Device in a Conference Room. *Energies*, *15*(5). https://doi.org/10.3390/en15051630

ANSYS Inc. (2011). *ANSYS CFX-Solver Theory Guide*.

Arlit, M., Partmann, C., Schleicher, E., Schuster, C., Hurtado, A., & Hampel, U. (2018). Instrumentation for experiments on a fuel element mock-up for the study of thermal hydraulics for loss of cooling or coolant scenarios in spent fuel pools. *Nuclear Engineering and Design*, *336*, 105–111. https://doi.org/10.1016/j.nucengdes.2017.06.034

Association of European Heating Industry. Heating market report. (2024). *Association of European Heating Industry. Heating market report*. https://ehi.eu/h eating-market-report/heating-market-report-2021/

Awbi, H. B. (1989). Application of computational fluid dynamics in room ventilation. *Building and Environment*, *24*(1), 73–84. https://doi.org/10.1016/0360-1323(89)90018-8

Ben Amara, S., Laguerre, O., Charrier-Mojtabi, M. C., Lartigue, B., & Flick, D. (2008). PIV measurement of the flow field in a domestic refrigerator model: Comparison with 3D simulations. *International Journal of Refrigeration*, *31*(8), 1328–1340. https://doi.org/10.1016/j.ijrefrig.2008.04.005

Blocken, B. (2018). LES over RANS in building simulation for outdoor and indoor applications: A foregone conclusion? In *Building Simulation* (Vol. 11, Issue 5, pp. 821–870). Tsinghua University Press. https://doi.org/10.1007/s12273-018-0459-3

Brohus, H. (1997). *Defended publicly at Aalborg University*. www.civil.auc/i6/klima

Bruchhausen, M., Guillard, F., & Lemoine, F. (2005). Instantaneous measurement of two-dimensional temperature distributions by means of two-color planar laser induced fluorescence (PLIF). *Experiments in Fluids*, *38*(1), 123–131. https://doi.org/10.1007/s00348-004-0911-2

Bulińska, A., & Buliński, Z. (2015). A CFD analysis of different human breathing models and its influence on spatial distribution of indoor air parameters. *Computer Assisted Methods in Engineering and Science*, *22*, 213–227.

Burch, S. D., Hassani, V., & Penney, T. F. L. (1992). *Use of Infra-Red Thermography for Automotive Climate Control Analysis*.

Calm, J. M. (2008). The next generation of refrigerants - Historical review, considerations, and outlook. In *International Journal of Refrigeration* (Vol. 31, Issue 7, pp. 1123–1133). https://doi.org/10.1016/j.ijrefrig.2008.01.013

Čantrak, Đ. S., & Janković, N. Z. (2022). High speed stereoscopic PIV investigation of the statistical characteristics of the axially restricted turbulent swirl flow behind the axial fan in pipe. *Advances in Mechanical Engineering*, *14*(11). https://doi.org/10.1177/16878132221130563

Cao, G., Sivukari, M., Kurnitski, J., Ruponen, M., & Seppänen, O. (2010). Particle Image Velocimetry (PIV) application in the measurement of indoor air distribution by an active chilled beam. *Building and Environment*, *45*(9), 1932–1940. https://doi.org/10.1016/j.buildenv.2009.11.020

Cao, X., Liu, J., Jiang, N., & Chen, Q. (2014). Particle image velocimetry measurement of indoor airflow field: A review of the technologies and applications. *Energy and Buildings*, *69*, 367–380. https://doi.org/10.1016/j.enbuild.2013.11.012

Cehlin, M., Moshfegh, B., & Sandberg, M. (2002). Measurements of air temperatures close to a low-velocity diffuser in displacement ventilation using an infrared camera. *Energy and Buildings*, *34*(7), 687–698. https://doi.org/10.1016/S0378-7788(01)00133-5

Chen, K., Tan, Z., Zhou, H., & Tan, Y. (2023). Optimization of Operations of Air Purifiers for Control of Indoor PM2.5 Using BIM and CFD. *Buildings*, *13*(1). https://doi.org/10.3390/buildings13010077

Chen, W., Li, J., Wang, C., Dai, X., & Liu, J. (2018). 2D-PIV measurement of range hood-driven flow in a domestic kitchen. *Energy and Buildings*, *177*, 64–76. https://doi.org/10.1016/j.enbuild.2018.07.051

Chow, W. K. (1996). Application of Computational Fluid Dynamics in building services engineering. *Building and Environment*, *31*(5), 425–436. https://doi.org/10.1016/0360-1323(96)00012-1

Dabiri, D. (2009). Digital particle image thermometry/velocimetry: A review. *Experiments in Fluids*, *46*(2), 191–241. https://doi.org/10.1007/s00348-008-0590-5

Dbouk, T., Roger, F., & Drikakis, D. (2021). Reducing indoor virus transmission using air purifiers. *Physics of Fluids*, *33*(10). https://doi.org/10.1063/5.0064115

De Baar, J. H. S., Percin, M., Dwight, R. P., Van Oudheusden, B. W., & Bijl, H. (2014). Kriging regression of PIV data using a local error estimate. *Experiments in Fluids*, *55*(1). https://doi.org/10.1007/s00348-013-1650-z

De Cachinho Cordeiro, I. M., Liu, H., Yuen, A. C. Y., Chen, T. B. Y., Li, A., & Yeoh, G. H. (2023). Numerical assessment of LES subgrid-scale turbulence models for expandable particles in fire suppression. *Experimental and Computational Multiphase Flow*, *5*(1), 99–110. https://doi.org/10.1007/s42757-021-0112-8

Dreizler, A., Pitsch, H., Scherer, V., Schulz, C., & Janicka, J. (2021). The role of combustion science and technology in low and zero impact energy transformation processes. *Applications in Energy and Combustion Science*, *7*. https://doi.org/10.1016/j.jaecs.2021.100040

Einecke, S., Schulz, C., & Sick, V. (2000). Measurement of temperature, fuel concentration and equivalence ratio fields using tracer LIF in IC engine

combustion. *Applied Physics B: Lasers and Optics*, *71*(5), 717–723. https://doi.org/10.1007/s003400000383

Elvsen, P. A., & Sandberg, M. (2009). Buoyant jet in a ventilated room: Velocity field, temperature field and airflow patterns analysed with three different whole-field methods. *Building and Environment*, *44*(1), 137–145. https://doi.org/10.1016/j.buildenv.2008.02.009

Energy Agency, I. (2021). *Global Energy Review: CO2 Emissions in 2021 Global emissions rebound sharply to highest ever level*. www.iea.org/t&c/*Estimates of World Air Conditioner Demand The Japan Refrigeration and Air Conditioning Industry Association*. (2022).

Eurostat. (2024). *Energy consumption in households*. https://ec.europa.eu/eurostat/statistics-explained/index.php?title=Energy_consumption_in_households

Fanger, P. O. (1973). Assessment of man's thermal comfort in practice. In *British Journal of Industrial Medicine* (Vol. 30, Issue 4, pp. 313–324). https://doi.org/10.1136/oem.30.4.313

Gharib, M., Kremers, D., Koochesfahani, M. M., & Kemp, M. (2002). Leonardo ' s vision of flow visualization. *Experiments in Fluids*, *33*(1), 219–223. https://doi.org/10.1007/s00348-002-0478-8

Hak, M. G. (2000). *Flow Control*.

Hinrichs, J., Felsmann, D., Schweitzer-De Bortoli, S., Tomczak, H. J., & Pitsch, H. (2018). Numerical and experimental investigation of pollutant formation and emissions in a full-scale cylindrical heating unit of a condensing gas boiler. *Applied Energy*, *229*, 977–989. https://doi.org/10.1016/j.apenergy.2018.08.011

Hirasawa, K., Kojima, H., & Tomimura, T. (2015). Proposal of simple measurement method for peak detection capability of microscopic area by infrared thermograph. *Transactions of the Japan Institute of Electronics Packaging*, *8–1*.

Incropera, F. P., DeWitt, D. P., Bergman, T. L., & Lavine, A. S. (2007). Fundamentals of Heat and Mass Transfer. In F. P. Incropera & F. P. F. O. H. A. M. T. Incropera (Eds.), *Water* (Vol. 6th). John Wiley & Sons. https://doi.org/10.1016/j.applthermaleng.2011.03.022

Jacobson, R. (1978). *The Manual of photography: Formerly the Ilford manual of photography* (Seventh Edition). Focal Press.

Jones, P. J., & Whittle, G. E. (1992). Computational fluid dynamics for building air flow prediction—current status and capabilities. *Building and Environment*, *27*(3), 321–338. https://doi.org/10.1016/0360-1323(92)90033-L

Karadeniz, Z. H., Kumlutaş, D., & Özer, Ö. (2013). Experimental visualization of the flow characteristics of the outflow of a split air conditioner indoor unit by meshed infrared thermography and stereo particle image velocimetry. *Experimental Thermal and Fluid Science*, *44*, 334–344. https://doi.org/10.1016/j.expthermflusci.2012.07.005

Keller, J., Blanco, E., Barrio, R., & Parrondo, J. (2014). PIV measurements of the unsteady flow structures in a volute centrifugal pump at a high flow rate. *Experiments in Fluids*, *55*(10). https://doi.org/10.1007/s00348-014-1820-7

Kelm, S., Ritterath, M., Prasser, H. M., & Allelein, H. J. (2016). Application of the MiniPanda test case “erosion of a stratified layer by a vertical jet” for CFD validation. *Nuclear Engineering and Design*, *299*, 124–135. https://doi.org/10.1016/j.nucengdes.2015.08.013

Kim, J. S., Jeong, U. C., Kim, D. W., Han, S. Y., & Oh, J. E. (2015). Optimization of sirocco fan blade to reduce noise of air purifier using a metamodel and evolutionary algorithm. *Applied Acoustics*, *89*, 254–266. https://doi.org/10.1016/j.apacoust.2014.10.005

Kline, S. J., Reynolds, W. C., Schraub, F. A., & Runstadler, P. W. (1967). The structure of turbulent boundary layers. *Journal of Fluid Mechanics*, *30*(4), 741–773. https://doi.org/10.1017/S0022112067001740

Kumlutaş, D., Karadeniz, Z. H., & Kuru, F. (2013). Investigation of flow and heat transfer for a split air conditioner indoor unit. *Applied Thermal Engineering*, *51*(1–2), 262–272. https://doi.org/10.1016/j.applthermaleng.2012.08.051

Lee, B., Sim, W., Jo, J., & Chung, J. (2020). Reduction of flow-induced noise in a household air purifier. *Journal of Mechanical Science and Technology*, *34*(8), 3105–3115. https://doi.org/10.1007/s12206-020-0701-7

Legrand, M., Nogueira, J., Lecuona, A., Nauri, S., & Rodríguez, P. A. (2010). Atmospheric low swirl burner flow characterization with stereo PIV. *Experiments in Fluids*, *48*(5), 901–913. https://doi.org/10.1007/s00348-009-0775-6

Liu, Z., Yu, Z., Chen, X., Cao, R., & Zhu, F. (2020). An investigation on external airflow around low-rise building with various roof types: PIV measurements and LES simulations. *Building and Environment*, *169*. https://doi.org/10.1016/j.buildenv.2019.106583

Lomperski, S., Gerardi, C., & Pointer, W. D. (2015). Fiber optic distributed temperature sensor mapping of a jet-mixing flow field. *Experiments in Fluids*, *56*(3), 1–16. https://doi.org/10.1007/s00348-015-1918-6

Ma, S., Liu, W., Dong, J., Liu, J., & Wang, Z. (2022). Indoor thermal environment in a rural dwelling heated by air-source heat pump air-conditioner. *Sustainable Energy Technologies and Assessments*, *51*. https://doi.org/10.1016/j.seta.2021.101948

Meraner, C., Li, T., Ditaranto, M., & Løvås, T. (2018). Cold flow characteristics of a novel bluff body hydrogen burner. *International Journal of Hydrogen Energy*, *43*(14), 7155–7168. https://doi.org/10.1016/j.ijhydene.2018.02.062

Meslem, A., Nastase, I., & Allard, F. (2010). Passive mixing control for innovative air diffusion terminal devices for buildings. *Building and Environment*, *45*(12), 2679–2688. https://doi.org/10.1016/j.buildenv.2010.05.028

Miles, R., & Lempert, W. (1990). Two-dimensional measurement of density, velocity, and temperature in turbulent high-speed air flows by UV rayleigh scattering.

Applied Physics B Photophysics and Laser Chemistry, *51*(1), 1–7. https://doi.org/10.1007/BF00332317

Minkina, Waldemar., & Dudzik, S. (2009). *Infrared thermography : errors and uncertainties*. J. Wiley.

Nero, A. V. (1988). Controlling Indoor Air Pollution. *Source: Scientific American*, *258*(5), 42–49. https://doi.org/10.2307/24989085

Nielsen, P. V. (1974). *Flow in air conditioned rooms: Model experiments and numerical solution of the flow equations*.

Nielsen, P. V. (2015). Fifty years of CFD for room air distribution. *Building and Environment*, *91*, 78–90. https://doi.org/10.1016/j.buildenv.2015.02.035

Non-ducted air conditioners and heat pumps-Testing and rating for performance: ISO 5151. (2017). www.iso.org

Özer, Ö. (2017). *Graduate school of natural and applied sciences investigation of fan driven flow fields by particle image velocimetry and infrared thermography*. Dokuz Eylül University

Özer, Ö., & Kumlutaş, D. (2017). Experimental investigation on cross flow fan's casing parameters inside of a split air conditioner indoor unit by Stereo Particle Image Velocimetry. *Applied Thermal Engineering*, *124*, 1233–1246. https://doi.org/10.1016/j.applthermaleng.2017.06.053

Özer, Ö., Kumlutaş, D., & Yücekaya, U. A. (2017). Üç Boyutlu Arka Plan Konumlandırılmış Yoğunluk Farkı (Schlieren) Yöntemi ile Akış Yapılarının İncelenmesi ve Parçacık Görüntülemeli Hız Ölçümü ile Doğrulanması. *Engineer and Machinery* (Vol. 58).

Özer, Ö., Kumlutaş, D., & Yücekaya, U. A. (2019). A method for volumetric visualization of temperature distribution: three-dimensional meshed infrared thermography. *Experiments in Fluids*, *60*(4). https://doi.org/10.1007/s00348-019-2704-7

Posner, J. D., Buchanan, C. R., & Dunn-Rankin, D. (2003). Measurement and prediction of indoor air flow in a model room. *Energy and Buildings* , *35*, 515–526.

Purimetla, A., & Cui, J. (2009). CFD studies on burner secondary airflow. *Applied Mathematical Modelling*, *33*(2), 1126–1140. https://doi.org/10.1016/j.apm.2008.01.007

Raffel, M., Willert, C. E., Wereley, S. T., & Kompenhans, J. (2007). Particle Image Velocimetry. In *Current Science* (Vol. 79, Issue 1). https://doi.org/10.1007/978-3-540-72308-0

Reynolds, O. (1883). An Experimental Investigation of the Circumstances which determine whether the Motion of Water shall he Direct or Sinuous, and of the Law of Resistance in Parallel Channels. *Philos Trans R Soc London.*, *174*, 935–982.

Ritterath, M., Öztürk, O. C., & Prasser, H. M. (2011). Thermo-resistive mesh sensors (TMS) for temperature field measurements. *Flow Measurement and Instrumentation*, *22*(4), 343–349. https://doi.org/10.1016/j.flowmeasinst.2011.04.007

Sakakibara, J., & Adrian, R. J. (1999). Whole field measurement of temperature in water using two-color laser induced fluorescence. In *Experiments in Fluids* (Vol. 26). Springer-Verlag.

Schäfer, T., Schubert, M., & Hampel, U. (2013). Temperature grid sensor for the measurement of spatial temperature distributions at object surfaces. *Sensors (Switzerland)*, *13*(2), 1593–1602. https://doi.org/10.3390/s130201593

Serra, N. (2023). Revisiting RANS turbulence modelling used in built-environment CFD simulations. *Building and Environment*, *237*. https://doi.org/10.1016/j.buildenv.2023.110333

Shinomori, K., Katou, K., Shimokuri, D., & Ishizuka, S. (2011). NOx emission characteristics and aerodynamic structure of a self-recirculation type burner for

small boilers. *Proceedings of the Combustion Institute*, *33*(2), 2735–2742. https://doi.org/10.1016/j.proci.2010.06.093

Smits, A. J., & Lim, , T. T. (2012). *Flow Visualization Techniques and Examples Second Edition* (Second Edition). Imperial College Press.

Staveckis, A., & Borodinecs, A. (2021). Impact of impinging jet ventilation on thermal comfort and indoor air quality in office buildings. *Energy and Buildings*, *235*. https://doi.org/10.1016/j.enbuild.2021.110738

Sun, Y., & Zhang, Y. (2007). An overview of room air motion measurement: Technology and application. *HVAC and R Research*, *13*(6), 929–950. https://doi.org/10.1080/10789669.2007.10391463

Vinnichenko, N., Plaksina, Y., Yakimchuk, O., Soldatenkova, K., & Uvarov, A. (2017). Air flow temperature measurements using infrared thermography. *Quantitative InfraRed Thermography Journal*, *14*(1), 107–121. https://doi.org/10.1080/17686733.2016.1258149

Wang, L., Li, G., Gao, J., Fang, X., Wang, C., & Xiong, C. (2023). Case Study: Impacts of Air-Conditioner Air Supply Strategy on Thermal Environment and Energy Consumption in Offices Using BES–CFD Co-Simulation. *Sensors*, *23*(13), 5958. https://doi.org/10.3390/s23135958

Wargocki, P. (1998). *Human Perception, Productivty and Symptoms Related to Indoor Air Quality*.

Wu, W., Wang, B., Malkawi, A., Yoon, N., Sehovic, Z., & Yan, B. (2018). A method toward real-time CFD modeling for natural ventilation. *Fluids*, *3*(4). https://doi.org/10.3390/fluids3040101

Xu, S., Zhang, G., Liu, X., & Li, X. (2023). CFD modelling of infection control in indoor environments: A focus on room-level air recirculation systems. *Energy and Buildings*, *288*. https://doi.org/10.1016/j.enbuild.2023.113033

Yao, Y., Yang, K., Huang, M., & Wang, L. (2013). A state-space model for dynamic response of indoor air temperature and humidity. *Building and Environment*, *64*, 26–37. https://doi.org/10.1016/j.buildenv.2013.03.009

Yılmaz, S., Kumlutaş, D., Özer, Ö., Yücekaya, U. A., Avcı, H., & Cumbul, A. Y. (2024). Parametric investigation of premixed gas inlet conditions effects on flow and combustion characteristics. *Applied Energy*, *353*. https://doi.org/10.1016/j.apenergy.2023.121999

Yücekaya, U. A., Kumlutaş, D., & Özer, Ö. (2023). The data assimilation of volumetric velocity and temperature data to extract boundary conditions for high-fidelity simulation of the indoor air. *Energy and Buildings*, *300*. https://doi.org/10.1016/j.enbuild.2023.113647

Zhai, Z. (2006). Application of computational fluid dynamics in building design: Aspects and trends. In *Indoor and Built Environment* (Vol. 15, Issue 4, pp. 305–313). https://doi.org/10.1177/1420326X06067336

Zhang, F., & Ryu, Y. (2021). Simulation study on indoor air distribution and indoor humidity distribution of three ventilation patterns using computational fluid dynamics. *Sustainability (Switzerland)*, *13*(7). https://doi.org/10.3390/su13073630

Zhang, T. H., Liu, F. G., & You, X. Y. (2014). Optimization of gas mixing system of premixed burner based on CFD analysis. *Energy Conversion and Management*, *85*, 131–139. https://doi.org/10.1016/j.enconman.2014.05.055

Zhang, X., Weerasuriya, A. U., & Tse, K. T. (2020). CFD simulation of natural ventilation of a generic building in various incident wind directions: Comparison of turbulence modelling, evaluation methods, and ventilation mechanisms. *Energy and Buildings*, *229*. https://doi.org/10.1016/j.enbuild.2020.110516

Zhao, D. F., Liu, F. G., You, X. Y., Zhang, R., Zhang, B. L., & He, G. L. (2015). Optimization of a premixed cylindrical burner for low pollutant emission. *Energy Conversion and Management*, *99*, 151–160. https://doi.org/10.1016/j.enconman.2015.04.039